Wave-current interactions in coastal areas

Von der Fakultät für Mathematik und Naturwissenschaften der Carl von Ossietzky Universität Oldenburg zur Erlangung des Grades und Titels eines Doktors der Naturwissenschaften (Dr. rer. nat.) angenommene Dissertation

von

Sebastian Grashorn

geboren am 10.04.1981 in Bremen

12.06.2013

Erstgutachter: Prof. Dr. Jörg-Olaf Wolff
Zweitgutachter: Prof. Dr. Emil V. Stanev

Tag der Disputation: 05.07.2013

This thesis is dedicated in loving memory of my godmother Rotraud and my father Knud.

**There is a tide in the affairs of men,
Which, taken on the flood, leads on to fortune;
Omitted, all the voyage of their life
Is bound in shallows and in miseries.
On such a full sea we now afloat,
And we must take the current when it serves,
Or lose our ventures.**

(William Shakespeare)

Abstract

Many coastal areas are threatened by flooding due to an increasing sea level. A deep understanding of the physical processes in the ocean and especially in these coastal areas is required to evaluate strategies to confront these problems. Wave-current interactions describe processes and the exchange of energy between waves and currents. In coastal areas these interactions as e.g. the radiation stress can generate strong longshore currents. In this thesis, the unstructured-grid ocean model FVCOM coupled to the wave model FVCOM-SWAVE with different model setups and different grid resolutions is used to investigate the wave-current interactions in two coastal areas.

The first area includes the East-Frisian Wadden Sea islands as part of the southern North Sea. A North Sea model with a coarse resolution and a Wadden Sea model with a fine resolution up to 50 m have been developed. Both models are validated using observational data. The models produce reasonable results, but a shift in phase of the sea level signal compared to observations is quite noticeable. In view of the theoretical results discussed here this forcing error has no direct consequences. The model with the high resolution shows a better performance in predicting the current velocities during a storm event in 2006. During this event, the wave energy flux reaches values up to 190 kW/m in front of the East Frisian Wadden Sea islands. Some energy enters the inlet between the barrier islands, providing erosion potential in this area. A sensitivity study shows that the highest longshore current speeds are generated with winds coming from a NW-direction. These currents reach values up to 1 m/s during the storm event and have an eastward direction. Without the wave model coupled to the hydrodynamic model the calculated longshore currents are too small. Therefore, a coupled modelling system could be essential to calculate e.g. the sediment or bedload transport along the coastline.

The second investigated area is a reef region on the volcanic island Moorea. Here, the wave-induced set-up and set-down at the reef crest are calculated by the model and compared to theoretical values and observational data. The calculated wave-induced set-down is too small compared to the theoretical value, but the wave-induced set-up compares well with the observational data. The current pattern of the reef region is reproduced by the model, but the predicted current velocities are overestimated. Nevertheless, the preliminary results are promising and an increased drag coefficient could improve the results.

The overall performance of the FVCOM modelling system is satisfying. Some aspects of the wave-current interactions in these specific areas have been investigated and interesting consequences of these interactions can be observed in the model output. The model benefits from the unstructured-grid approach especially in coastal areas.

Zusammenfassung

Viele Küstengebiete sind aufgrund des ansteigenden Meeresspiegels einer Überflutungsgefahr ausgesetzt. Um Strategien zu entwickeln, die sich mit diesen Problemen auseinandersetzen, ist ein tiefes Verständnis der physikalische Prozesse im Ozean und besonders in Küstengebieten erforderlich. Welle-Strömungsinteraktionen beschreiben Prozesse und den Austausch von Energie zwischen Wellen und Strömungen. In Küstenregionen können diese Interaktionen wie z.B. der sogenannte „Radiation Stress“ starke zur Küste parallel verlaufende Strömungen erzeugen.

In dieser Dissertation wird das auf unstrukturierten Gittern basierende Ozeanmodel FVCOM, das mit dem Wellenmodell FVCOM-SWAVE gekoppelt ist, mit unterschiedlichen Modellkonfigurationen und unterschiedlichen Auflösungen dazu benutzt, die Welle-Strömungsinteraktionen in zwei Küstenregionen zu untersuchen.

Die erste Region enthält das ostfriesische Wattenmeer als Teil der südlichen Nordsee. Ein Nordseemodell mit einer groben Auflösung und ein Wattenmeermodell mit einer Auflösung von bis zu 50 m sind erstellt worden. Beide Modelle werden mit Beobachtungsdaten validiert. Die Modelle produzieren sinnvolle Resultate, aber ein Phasenverschub des Meereshöhensignals verglichen mit den Beobachtungen ist durchaus feststellbar. Unter der Sicht der hier diskutierten theoretischen Resultate hat dieser Antriebsfehler keine direkten Konsequenzen. Das Modell mit der höheren Auflösung erzielt ein besseres Ergebnis bei der Vorhersage der Strömungsgeschwindigkeiten während eines Sturmereignisses im Jahr 2006. Während dieses Ereignisses erreicht der Wellenenergiefluss Werte von bis zu 190 kW/m im Bereich vor den ostfriesischen Wattenmeerinseln. Ein Teil dieser Energie tritt auch in den Zugang zwischen den Barriereinseln ein und stellt damit ein Erosionspotential in diesem Gebiet bereit. Eine Sensitivitätsstudie zeigt, dass die höchsten küstenparallelen Strömungsgeschwindigkeiten durch aus dem Nordwesten kommende Winde erzeugt werden. Diese Strömungen erreichen Werte bis zu 1 m/s während des Sturmereignisses und sind ostwärts gerichtet. Ohne das an das hydrodynamische Modell gekoppelte Wellenmodell werden die küstenparallelen Strömungen zu gering berechnet. Deshalb könnte ein gekoppeltes Modellsystem unentbehrlich für die Berechnung von z.B. Sediment- oder Geschiebetransport entlang der Küstenlinie sein.

Das zweite untersuchte Gebiet ist eine Riffregion auf der Vulkaninsel Moorea. Hier werden das welleninduzierte „Set-up“ und „Set-down“ am Riffkamm vom Modell berech-

net und mit theoretischen Werten und Beobachtungsdaten verglichen. Das berechnete welleninduzierte „Set-down“ ist zu gering verglichen mit dem theoretischen Wert, aber das welleninduzierte „Set-up“ lässt sich gut mit den Beobachtungsdaten vergleichen. Das Strömungsmuster der Riffregion wird von dem Modell wiedergegeben, aber die vorhergesagten Strömungsgeschwindigkeiten werden überschätzt. Trotzdem sind die bisherigen Ergebnisse vielversprechend und ein erhöhter Strömungswiderstandskoeffizient könnte die Ergebnisse verbessern.

Die insgesamte Leistungsfähigkeit des FVCOM-Modellsystems ist zufriedenstellend. Einige Aspekte der Welle-Strömungsinteraktionen in diesen speziellen Gebieten sind untersucht worden und es können interessante Konsequenzen dieser Interaktionen in dem Modelloutput beobachtet werden. Besonders in Küstenregionen profitiert das Modell von dem auf unstrukturierten Gittern basierenden Ansatz.

Contents

List of Figures

1 Introduction

One of the most important parts of the Earth's climate system is the ocean because 70.8% of the Earth's surface is covered with water (see Snelgrove 1999) and 97% of the water lies in the ocean (see Garrison 2007). Traditionally, coastal areas are a popular place for human settlement to engage in activities as e.g. fishery, traffic, trade and tourism. A lot of metropolises are located at the coast and McGranahan et al. (2007) report that 10% of the world's population and 13% of the world's urban population are living in an area that is less than 10 metres above sea level. In the ICCP (2007) report scenarios with a predicted global mean sea level change up to 50 cm within the next 100 years are predicted, implying that many coastal areas are threatened by flooding in these scenarios. In order to evaluate strategies to confront these problems a deep understanding of the physical processes in the ocean is required.

Ocean modelling is a powerful tool to investigate a variety of physical aspects ranging from the deep ocean dynamics to the behaviour of specific coastal areas. These models have first been used in the 1960's (see Bryan and Cox 1967, Bryan 1969). In contrast to in-situ measurements, ocean models may cover vast areas of the ocean calculating estimates for current velocities and tracers like temperature or salinity. This is especially useful at times and in areas where it is impossible to directly observe the oceanic variables (e.g. in hurricane conditions or under the ice shelves).

The topic of this thesis is related to wave-current interactions in coastal areas. The wave-current interactions describe processes where waves influence the coastal currents or currents change the behaviour of the waves. One aspect of this interaction is the longshore current generated by waves. This process may have a big influence on the dynamics of the ocean close to the coast since it is able to initiate and enhance the transport of sediments and thus to influence the long-term morphological evolution of the coastal area. The wave-current interactions may also be directly responsible for the whole current circulation in a specific area, thus being the main influence on the biological system in that coastal area.

The investigated areas of the East-Frisian Wadden Sea located in the southern North Sea and the island Moorea located in the southern Pacific were chosen because in these areas the above mentioned physical processes are expected to occur and can be investigated utilising an ocean model. Additionally, for these areas observational data was available, so the results of the models can be compared to realistic data and the reliability of the results can be tested.

The ocean model used during the preparation of this thesis is named FVCOM (Finite-Volume Coastal Ocean Circulation model) (see Chen et al. 2003) and has recently been coupled to the surface wave model FVCOM-SWAVE (see Qi et al. 2009), making it possible to investigate wave-current interactions. Another advantage of this model is the unstructured nature of the grid that is used for the computations performed by FVCOM. In this way a high resolution in areas of interest can be chosen to guarantee a sufficient resolution of the ongoing processes. There are also other ocean models providing methods to reveal wave-current-driven processes (see e.g. ROMS, GETM, SELFE) with structured or unstructured grids, but FVCOM was one of the first unstructured-grid models offering the possibility to investigate wave-current interactions.

Wave-current interactions have been extensively described in the modern literature including examples for the North Sea region. Pleskachevsky et al. (2009) investigated the impact of a storm surge on the North-Frisian island of Sylt by estimating the wave energy flux and the effects of wave-current interactions. Osuna and Monbaliu (2004) investigated various aspects of wave-current interactions with a focus on the Belgian coast. Hench et al. (2008) and Ahmerkamp (2010) investigated wave-induced effects on the Moorea island and these results can be compared to the data estimated by the Moorea model setup.

The aims of the thesis are to develop and test model setups for the above mentioned areas of the North Sea, East-Frisian Wadden Sea and Moorea island, to compare and validate the model results using observations and to discuss the influence of the wave-current interactions on this specific areas. Especially, in the East-Frisian Wadden Sea the longshore currents produced by wave-current interactions have not been addressed by ocean modelling efforts so far.

This thesis consists of several parts. In chapter 2 the fundamental theoretical equations for hydrodynamic and surface wave modelling are explained. The application of the ocean model FVCOM is illustrated in chapter 3. In chapter 4 and in chapter 5 the influence of the wave-current interactions in the regions of the southern North Sea area including the East Frisian Wadden Sea and of the Moorea island are investigated and discussed, respectively, and in chapter 6 some conclusions are drawn.

The preparation of this thesis was supported and funded by the Ministry for Science and Culture of Lower Saxony within the network KLIFF - climate impact and adaption research in Lower Saxony and the initiative Earth Science Knowledge Platform (ESKP) operated by the Helmholtz Association.

2 Theoretical background of ocean models

In order to develop and evaluate an ocean model as a tool to investigate various dynamics in the ocean a theoretical background has to be set up, consisting of so-called governing equations to calculate various quantities as e.g. velocity, density, salinity, temperature etc. Several theoretical approaches (see e.g. Mellor 2003, 2005, 2008, Chen et al. 2006a, Warner et al. 2008, Wu 2009, Wu et al. 2011) have been published and the theoretical aspects that are summarised in section 2.1 provide a theoretical background with a focus on the ocean model FVCOM that was used as a tool for the investigations made during the preparation of this thesis. In section 2.2 some theoretical aspects about wave modelling are explained. The wave model FVCOM-SWAVE is very similar to the wave model SWAN (see Booij et al. 1999). The theoretical background of SWAN is explained in Holthuijsen (2007).

2.1 Hydrodynamics

2.1.1 Governing equations of ocean models in Cartesian coordinates

To derive a set of governing equations to represent processes that can be observed in the dynamics of the ocean several well known physical equations or laws can be utilised. At first, the conversation of mass can be used to derive the equation of continuity, assuming seawater as incompressible:

$$\frac{\partial u}{\partial x} + \frac{\partial v}{\partial y} + \frac{\partial w}{\partial z} = 0 \tag{2.1}$$

To derive this equation a small fixed cuboid called control volume can be considered (see figure 2.1). The dimensions of this cuboid are δx, δy and δz and no amount of fluid is produced or destroyed inside the cuboid (see e.g. Simpson and Sharples 2012). In the x-direction the net rate of mass flow across the boundaries of the cuboid is (see e.g. Versteeg and Malalasekera 2007):

$$\left(\rho u - \frac{\partial\left(\rho u\right)}{\partial x}\frac{1}{2}\delta x\right)\delta y\delta z - \left(\rho u + \frac{\partial\left(\rho u\right)}{\partial x}\frac{1}{2}\delta x\right)\delta y\delta z = -\frac{\partial\left(\rho u\right)}{\partial x}\delta x\delta y\delta z \tag{2.2}$$

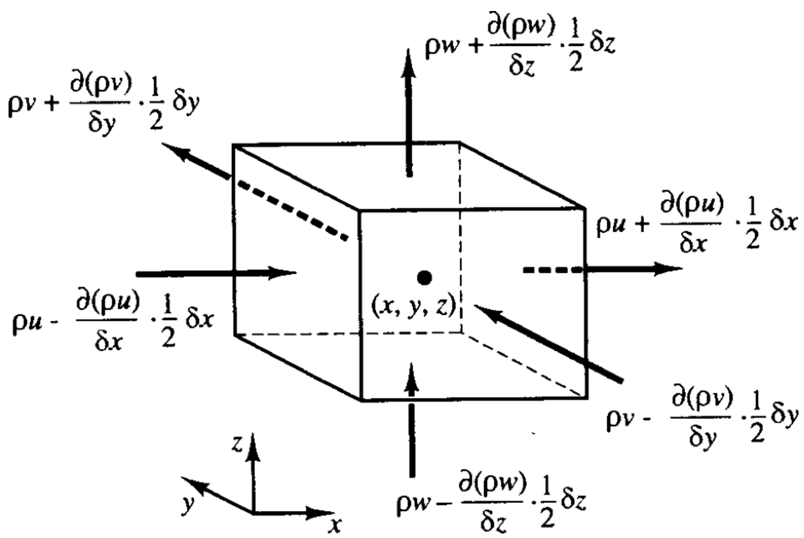

Figure 2.1: Cuboid as a control volume to derive the equation of continuity (Source: Versteeg and Malalasekera (2007))

Summing up all contributions in all directions and through all boundaries of the cuboid and equating these terms with the rate of change of mass inside the cuboid yields:

$$\frac{\partial \rho}{\partial t} + \nabla \cdot (\rho \vec{u}) = 0 \tag{2.3}$$

Assuming seawater as incompressible, as mentioned above, leads to equation 2.1. The vector $\vec{u}$ consists of the components u, v and w in the x-, y- and z-direction, respectively. The density of the fluid is denoted as ρ and the time as t.
Following Simpson and Sharples (2012) to express the equations of motion of a unit volume Newton's second law is used and the influence of the Coriolis force f is added:

$$\frac{du}{dt} = fv + \frac{F_x}{\rho} \tag{2.4}$$
$$\frac{dv}{dt} = -fu + \frac{F_y}{\rho} \tag{2.5}$$

The terms F_x and F_y represent net forces per unit volume acting in the x- and y-direction, respectively. The effect of the vertical component of the Coriolis force is very small and can be neglected here. An expression for motion in the z-direction will be given later.
To add the pressure p and frictional forces again a cuboid shown in figure 2.2 can be considered. The difference of the pressure forces acting on two sides of the cuboid in the x-direction (see figure 2.2 (a)) is given as follows:

$$\left(p - \frac{\partial p}{\partial x}\frac{1}{2}\delta x\right)\delta y \delta z - \left(p + \frac{\partial p}{\partial x}\frac{1}{2}\delta x\right)\delta y \delta z = -\frac{\partial p}{\partial x}\delta x \delta y \delta z \tag{2.6}$$

The same applies for the y- and z-direction.

To derive the frictional forces the stress $\tau(z)$ shall be the stress component exerted by the fluid on the lower side of a plane on the fluid above it. The bottom of the cuboid will

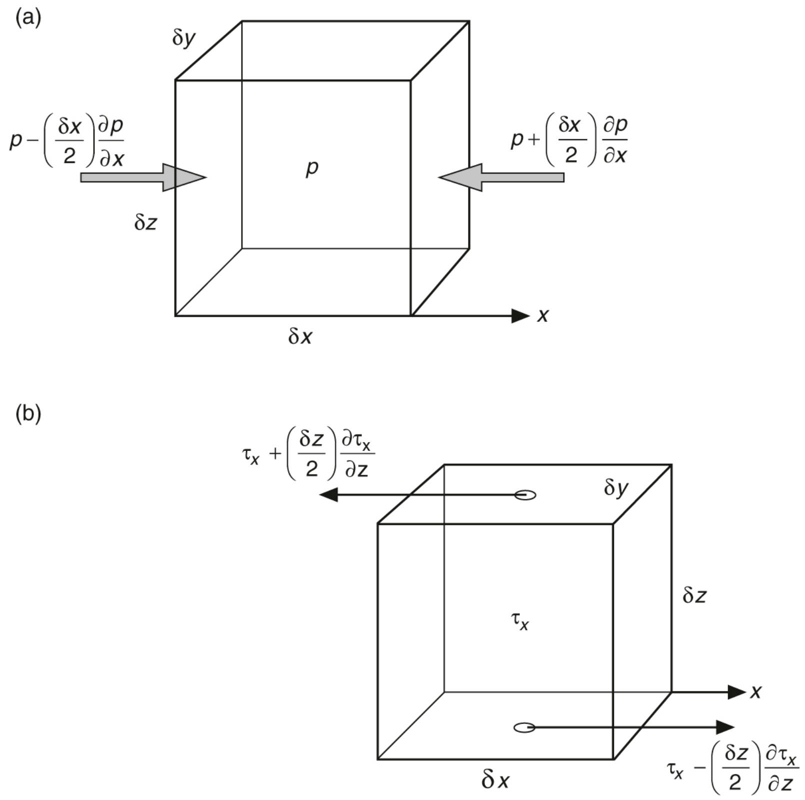

Figure 2.2: Cuboid as a control volume to derive the pressure and frictional forces (Source: Simpson and Sharples (2012))

then experience a force in the positive x-direction and according to Newton's third law an equal force in the opposite direction (see figure 2.2 (b)) and the net force acting in the x-direction is:

$$\left[\left(\tau_x-\frac{\partial\tau_x}{\partial z}\frac{1}{2}\delta z\right)-\left(\tau_x+\frac{\partial\tau_x}{\partial z}\frac{1}{2}\delta z\right)\right]\delta x\delta y=-\frac{\partial\tau_x}{\partial z}\delta z\delta x\delta y \tag{2.7}$$

Again, the same procedure can be applied for the y- and z-direction.

Adding pressure and frictional forces to the equations of horizontal motion 2.4 and 2.5 results in the so-called governing equations for ocean models (see Simpson and Sharples 2012):

$$\frac{du}{dt} = fv-\frac{1}{\rho}\left(\frac{\partial p}{\partial x}+\frac{\partial\tau_x}{\partial z}\right)+\frac{F_u}{\rho} \tag{2.8}$$

$$\frac{dv}{dt} = -fu-\frac{1}{\rho}\left(\frac{\partial p}{\partial y}+\frac{\partial\tau_y}{\partial z}\right)+\frac{F_v}{\rho} \tag{2.9}$$

Here, F_u and F_v are additional forces acting in the x- and y-direction, respectively. The quantities τ_x and τ_y are the frictional stresses associated with vertical changes in the horizontal flow (vertical shear stresses). Horizontal shear stresses can be added as additional terms. An equation of motion in the z-direction can also be stated:

$$\frac{dw}{dt} = -\frac{1}{\rho}\frac{\partial p}{\partial z} - g \tag{2.10}$$

This simplified form results from the neglection of the vertical Coriolis component and the small frictional forces compared to the gravitational acceleration g. Furthermore, vertical accelerations are small compared to g, so the only force remaining is the pressure gradient (hydrostatic approximation):

$$\frac{\partial p}{\partial z} = -\rho g \tag{2.11}$$

Additionally, the changes of the density in the horizontal direction are very small, so the density in the equations of momentum for the x- and y- direction can be set to a static density stated as ρ_0 (Boussinesq approximation) (see e.g. Phillips 1977).
It can also be assumed that the frictional stresses are proportional to the velocity shear components:

$$\tau_x = -\rho_0 K_m \frac{\partial u}{\partial z} \tag{2.12}$$
$$\tau_y = -\rho_0 K_m \frac{\partial v}{\partial z} \tag{2.13}$$

Here, K_m is the vertical eddy viscosity that can be calculated using different parametrisation approaches (see section 2.1.4).
The density of seawater is connected to the water temperature T_w and the salinity S by the equation of state (see Blumberg and Mellor 1987):

$$\rho = \rho\,(T_w, S) \tag{2.14}$$

The equation must be evaluated at atmospheric pressure.
The final equations for a complete set of governing equations are the expressions for the water temperature and the salinity (see e.g. Chen et al. 2006a):

$$\frac{\partial T_w}{\partial t} + u\frac{\partial T_w}{\partial x} + v\frac{\partial T_w}{\partial y} + w\frac{\partial T_w}{\partial z} = \frac{\partial}{\partial z}\left(K_h\frac{\partial T_w}{\partial z}\right) + F_{T_w} \tag{2.15}$$
$$\frac{\partial S}{\partial t} + u\frac{\partial S}{\partial x} + v\frac{\partial S}{\partial y} + w\frac{\partial S}{\partial z} = \frac{\partial}{\partial z}\left(K_h\frac{\partial S}{\partial z}\right) + F_S \tag{2.16}$$

Here, , K_h is the thermal vertical eddy diffusion coefficient, F_{T_w} and F_S are the terms describing the horizontal diffusion.

Following Chen et al. (2006a) at the surface and at the bottom of the water column boundary conditions have to be set to solve the governing equations and these are for the temperature:

$$\frac{\partial T_w}{\partial z} = \frac{1}{\rho c_{p,w} K_h} \left(Q_n \left(x, y, t\right) - SW \left(x, y, \eta, t\right)\right) \quad \text{at } z = \eta \left(x, y, t\right) \tag{2.17}$$

$$\frac{\partial T_w}{\partial z} = \frac{A_h \tan\left(\alpha_b\right)}{K_h} \frac{\partial T_w}{\partial n} \quad \text{at } z = -h \left(x, y\right) \tag{2.18}$$

Here, h is the depth relative to $z = 0$, $D = h + \eta$ is the total water depth, η is the free surface relative to $z = 0$, Q_n is the surface net heat flux, $SW\left(x, y, 0, t\right)$ is the shortwave flux incident at the sea surface, $c_{p,w}$ is the specific heat of seawater, A_h is the horizontal thermal diffusion coefficient, α_b is the slope of the bottom bathymetry and n is a horizontal

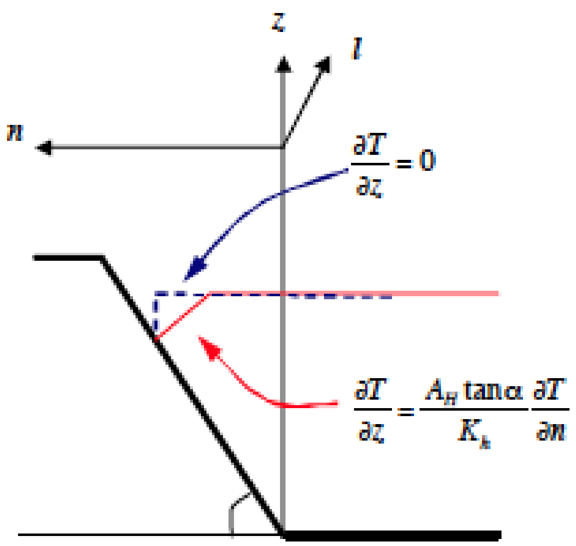

Figure 2.3: Bottom boundary condition for temperature over a sloping bottom (Source: Chen et al. (2006a))

coordinate (see figure 2.3).

For the salinity the surface and bottom boundary conditions are defined as follows:

$$\frac{\partial S}{\partial z} = 0 \quad \text{at } z = \eta \left(x, y, t\right) \tag{2.19}$$

$$\frac{\partial S}{\partial z} = \frac{A_h \tan\left(\alpha_b\right)}{K_h} \frac{\partial S}{\partial n} \quad \text{at } z = -h \left(x, y\right) \tag{2.20}$$

The surface and bottom boundary conditions for the velocities u, v and w are:

$$K_m\left(\frac{\partial u}{\partial z},\frac{\partial v}{\partial z}\right)=\frac{1}{\rho_0}\left(\tau_{sx},\tau_{sy}\right),\ w=\frac{\partial \eta}{\partial t}+u\frac{\partial \eta}{\partial x}+v\frac{\partial \eta}{\partial y}+\frac{\hat{E}-\hat{P}}{\rho}$$
$$\text{at } z=\eta\left(x,y,t\right) \tag{2.21}$$
$$K_m\left(\frac{\partial u}{\partial z},\frac{\partial v}{\partial z}\right)=\frac{1}{\rho_0}\left(\tau_{bx},\tau_{by}\right),\ w=-u\frac{\partial h}{\partial x}-v\frac{\partial h}{\partial y}+\frac{Q_b}{\Omega}$$
$$\text{at } z=-h\left(x,y\right) \tag{2.22}$$

Here, (τ_{sx},τ_{sy}) and $(\tau_{bx},\tau_{by})=C_{d,b}\sqrt{u^2+v^2}\,(u,v)$ are the x- and y-components of the surface wind and bottom stresses, respectively, Q_b is the groundwater volume flux at the bottom, $\hat{P}$ and $\hat{E}$ are the precipitation and evaporation, respectively and Ω is the area of the groundwater source. The drag coefficient $C_{d,b}$ is calculated using a logarithmic bottom layer at a height z_{ab} above the bottom:

$$C_{d,b}=max\left(\frac{\kappa^2}{ln\left(\frac{z_{ab}}{z_0}\right)^2},0.0025\right) \tag{2.23}$$

The von-Karman-constant is $\kappa=0.4$ and the maximum value of the drag coefficient is often chosen as 0.0025 and the value of the bottom roughness length z_0 as 0.001.
The components of the wind stress can be split into a skin friction part and a form drag part τ_{sx} and τ_{sy}. The skin friction part is described in the equations 2.12 and 2.13 and the form drag part can be calculated as (see e.g. Wu 1982)

$$\tau_s=\rho_{air}C_{d,s}U_{10}^2 \tag{2.24}$$

using a drag coefficient given by Large and Pond (1981) as

$$C_{d,s}=10^{-3}\begin{cases}1.2, & U_{10} & <11\frac{m}{s},\\ 0.49+0.0065U_{10}, & 11\frac{m}{s} & \leq U_{10}<25\frac{m}{s},\\ 0.49+0.0065\cdot 25 & 25\frac{m}{s} & \leq U_{10},\end{cases} \tag{2.25}$$

where U_{10} is the wind speed at a height of 10 m and ρ_{air} is the density of the air.
Finally, the conditions for the kinematic, heat and salt flux conditions on the solid boundary are given as:

$$v_{n_b}=0,\ \frac{\partial T_w}{\partial n_b}=0,\ \frac{\partial S}{\partial n_b}=0 \tag{2.26}$$

The velocity v_{n_b} is the velocity component normal to the boundary and n_b is the direction normal to the boundary.

2.1.2 Governing equations of ocean models in σ-coordinates

In a number of models the vertical coordinate z is often replaced by a so-called σ-coordinate. By applying this transformation a better representation of the irregular bottom topography can be obtained. Following Chen et al. (2006a) and Wu (2009) the σ-transformation defined as:

$$\sigma = \frac{z-\eta}{h+\eta} = \frac{z-\eta}{D} \tag{2.27}$$

Values of σ vary between -1 at the bottom and 0 at the surface.
Using the σ-coordinate the equations 2.1, 2.8, 2.9, 2.14, 2.15 and 2.16 can be transformed into:

$$\frac{\partial \eta}{\partial t} + \frac{\partial Du}{\partial x} + \frac{\partial Dv}{\partial y} + \frac{\partial \omega}{\partial \sigma} = 0 \tag{2.28}$$

$$\begin{aligned}&\frac{\partial uD}{\partial t} + \frac{\partial u^2 D}{\partial x} + \frac{\partial uvD}{\partial y} + \frac{\partial u\omega}{\partial \sigma} - fvD = \\ &- gD\frac{\partial \eta}{\partial x} - \frac{gD}{\rho_0}\left[\frac{\partial}{\partial x}\left(D\int_\sigma^0 \rho D\sigma'\right) + \sigma\rho\frac{\partial D}{\partial x}\right] + \frac{1}{D}\frac{\partial}{\partial \sigma}\left(K_m\frac{\partial u}{\partial \sigma}\right) + DF_x\end{aligned} \tag{2.29}$$

$$\begin{aligned}&\frac{\partial vD}{\partial t} + \frac{\partial uvD}{\partial x} + \frac{\partial v^2 D}{\partial y} + \frac{\partial v\omega}{\partial \sigma} + fuD = \\ &- gD\frac{\partial \eta}{\partial y} - \frac{gD}{\rho_0}\left[\frac{\partial}{\partial y}\left(D\int_\sigma^0 \rho D\sigma'\right) + \sigma\rho\frac{\partial D}{\partial y}\right] + \frac{1}{D}\frac{\partial}{\partial \sigma}\left(K_m\frac{\partial v}{\partial \sigma}\right) + DF_y\end{aligned} \tag{2.30}$$

$$\frac{\partial T_w D}{\partial t} + \frac{\partial T_w uD}{\partial x} + \frac{\partial T_w vD}{\partial y} + \frac{\partial T_w \omega}{\partial \sigma} = \frac{1}{D}\frac{\partial}{\partial \sigma}\left(K_h\frac{\partial T_w}{\partial \sigma}\right) + D\hat{H} + DF_{T_w} \tag{2.31}$$

$$\frac{\partial SD}{\partial t} + \frac{\partial SuD}{\partial x} + \frac{\partial SvD}{\partial y} + \frac{\partial S\omega}{\partial \sigma} = \frac{1}{D}\frac{\partial}{\partial \sigma}\left(K_h\frac{\partial S}{\partial \sigma}\right) + DF_S \tag{2.32}$$

$$\rho = \rho\left(T_w, S\right) \tag{2.33}$$

Here, ω is the velocity normal to the σ-layers and $\hat{H}$ is the solar irradiance.
The horizontal diffusion terms can be defined as follows:

$$DF_x \approx \frac{\partial}{\partial x}\left[2A_m h\frac{\partial u}{\partial x}\right] + \frac{\partial}{\partial y}\left[A_m h\left(\frac{\partial u}{\partial y} + \frac{\partial v}{\partial x}\right)\right] \tag{2.34}$$

$$DF_y \approx \frac{\partial}{\partial x}\left[A_m h\left(\frac{\partial u}{\partial y} + \frac{\partial v}{\partial x}\right)\right] + \frac{\partial}{\partial y}\left[2A_m h\frac{\partial v}{\partial y}\right] \tag{2.35}$$

$$D\left(F_{T_w}, F_S\right) \approx \left[\frac{\partial}{\partial x}\left(A_h h\frac{\partial}{\partial x}\right) + \frac{\partial}{\partial y}\left(A_h h\frac{\partial}{\partial y}\right)\right]\left(T_w, S\right) \tag{2.36}$$

The horizontal eddy and thermal diffusion coefficients are denoted as A_m and A_h, respectively.
At the surface ($\sigma = 0$) the boundary conditions for the velocities, the temperature and

the salinity are defined as follows

$$\left(\frac{\partial u}{\partial \sigma}, \frac{\partial v}{\partial \sigma}\right) = \frac{D}{\rho_0 K_m}\left(\tau_{sx}, \tau_{sy}\right), \ \omega = 0, \tag{2.37}$$

$$\frac{\partial T_w}{\partial \sigma} = \frac{D}{\rho c_{p,w} K_h}\left[Q_n\left(x, y, t\right) - SW\left(x, y, 0, t\right)\right], \tag{2.38}$$

$$\frac{\partial S}{\partial \sigma} = 0 \tag{2.39}$$

and at the bottom ($\sigma = -1$) these conditions are

$$\left(\frac{\partial u}{\partial \sigma}, \frac{\partial v}{\partial \sigma}\right) = \frac{D}{\rho_0 K_m}\left(\tau_{bx}, \tau_{by}\right), \ \omega = 0, \tag{2.40}$$

$$\frac{\partial T_w}{\partial \sigma} = \frac{A_h D \, tan\left(\alpha\right)}{K_h - A_h tan^2\left(\alpha\right)} \frac{\partial T_w}{\partial n}, \tag{2.41}$$

$$\frac{\partial S}{\partial \sigma} = \frac{A_h D \, tan\left(\alpha\right)}{K_h - A_h tan^2\left(\alpha\right)} \frac{\partial S}{\partial n}. \tag{2.42}$$

The governing equations can also be transformed into spherical coordinates. This procedure is explained in detail in Chen et al. (2006a).

2.1.3 The 2D (vertically-integrated) equation

In the governing equations fast moving surface gravity waves are described by the surface elevation (see Chen et al. 2006a). Using an explicit numerical approach the phase speed of

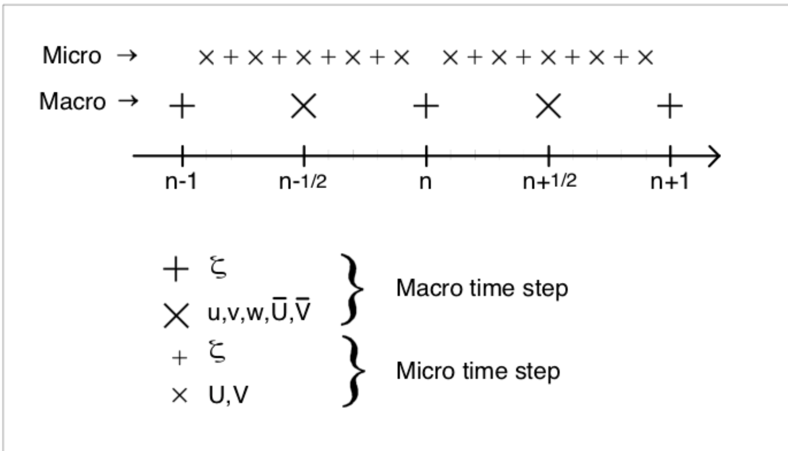

Figure 2.4: Mode-splitting (Source: Burchard and Bolding (2002))

these waves $\left(\sqrt{gd}\right)$ determines the time step of the model. The surface elevation depends on the gradient of the water transport and therefore it can be calculated using vertically integrated equations. With a given surface elevation the 3D-equations can then be solved. This procedure is called mode-splitting and the currents are split up into external and

internal modes with two different time steps. The variables that are calculated at the different time steps can be seen in figure 2.4. The 2D-equations are solved for every micro (external) time step and then the time-averaged velocities and the surface elevation are used in the macro (internal) time step to solve the 3D-equations.
The 2D vertically integrated equations are defined as (see Chen et al. 2006a):

$$\frac{\partial \eta}{\partial t} + \frac{\partial (\overline{u} D)}{\partial x} + \frac{\partial (\overline{v} D)}{\partial y} + \frac{\hat{E} - \hat{P}}{\rho} + \frac{Q_b}{\Omega} = 0 \tag{2.43}$$

$$\frac{\partial \overline{u} D}{\partial t} + \frac{\partial \overline{u}^2 D}{\partial x} + \frac{\partial \overline{uv} D}{\partial y} - f \overline{v} D$$
$$= -gD\frac{\partial \eta}{\partial x} - \frac{gD}{\rho_0}\left(\int_{-1}^{0} \frac{\partial}{\partial x}\left(D \int_{\sigma}^{0} \rho d\sigma'\right) d\sigma + \frac{\partial D}{\partial x}\int_{-1}^{0} \sigma \rho d\sigma\right) + \frac{\tau_{sx} - \tau_{bx}}{\rho_0} + D\tilde{F}_x + G_x \tag{2.44}$$

$$\frac{\partial \overline{v} D}{\partial t} + \frac{\partial \overline{uv} D}{\partial x} + \frac{\partial \overline{v}^2 D}{\partial y} + f \overline{u} D$$
$$= -gD\frac{\partial \eta}{\partial y} - \frac{gD}{\rho_0}\left(\int_{-1}^{0} \frac{\partial}{\partial y}\left(D \int_{\sigma}^{0} \rho d\sigma'\right) d\sigma + \frac{\partial D}{\partial y}\int_{-1}^{0} \sigma \rho d\sigma\right) + \frac{\tau_{sy} - \tau_{by}}{\rho_0} + D\tilde{F}_y + G_y \tag{2.45}$$

Here, the coefficients G_x and G_y are

$$G_x = \frac{\partial \overline{u}^2 D}{\partial x} + \frac{\partial \overline{u}\,\overline{v} D}{\partial y} - D\tilde{F}_x - \left(\frac{\partial \overline{u^2} D}{\partial x} + \frac{\partial \overline{uv} D}{\partial y} - D\overline{F}_x\right) \tag{2.46}$$

$$G_y = \frac{\partial \overline{u}\,\overline{v} D}{\partial x} + \frac{\partial \overline{v}^2 D}{\partial y} - D\tilde{F}_y - \left(\frac{\partial \overline{uv} D}{\partial x} + \frac{\partial \overline{v^2} D}{\partial y} - D\overline{F}_y\right) \tag{2.47}$$

with the horizontal diffusion terms approximately given as

$$D\tilde{F}_x \approx \frac{\partial}{\partial x}\left[2\overline{A}_m H \frac{\partial \overline{u}}{\partial x}\right] + \frac{\partial}{\partial y}\left[\overline{A}_m H \left(\frac{\partial \overline{u}}{\partial y} + \frac{\partial \overline{v}}{\partial x}\right)\right] \tag{2.48}$$

$$D\tilde{F}_y \approx \frac{\partial}{\partial x}\left[\overline{A}_m H \left(\frac{\partial \overline{u}}{\partial y} + \frac{\partial \overline{v}}{\partial x}\right)\right] + \frac{\partial}{\partial y}\left[2\overline{A}_m H \frac{\partial \overline{v}}{\partial y}\right] \tag{2.49}$$

$$D\overline{F}_x \approx \frac{\partial}{\partial x}\overline{2 A_m H \frac{\partial u}{\partial x}} + \frac{\partial}{\partial y}\overline{A_m H \left(\frac{\partial u}{\partial y} + \frac{\partial v}{\partial x}\right)} \tag{2.50}$$

$$D\overline{F}_y \approx \frac{\partial}{\partial x}\overline{A_m H \left(\frac{\partial u}{\partial y} + \frac{\partial v}{\partial x}\right)} + \frac{\partial}{\partial y}\overline{2 A_m H \frac{\partial v}{\partial y}} \tag{2.51}$$

The overbar denotes the vertical integration.

2.1.4 The turbulence closure models

The governing equations have to be mathematically closed using a turbulence closure model to determine the coefficients for horizontal or vertical diffusion (or mixing). For the horizontal diffusion the Smagorinsky eddy parametrisation method is widely used (see Smagorinsky 1963). For the momentum equations the coefficient is (see Chen et al. 2006a)

$$A_m = \frac{1}{2} C \Omega^u \sqrt{\left(\frac{\partial u}{\partial x}\right)^2 + \frac{1}{2}\left(\frac{\partial v}{\partial x} + \frac{\partial u}{\partial y}\right)^2 + \left(\frac{\partial v}{\partial y}\right)^2} \tag{2.52}$$

and for tracers (e.g. temperature)

$$A_h = \frac{1}{2} \frac{C \Omega^\eta}{P_r} \sqrt{\left(\frac{\partial u}{\partial x}\right)^2 + \frac{1}{2}\left(\frac{\partial v}{\partial x} + \frac{\partial u}{\partial y}\right)^2 + \left(\frac{\partial v}{\partial y}\right)^2}. \tag{2.53}$$

Here, C is a constant, Ω^u is the area of the individual momentum control element, Ω^η is the area of the individual tracer control element and P_r is the Prandtl number. The Prandtl number can be defined as the ratio between the momentum and thermal diffusion rate:

$$P_r = \frac{A_m}{A_h} \tag{2.54}$$

The coefficient A_m depends on the resolution of the model and the gradient of the horizontal velocities while the coefficient A_h depends on the area of the individual tracer control element and the horizontal gradient of the tracer concentration. These control elements are explained in section 3.2.

To calculate the vertical eddy viscosity coefficient K_m and the thermal eddy diffusion coefficient K_h several approaches are given in the literature. During the preparation of this thesis the Mellor and Yamada level 2.5 (MY-2.5) turbulence closure model was used, but another popular turbulence closure model suite is GOTM that offers several models, e.g. the $k - \epsilon$ type model (see Burchard 2002). The MY-2.5 model is a $q - ql$ type model and can be enhanced using the upper and lower limits of the stability functions given by Galperin et al. (1988). The turbulent energy input at the surface induced by wind-driven surface wave breaking can be added as it was proposed by Mellor and Blumberg (2004). Kantha and Clayson (1994) presented an improved parametrisation of pressure-strain covariance and shear instability-induced mixing in strongly stratified regions that can also be used to extend the MY-2.5 model. Here, q is used as the turbulent energy and l is the turbulent macroscale. The equations for q^2 and $q^2 l$ can be simplified using a boundary layer approximation where the shear component of turbulent kinetic energy is generated by the vertical shear of the horizontal flow near the boundary and the Coriolis term is neglected (see Mellor and Yamada 1982, Chen et al. 2006a, Wu 2009):

$$\frac{\partial q^2}{\partial t} + u\frac{\partial q^2}{\partial x} + v\frac{\partial q^2}{\partial y} + w\frac{\partial q^2}{\partial z} = 2\left(P_s + P_b - \epsilon\right) + \frac{\partial}{\partial z}\left(K_q \frac{\partial q^2}{\partial z}\right) + F_q \tag{2.55}$$

$$\frac{\partial q^2 l}{\partial t} + u\frac{\partial q^2 l}{\partial x} + v\frac{\partial q^2 l}{\partial y} + w\frac{\partial q^2 l}{\partial z} = lE_1\left(P_s + P_b - \frac{\tilde{W}}{E_1}\epsilon\right) + \frac{\partial}{\partial z}\left(K_q \frac{\partial q^2 l}{\partial z}\right) + F_l \tag{2.56}$$

Here, the turbulent kinetic energy is defined as $q^2 = \left(u'^2 + v'^2\right)/2$, K_q is the vertical eddy diffusion coefficient of the turbulent energy, F_q and F_l are the horizontal diffusion coefficients of the turbulent kinetic energy and macroscale, $P_s = K_m\left[\left(\frac{\partial u}{\partial z}\right)^2 + \left(\frac{\partial v}{\partial z}\right)^2\right]$ and $P_b = \left(gK_h\frac{\partial \rho}{\partial z}\right)/\rho_0$ are the shear and buoyancy production terms of turbulent kinetic energy, respectively, $\epsilon = q^3/B_1 l$ is the turbulent kinetic dissipation rate, $\tilde{W} = 1 + E_2 l^2/\left(\kappa L\right)^2$ is a wall proximity function with $L^{-1} = \left(\eta - z\right)^{-1} + \left(h + z\right)^{-1}$. The coefficients F_q and F_l can be calculated using equation 2.36 and 2.53, but they are kept as small as possible to reduce the effects of horizontal diffusion on the solutions and the turbulence closure model can be run with both variables set to zero (see Chen et al. 2006a).
To close the governing and the turbulent kinetic energy and macroscale equations the following quantities are defined (see Mellor and Yamada 1982, Galperin et al. 1988, Chen et al. 2006a, Wu 2009)

$$K_m = lqS_m,\ K_h = lqS_h,\ K_q = 0.2lq \tag{2.57}$$

using the stability functions

$$S_m = \frac{0.4275 - 3.354Ri}{\left(1 - 34.676Ri\right)\left(1 - 6.127Ri\right)} \text{ and } S_h = \frac{0.494}{1 - 34.676Ri} \tag{2.58}$$

and the Richardson number

$$Ri = -\left(\frac{Nl}{q}\right)^2 \text{ with the BruntVäisälä frequency } N = \left(-\frac{g}{\rho_0}\frac{\partial \rho}{\partial z}\right)^{1/2}. \tag{2.59}$$

The calculation of the stability functions was simplified by Galperin et al. (1988) compared to the original model by Mellor and Yamada (1982), so the stability functions only depend on Ri. The upper bound of Ri for unstable stratification $\left(\frac{\partial \rho}{\partial z} > 0\right)$ is 0.00233 and the lower bound for stable stratification $\left(\frac{\partial \rho}{\partial z} < 0\right)$ is -0.28. The values for B_1, E_1 and E_2 are 16.6, 1.8 and 1.33, respectively (see Mellor and Yamada 1982, Galperin et al. 1988). The boundary conditions are:

$$q^2 l = 0,\ q^2 = B_1^{2/3}u_{\tau s}^2,\ \text{at } z = \eta\left(x, y, t\right) \tag{2.60}$$

$$q^2 l = 0,\ q^2 = B_1^{2/3}u_{\tau b}^2,\ \text{at } z = -h\left(x, y\right) \tag{2.61}$$

Here, the water friction velocities at the surface and at the bottom are denoted as $u_{\tau s}$ and $u_{\tau b}$, respectively. With this approach the coefficients defined in equation 2.57 equal zero at the bottom and at the surface of the water column. Because q^2 is not zero at the boundaries, this results in $l = 0$ (see Chen et al. 2006a). This parametrisation ignores the influence of high wind-generated waves on the turbulent energy flux. Therefore, a new parametrisation was suggested by Mellor and Blumberg (2004):

$$\frac{\partial q^2}{\partial z} = \frac{2\alpha_{CB} u_{\tau s}^3}{K_q}, \; l = max\left(\kappa z_w, l_z\right) \text{ at } z = \eta\left(x, y, t\right) \tag{2.62}$$

The length scale l_z is generally

$$l_z = \kappa z \tag{2.63}$$

for small z and the coefficient α_{CB} is (see Mellor and Blumberg 2004)

$$\alpha_{CB} = 15 \frac{c}{u_*} e^{-(0.04c/u_*)^4}. \tag{2.64}$$

The air side friction velocity is $u_* \approx 30 u_{\tau s}$, c is the phase speed of waves of the dominant frequency and the ratio c/u_* is called the wave age (see Mellor and Blumberg 2004). A parametrisation of the wave-related roughness height is given by Terray et al. (2000) as

$$z_w = 0.85 H_s, \tag{2.65}$$

but there are also other parametrisations in the literature (see Mellor and Blumberg 2004). This approach involving the wave-related roughness height is implemented in the source code of FVCOM version 3.1.4. and led to some difficulties concerning the vertical distribution of the horizontal velocity that is documented in section 3.5.

2.2 Surface waves in the ocean

2.2.1 Characteristic properties of ocean waves

To describe a surface wave using mathematical expressions, it is mandatory to define some wave-related quantities. In figure 2.5 a time series of the elevation of the ocean surface is shown. A surface wave can be defined as the surface elevation between two zero-crossings in the same direction. This may be a downward (see top panel in figure 2.5) or an upward (see bottom panel in figure 2.5) crossing. Most of the time the former definition is used. This originates from the fact that in the early times of oceanography the wave height was determined visually with the naked eye by estimating the wave height as the distance between a prior wave trough and a subsequent wave crest (see Holthuijsen 2007). Furthermore, the steepness of the complete wave front is crucial for the process of

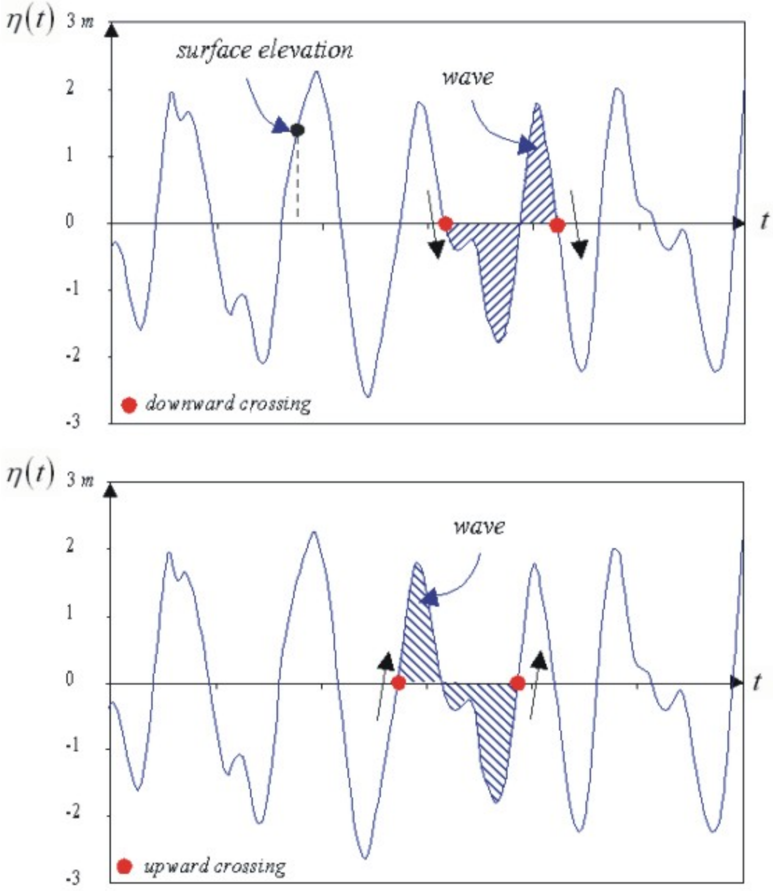

Figure 2.5: Definition of a surface wave within a time series of the surface elevation at a certain position (Source: Holthuijsen (2007))

wave breaking. This steepness can only be captured in the definition shown in the top panel of figure 2.5.

In figure 2.6 some characteristic quantities of a surface wave can be seen. The wave height H is defined as the distance between the maximum and the minimum of the surface elevation. The time lag between two identical phases of the wave is called the period of the wave T or T_0 when defined as the period between to zero-crossing (see Holthuijsen 2007). In the field of oceanography scientists usually use the significant wave height instead of the normal wave height. The significant wave height and the significant wave period are defined as the mean height and period of the highest one-third of waves:

$$H_{1/3} = \frac{1}{N/3} \sum_{j=1}^{N/3} H_j \tag{2.66}$$

$$T_{1/3} = \frac{1}{N/3} \sum_{j=1}^{N/3} T_{0,j} \tag{2.67}$$

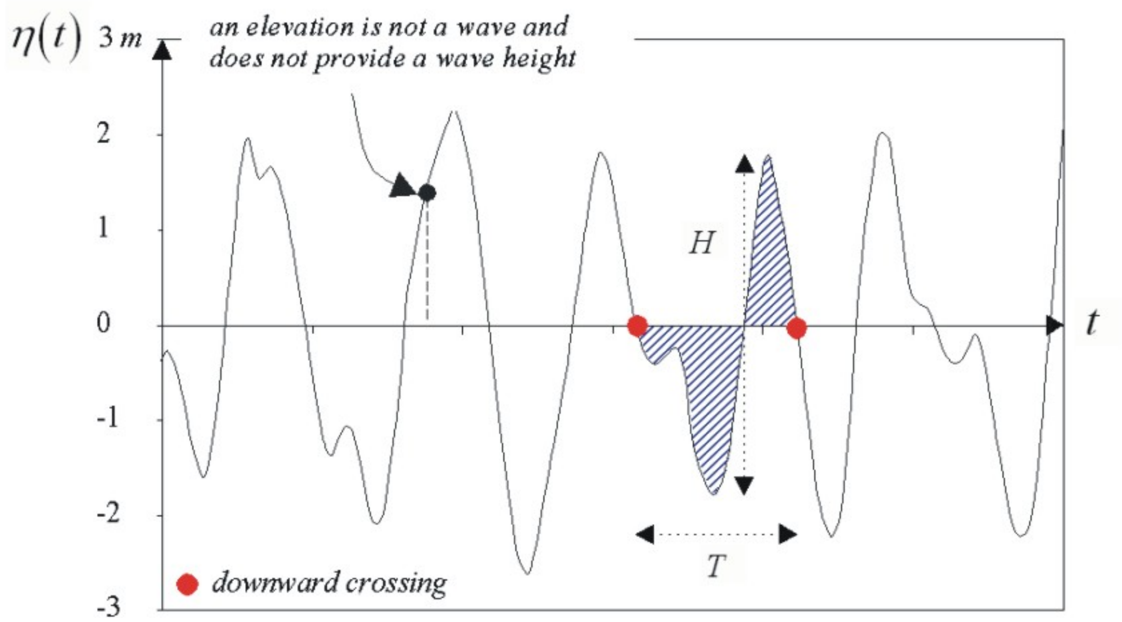

Figure 2.6: Definition of the wave height and period within a time series of the surface elevation (Source: Holthuijsen (2007))

Here, j is the rank number of the wave based on the wave height (e.g. j=1 is the highest wave, j=2 is the second-highest wave, etc.).
The significant wave height is very similar to the wave height that was measured visually in the past like it was mentioned above. This is the reason why this quantity is nowadays widely used in the field of oceanography (see Holthuijsen 2007).
The surface of the ocean often shows a chaotic structure and no defined properties of a wave can be identified. This structure can be interpreted as the sum of harmonic waves with varying wave heights and periods that were generated on different locations

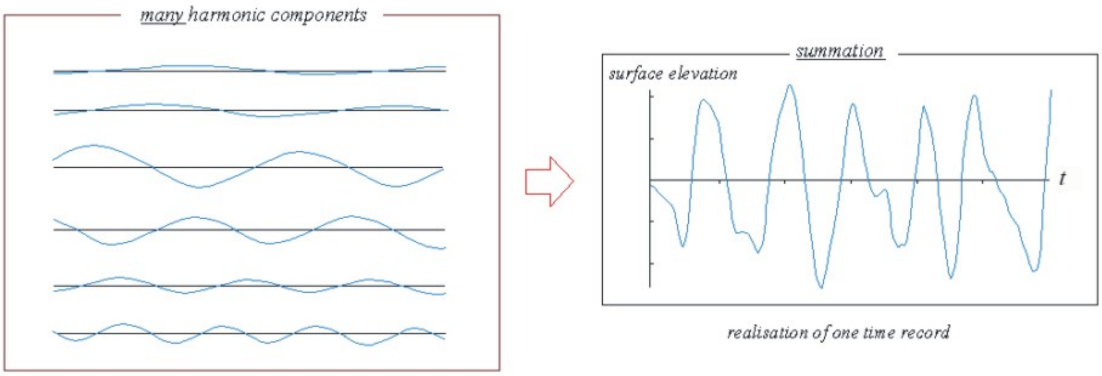

Figure 2.7: Sum of several harmonic waves with constant, but random, amplitudes and phases (Source: Holthuijsen (2007))

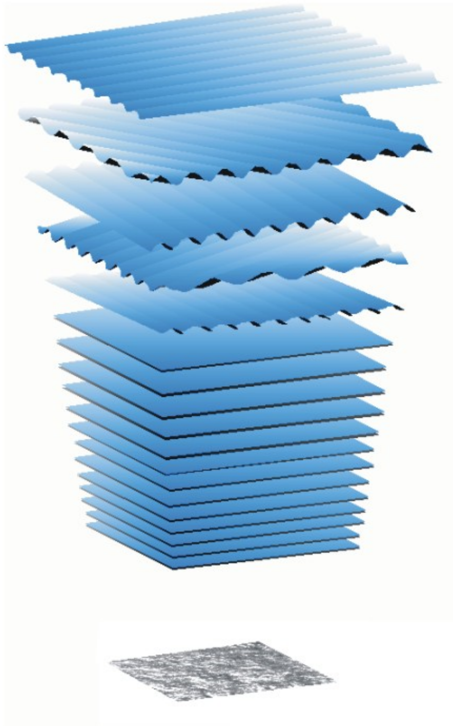

Figure 2.8: Sum of a high number of harmonic wave components (Source: Holthuijsen (2007))

with different wind conditions. The linear waves are statistically independent and they remain independent while they are traveling across the ocean (see figure 2.7). Following Holthuijsen (2007) the sum of these waves can be stated as follows:

$$\underline{\eta}(t) = \sum_{i=1}^{N_w} \underline{a_i} \cos\left(\underbrace{2\pi f_i}_{\sigma_i} t + \underline{\alpha_i}\right) \tag{2.68}$$

Here, N_w is the number of the different independent wave components (see figure 2.8), η, a, $f = 1/T$ and α are the surface elevation, wave amplitude, frequency and initial phase, respectively. Underlined quantities are random variables. In this section the notation σ is used for the relative angular frequency of the wave in the presence of an ambient current U_n that is directed normal to the wave crest:

$$\omega_a = \sigma + kU_n \tag{2.69}$$

The dispersion relation

$$\sigma^2 = gk \tanh kh \tag{2.70}$$

that describes the change of the frequency as a function of the water depth is retained. Here, $\omega_a = 2\pi f$ is the absolute angular frequency, λ or L is the wavelength, $k = 2\pi/\lambda$ is

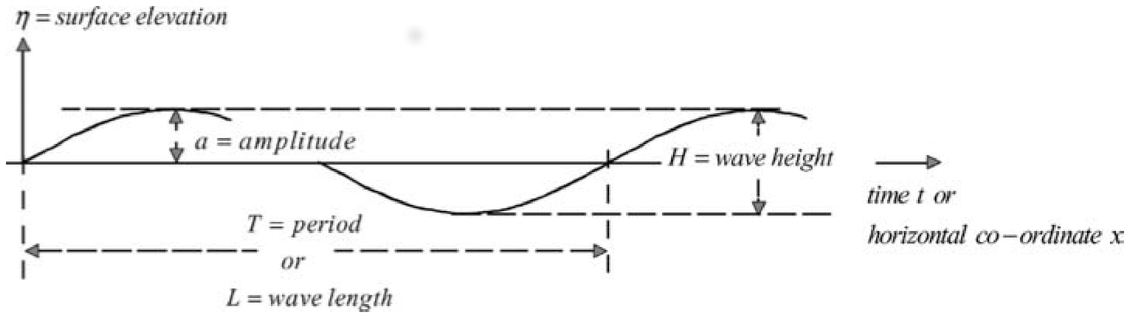

Figure 2.9: Some characteristic properties of an ocean wave (Source: Holthuijsen (2007))

the wave number and h is the depth (see figure 2.9).
To describe the processes of shoaling, refraction or energy transport especially in coastal areas it is important to introduce the phase and group velocity c and c_g, respectively (see Holthuijsen 2007):

$$c = L/T = \omega_a/k = \frac{g}{\omega_a}\tanh kh = \sqrt{\frac{g}{k}\tanh kh} \tag{2.71}$$

$$c_g = \frac{\partial\omega_a}{\partial k} = nc = \frac{1}{2}\left(1+\frac{2kh}{\sinh 2kh}\right)c \tag{2.72}$$

The phase velocity c describes the propagation speed of a traveling wave. This wave is called dispersive wave because it depends on the wavelength or frequency. The group velocity c_g can be identified as the velocity of a group of waves with different frequencies and wavelengths. The quantity n can be obtained from the dispersion relationship in equation 2.70 when ω_a is used instead of σ (see Holthuijsen 2007).

2.2.2 Transport of wave energy

The potential energy induced by a wave can be calculated as the difference between the potential energy in the water column with and without a wave on top of the ocean surface. The kinetic energy of a wave can be obtained from the orbital velocity components of the water particles using linear theory with second order accuracy. The expressions for the potential and kinetic energy of a harmonic wave are equal to each other and the total time-averaged wave induced energy density per unit horizontal area is (see Dean and Dalrymple 1991, Holthuijsen 2007)

$$\begin{aligned} E = E_{potential} + E_{kin} &= \overline{\int_0^\eta \rho g z dz} + \overline{\int_{-h}^{\eta} \frac{1}{2}\rho\,(u^2+w^2)\,dz} \\ &= \frac{1}{4}\rho g a^2 + \frac{1}{4}\rho g a^2 = \frac{1}{2}\rho g a^2 = \frac{1}{8}\rho g H^2. \end{aligned} \tag{2.73}$$

Here, the overbar denotes time-averaging.
Water particles do not travel with the speed of a propagating wave and stay close to their original position. They only move with the Stokes drift velocity that is usually much smaller than the orbital, phase or group velocity. Therefore, almost no mass is transported by a traveling wave train. However, energy is transported by a wave in the direction of propagation.
To calculate the energy transport or flux three contributions have to be taken into account (see Holthuijsen 2007). At first, the transport of potential energy in the x-direction through a cross-section Δz Δy in a time interval Δt has to be defined:

$$T_1 = \left(\int_{-h}^{\eta} (\rho g z) \, u dz \right) \Delta y \Delta t \tag{2.74}$$

Accordingly, the transport of the kinetic energy is calculated as follows:

$$T_2 = \left(\int_{-h}^{\eta} \left[\frac{1}{2} \rho \left(u^2 + w^2 \right) \right] u dz \right) \Delta y \Delta t \tag{2.75}$$

Additionally, there is also energy transported by the work done by the pressure:

$$T_3 = \left(\int_{-h}^{\eta} (pu) \, dz \right) \Delta y \Delta t \tag{2.76}$$

The pressure can be split up into the hydrostatic pressure and the wave-induced pressure:

$$T_3 = \left(\int_{-h}^{\eta} \left(-\rho g z + p_{wave} \right) u \right) \Delta y \Delta t \tag{2.77}$$

Summing these contributions up and using second-order approximation shows that only the wave-induced pressure contributes to the energy transport and the energy is transported in the wave direction. This effect can be understood by looking at the orbital movement of a water particle due to a traveling wave. While the water particle moves in the direction of the wave, the crest of the wave is passing by, so the surface elevation is high compared to the mean sea level which means the pressure in the water column is high. The movement of the water particle will then turn in the opposite direction while the wave trough is approaching the position of the water particle. Now, the surface elevation is low compared to the mean sea level which means, that the pressure in the water column is lower than before. Therefore, the wave-induced pressure is in phase with the surface elevation and the energy is transported in the wave direction as mentioned above.
To retain second-order accuracy it is only necessary to integrate up to the mean sea level (see Dean and Dalrymple 1991). Using an expression for the wave-induced pressure derived from a velocity potential function and the Bernoulli equation yields (see Holthuijsen

2007):

$$P \approx \overline{\int_{-h}^{0} (p_{wave} u)\, dz} = \left(\frac{1}{2}\rho g a^2\right) \frac{1}{2} \left(1 + \frac{2kh}{\sinh(2kh)}\right) \frac{\omega}{k} \tag{2.78}$$

Applying the equations 2.71, 2.73 and n from equation 2.72 leads to:

$$P = Enc = Ec_g \tag{2.79}$$

Thus, the wave energy is transmitted with the speed of the group velocity. It should be mentioned that P is the transport of energy due to waves. An ambient current will change direction and amount of transported energy.

2.2.3 Description of waves in the spectral domain

As mentioned above ocean waves follow a chaotic behaviour thus a description in the time domain is limited. This is the reason that most wave models utilise the variance density spectrum $E(f)$ that can be calculated using the Fourier transform of the auto-covariance of the surface elevation. The total variance of the surface elevation can be calculated using the spectrum as follows (see Holthuijsen 2007):

$$m_0 = \overline{\underline{\eta}^2} = \int_0^{+\infty} E(f) df \tag{2.80}$$

Again, the ovebar denotes that this is an time-averaged quantity and m_0 indicates that this is the zeroth-order moment of the spectrum.
The total energy per unit area can then be calculated using the variance:

$$E_{tot} = \rho g \overline{\underline{\eta}^2} \tag{2.81}$$

Therefore, the variance density spectrum can also be interpreted as an estimate for the energy density spectrum.
The significant wave height can also be estimated using the variance:

$$H_s \approx 4\sqrt{\overline{\underline{\eta}^2}} \tag{2.82}$$

This is the definition that is used in wave models for solving the governing equation of wave propagation in the spectral domain.
Assuming a Rayleigh distribution of the wave the root-mean-square of the wave height is:

$$H_{rms} = \frac{1}{2}\sqrt{H_s} \tag{2.83}$$

In figure 2.10 some spectra for different types of waves can be seen. It can be noticed that a higher number of different wave components will result in an expanded spectrum.

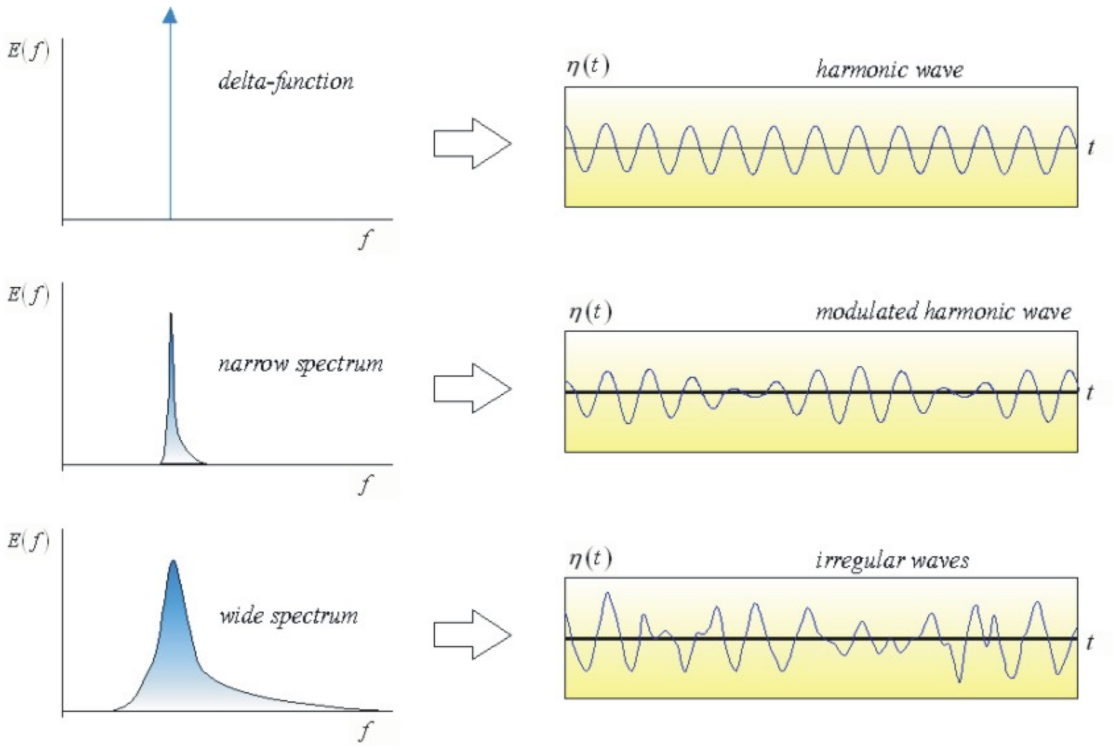

Figure 2.10: The energy spectra resulting from three different wave types (Source: Holthuijsen (2007))

The spectrum can also include spatial information. In figure 2.11 a southward directed swell generated close to the Norwegian coast can be seen. This swell meets a young wind sea generated by wind in an eastward direction at a certain location. It can be seen that the swell is propagating to the south and the young waves have different angles of propagation, mainly to the east. In the spectrum of the young waves frequencies higher than the ones from the swell are present. Here, the spectrum also depends on the wave direction Θ. If the two-dimensional spectrum is integrated over all possible directions, the result is an one-dimensional energy density spectrum, indicating that the energy carried by the young wave is higher than the energy transported by the swell.
With the equations defined in the spectral domain, it is also possible to give a definition of the energy transport or flux using spectral quantities. The wave energy flux of one wave is defined as the product of the energy density and the group velocity of the waves (see Cornett and Zhang 2008). To take the whole wave train into account this product has to be integrated over all wave frequencies and directions:

$$P = \rho g \int_0^{\infty} \int_0^{2\pi} c_g (\sigma, h) \, J (\sigma, \Theta) \, d\sigma d\Theta \tag{2.84}$$

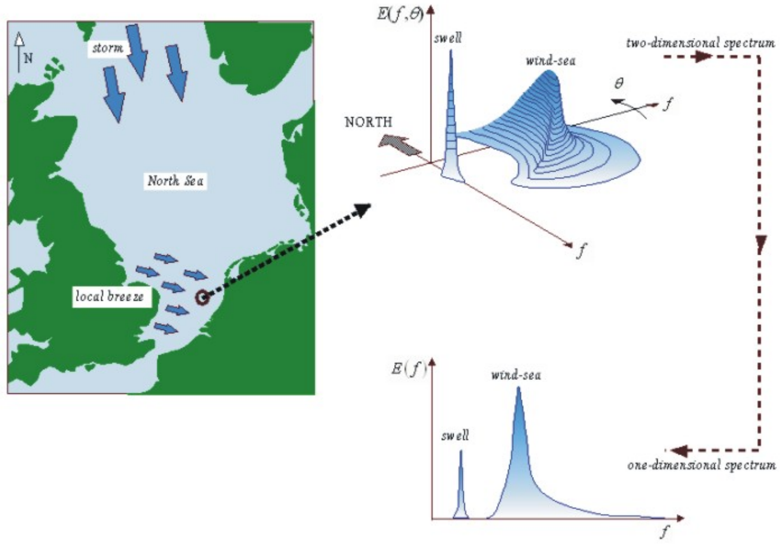

Figure 2.11: A southward directed swell meets local generated eastward directed waves. (Source: Holthuijsen (2007))

Here, $J(\sigma, \Theta)$ is the 2D wave spectrum, $c_g(\sigma, h)$ the group velocity as already used before. The group velocity of every single wave inside a wave train $c_g(\sigma, h)$ can be calculated using equations 2.71 and 2.72 and kh can be determined using an approximation given by Fenton and McKee (1990) (see also Holthuijsen 2007). The wave energy in a wave train can be calculated using equations 2.81 and 2.82:

$$E = \frac{1}{16}\rho g H_s^2 \tag{2.85}$$

An approximation of the wave energy flux per unit wave crest length produced by a wave train of irregular waves in any water depth can be estimated from the wave energy (see equation 2.85), the peak wave period T_p and the local water depth as

$$P \approx \frac{1}{16}\rho g H_s^2 c_g\left(\frac{1}{\alpha_E T_p}, h\right) \tag{2.86}$$

in which $c_g\left(\frac{1}{\alpha_E T_p}, h\right)$ is the group velocity of a wave with a period of $\alpha_E T_p$. The parameter α_E is a coefficient that depends on the shape of the wave spectrum and is shifting the peak period to lower periods. If a sea state is dominated by waves from a single source and the spectrum is uni-modal, Cornett and Zhang (2008) suggest a value of $\alpha_E \approx 0.9$.

2.2.4 Action balance equation

In wave models it is more common to use the action density instead of the energy density because the action density is conserved in presence of an ambient current. Following

Holthuijsen (2007) the action density is defined as:

$$N = E/\sigma \tag{2.87}$$

Using the action density the action balance equation can be stated in Cartesian coordinates as (see e.g. Hasselmann et al. 1973, Whitham 1974, Phillips 1977, Mei 1983):

$$\begin{aligned}\underbrace{\frac{\partial N(\sigma,\Theta;x,y,t)}{\partial t}}_{\text{Kinematics}} &+ \underbrace{\frac{\partial c_{g,x}N(\sigma,\Theta;x,y,t)}{\partial x} + \frac{\partial c_{g,y}N(\sigma,\Theta;x,y,t)}{\partial y}}_{\text{Propagation of the wave action density}} + \underbrace{\frac{\partial c_{\sigma}N(\sigma,\Theta;x,y,t)}{\partial \sigma}}_{\text{Shift in frequency}} + \\ &+ \underbrace{\frac{\partial c_{\Theta}N(\sigma,\Theta;x,y,t)}{\partial \Theta}}_{\text{Refraction}} = \frac{S_{tot}(\sigma,\Theta;x,y,t)}{\sigma}\end{aligned} \tag{2.88}$$

The first term describes the change of the action density in time. The second and third term represent the propagation of action density in space, also involving the process of shoaling (increase of wave height in shallow water), the fourth term describes the shifting of the relative frequency due to variations in depth and current and the fifth term represents the depth- and current-induced refraction (bending of waves when entering shallow water). The effects of diffraction may also be included. The source term for action density S_{tot}/σ describes the processes of generation and dissipation of action density and nonlinear wave-wave interactions:

$$\begin{aligned}S_{tot}(\sigma,\Theta) &= \underbrace{S_{in}(\sigma,\Theta)}_{\text{Wave growth by wind}} + \underbrace{S_{nl3}(\sigma,\Theta) + S_{nl4}(\sigma,\Theta)}_{\text{Nonlinear transfer of energy}} + \underbrace{S_{ds,w}(\sigma,\Theta)}_{\text{White-capping}} \\ &+ \underbrace{S_{ds,b}(\sigma,\Theta)}_{\text{Bottom friction}} + \underbrace{S_{ds,br}(\sigma,\Theta)}_{\text{Depth-induced wave breaking}}\end{aligned} \tag{2.89}$$

In the next sections these processes and their implementation into wave models will be explained.

2.2.5 Generation of energy by wind

Following Holthuijsen (2007) there are two mechanisms that contribute to the transfer of energy from the wind into the ocean surface. The first one can be described utilising a pressure pattern induced by the wind that moves over the water surface. The pressure pattern contains many different harmonic air-pressure waves. Some of them might have the same speed, direction and wavelength as some wave components of the water surface. In this case energy is transferred from the pressure waves to the water waves via resonance. This is the mechanism for the initial wave growth and can be described as (see Phillips

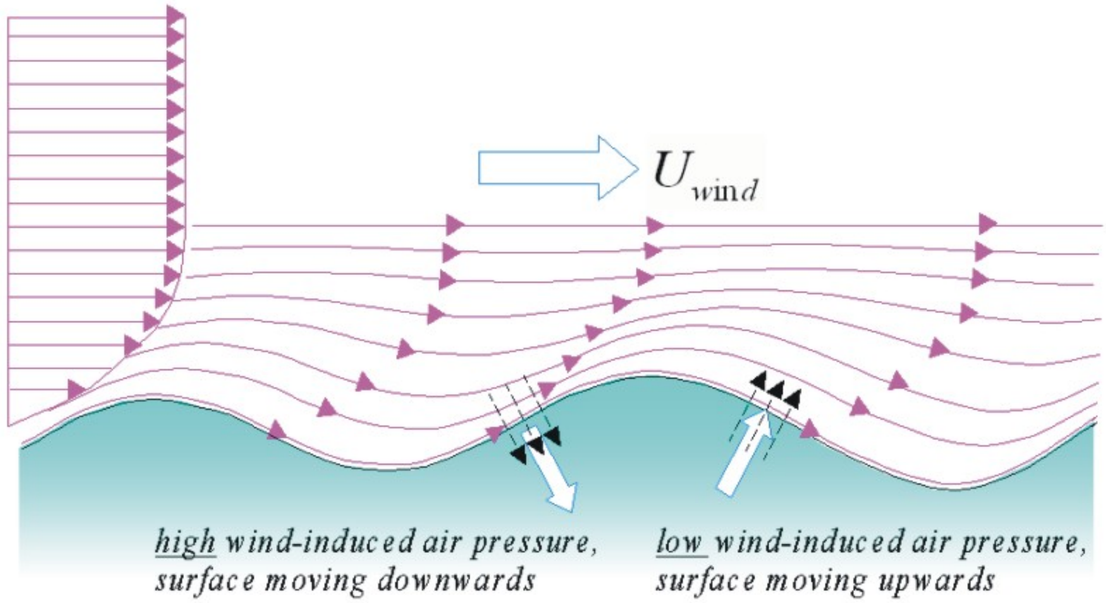

Figure 2.12: Wave growth by a positive-feedback mechanism (Source: Holthuijsen (2007))

1957):

$$S_{in,1}(\sigma, \Theta) = \alpha \text{ with } \alpha = \alpha\left(\sigma, \Theta; \vec{U}_{wind}\right) \tag{2.90}$$

Here, $\vec{U}_{wind}$ is the wind speed.

The second mechanism can be described as a positive-feedback mechanism (see Miles 1957). In figure 2.12 it can be seen that the wind-induced pressure is high at the windward side of the wave crest. Here, the water is pushed down. At the leeward side the pressure is low causing the ocean surface to rise. This effect is increased when the wave height increases what again increases the different pressure zones making the mechanism more and more effective. This is why a positive-feedback mechanism can be assessed here and be expressed as:

$$S_{in,2}(\sigma, \Theta) = \beta E(\sigma, \Theta) \tag{2.91}$$

It should be mentioned that this theory for wave growth assumes that small initial waves are already present what should be the case in an ordinary situation at sea.

There are several publications describing different procedures to calculate the energy input generated by wind (see Cavaleri and Rizzoli 1981, Snyder et al. 1981, Komen et al. 1984, 1994). Here, the method used in the preparation of this thesis is explained.

First, the wind velocity at a height of 10 m U_{10} has to be transformed into the friction velocity u_* at the ocean surface (see Holthuijsen 2007):

$$u_*^2 = C_D U_{10}^2 \tag{2.92}$$

C_D is the wind-drag coefficient that connects the wind speed to the friction velocity. This wind-drag coefficient is widely discussed in the literature. Here C_D is determined using the following expression (see Wu 1982):

$$C_D = \begin{cases} (0.8 + 0.065 U_{10}) \cdot 10^{-3} & \text{for } U_{10} > 7.5 \text{ m/s} \\ 1.2875 \cdot 10^{-3} & \text{else} \end{cases} \tag{2.93}$$

The energy input by wind is calculated using the initial wave growth and the feedback mechanism with the energy density spectrum:

$$S_{in}(\sigma, \Theta) = \alpha + \beta E(\sigma, \Theta) \tag{2.94}$$

The empirical expression of Cavaleri and Rizzoli (1981) is used to calculate the initial wave growth with a cut-off to avoid growth at frequencies lower than the Pierson-Moskowitz frequency (see Tolman 1992):

$$\alpha = \begin{cases} \frac{1.5 \cdot 10^{-3}}{g^2 2\pi} \left[u_* \cos\left(\Theta - \Theta_{wind}\right)\right]^4 G & \text{for } |\Theta - \Theta_{wind}| \leq 90^\circ \\ 0 & \text{for } |\Theta - \Theta_{wind}| > 90^\circ \end{cases} \tag{2.95}$$

The cut-off function is defined as

$$G = \exp\left(-\sigma/\sigma^*_{PM}\right)^{-4} \quad \text{with } \sigma^*_{PM} = 2\pi \frac{0.13 g}{28 u_*}. \tag{2.96}$$

Here, Θ_{wind} is the wind direction and σ^*_{PM} is the peak frequency of the Pierson-Moskowitz spectrum (see Pierson and Moskowitz 1964) which is a spectrum that describes a fully developed sea state.
The coefficient β for exponential wave growth is calculated following Snyder et al. (1981) and Komen et al. (1984):

$$\beta = \max\left(0, 0.25 \frac{\rho_{air}}{\rho_{water}} \left[28 \frac{u_*}{c} \cos\left(\Theta_{wave} - \Theta_{wind}\right) - 1\right]\right) \sigma \tag{2.97}$$

2.2.6 Nonlinear wave interactions

Following Holthuijsen (2007) there are two nonlinear wave interactions mechanisms. At first, there is the so-called triad wave-wave interaction. If two wave trains with different directions and frequencies meet, a diamond pattern of crests and troughs is created that has a wavelength, speed and direction on its own. This pattern consisting of the first two wave components would interact with a third wave component by resonance, if this wave component had the same wavelength, speed and direction as the pattern. Thus, there is an interaction between all three wave components and energy can be exchanged, but this

effect only occurs in shallow water and often generates a second peak at twice the peak frequency.
In deep water the conditions for resonance can not be fulfilled by three wave components. Here, two pairs of diamond patterns can interact and fulfill the resonance conditions if they have the same wavelength, speed and direction. This is called quadruplet wave-wave interactions. Again, energy can be exchanged. In fact, the quadruplet wave-wave interactions shift a small amount of energy of the spectrum to higher frequencies where the energy might be dissipated by white-capping (see section 2.2.7). A higher amount of energy is transferred to lower frequencies, thus shifting the peak of the spectrum to a lower frequency. In this way a spectrum can be stabilised by this interaction.
The triad wave-wave interactions are calculated using the lumped-triad approximation (LTA) (see Eldeberky 1996):

$$S_{nl3}\left(\sigma,\Theta\right) = S_{nl3}^{+}\left(\sigma,\Theta\right) + S_{nl3}^{-}\left(\sigma,\Theta\right) \tag{2.98}$$

Here, the term $S_{nl3}^{+}\left(\sigma,\Theta\right)$ is always positive, so that the wave component with the frequency σ receives energy from a wave component with the frequency $\sigma/2$. On the other hand the wave component with the frequency σ loses energy to a wave component with the frequency 2σ because the term $S_{nl3}^{-}\left(\sigma,\Theta\right)$ is always negative. In this way energy is transported to higher frequencies. The degree of nonlinearity of the waves in this interaction is represented by the Ursell number that describes the ratio of the amplitude of a harmonic wave and the amplitude of its second-order Stokes correction:

$$N_{Ursell} = HL^2/h^3 \tag{2.99}$$

For the calculation of the quadruplet wave-wave interactions the discrete-interaction approximation (DIA) of Hasselmann et al. (1985) is used. In this method two configurations of quadruplets with wave components that differ in some wave directions are calculated and combined to represent the redistribution of energy by the quadruplet interaction (see WAMDI group 1988):

$$S_{nl4}\left(\sigma,\Theta\right) = S_{nl4}^{*}\left(\sigma,\Theta\right) + S_{nl4}^{**}\left(\sigma,\Theta\right) \tag{2.100}$$

2.2.7 Dissipation by white-capping

The mechanisms of the energy dissipation due to white-capping are still under investigation. It has been proposed that the white-capping is connected to the steepness of the waves but observations have shown that the steepness only seems to provide a upper limit of a wave before breaking (see Holthuijsen 2007). The dissipative character of the white capping is locally nonlinear, but linear on average, thus it can be added as a source term

to the action balance equation in section 2.2.4.
A popular theory explaining the effect of white-capping is given by Hasselmann (1974). In this theory the white cap or white foam on the top of a slightly breaking wave acts as a pressure impulse at the leeward side of the wave crest. The weight of the white cap pushes the wave down causing energy to dissipate. Thus, the white cap counteracts in some way the generation of energy described in section 2.2.5 (see Holthuijsen 2007).
The expression of the source term follows the pulse-based model by Hasselmann (1974) as suggested by the WAMDI group (1988) as

$$S_{ds,w}(\sigma,\Theta) = -\mu k E(\sigma,\Theta) \tag{2.101}$$

and

$$\mu = C_w \left((1-n) + n\frac{k}{\tilde{k}}\right)\left(\frac{\tilde{s}}{\tilde{s}_{PM}}\right)^p \frac{\tilde{\sigma}}{\tilde{k}}. \tag{2.102}$$

Here, $\tilde{s} = \tilde{k}\sqrt{m_0}$ is the overall wave steepness (see Janssen 1991, Günther et al. 1992) and $\tilde{s}_{PM}$ is the steepness of the Pierson-Moskowitz spectrum with $\tilde{s}_{PM} = \sqrt{3.02 \cdot 10^{-3}}$ (see Pierson and Moskowitz 1964). In WAMDI group (1988) the definitions for the mean frequency and the mean wave number are given as:

$$\tilde{\sigma} = \left[m_0^{-1}\int_0^{2\pi}\int_0^{\infty}\sigma^{-1}E(\sigma,\Theta)\,d\Theta d\sigma\right]^{-1} \tag{2.103}$$

$$\tilde{k} = \left[m_0^{-1}\int_0^{2\pi}\int_0^{\infty}k^{-1/2}E(\sigma,\Theta)\,d\Theta d\sigma\right]^{-2} \tag{2.104}$$

Following Komen et al. (1984) the remaining parameters can be set as $C_w = 2.36 \cdot 10^{-5}$, $n = 0$ and $p = 4$. Alternative values for these parameters were presented by Günther et al. (1992).

2.2.8 Dissipation by bottom friction

In coastal areas the bottom friction is a very dominant factor for the energy dissipation because the water depth is relatively small and the orbital velocity is not zero at the bottom (see figure 2.13). Thus, this orbital motion interacts with the bottom and a thin turbulent layer is created where energy of the orbital motion is dissipated.
Following Holthuijsen (2007) the loss rate of energy due to bottom friction is:

$$D_b = -\tau_b u_b \tag{2.105}$$

Here, τ_b is the bottom shear stress and u_b is the velocity of a water particle close to the bottom. If they are oriented in the same direction, the time-averaged energy-dissipation

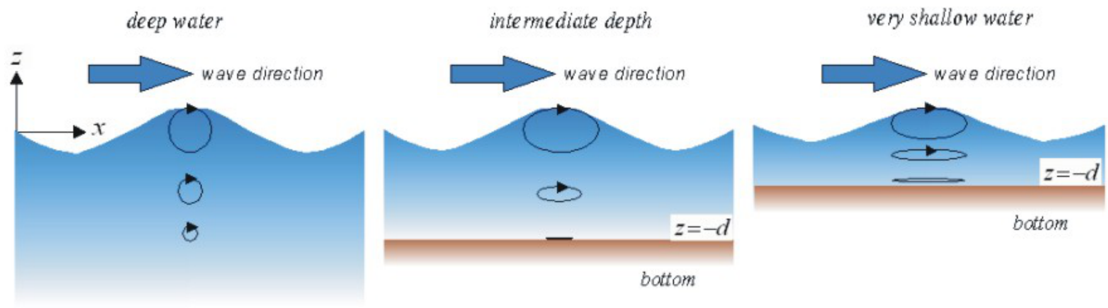

Figure 2.13: Orbital velocities of the water particles in different water depths (Source: Holthuijsen (2007))

rate at the bottom per unit bottom surface area is (see Holthuijsen 2007):

$$\overline{D_b} = -\overline{\tau_b u_b} \tag{2.106}$$

There are two approaches to determine the shear stress. The first method is for example used by Collins (1972). Here, the turbulent boundary layer at the bottom of the ocean is represented by a drag coefficient C_b that is utilised in a quadratic law to estimate the shear stress (see Putnam and Johnson 1949):

$$\tau_b = \rho C_b u_b^2 \tag{2.107}$$

Here, ρ is the density of water
Inserting this equation into equation 2.106 yields

$$\overline{D_b} = -\overline{\rho C_b u_b^2 u_b} \tag{2.108}$$

and is approximated for random waves by Collins (1972) as

$$\overline{D_b} = -\rho C_b u_{rms,b}^2 u_{rms,b}. \tag{2.109}$$

in which rms indicates that the root-mean-square of the orbital velocity is used.
The energy spectrum is obtained by replacing the square of the orbital velocity (see Holthuijsen 2007)

$$S_b^* (\sigma, \Theta) = -\rho_{water} C_b \left[\frac{\sigma}{\sinh (kd)}\right]^2 E(\sigma, \Theta)\, u_{rms,b} \tag{2.110}$$

with

$$u_{rms,b} = \left(\int_0^\infty \int_0^{2\pi} \left[\frac{\sigma}{\sinh (kd)}\right]^2 E(\sigma, \Theta)\, d\Theta d\sigma \right)^{1/2}. \tag{2.111}$$

And for the variance spectrum the following expression results from equation 2.110:

$$S_b(\sigma,\Theta) = -\frac{C_b}{g}\left[\frac{\sigma}{\sinh(kd)}\right]^2 E(\sigma,\Theta)\, u_{rms,b} \tag{2.112}$$

Following Hasselmann et al. (1973) the drag or bottom-friction coefficient for a swell can be calculated as

$$C_b = \frac{\chi}{g u_{rms,b}} \tag{2.113}$$

with a value of 0.038 m^2s^{-3} or 0.067 m^2s^{-3} as suggested by Bouws and Komen (1983) for a fully developed wind-sea.
In the second method used for example by Madsen et al. (1988) bottom-related parameters like the grain size are utilised to describe the energy dissipation due to the influence of the bottom. This approach is often used in combination with the calculation of sediment and bedload transport.

2.2.9 Dissipation by depth-induced breaking

A very popular model to calculate the energy dissipation due to wave breaking was presented by Battjes and Janssen (1978). In a single breaking wave the average energy loss per unit time and per unit horizontal bottom area is estimated using the inverse of the zero-crossing period $f_0 = 1/T_0$, the wave height H_{br} of the breaking wave and a tunable coefficient $\alpha_{br} \approx 1$ (see Holthuijsen 2007):

$$D_{br,wave} = -\frac{1}{4}\alpha_{br}\rho g f_0 H_{br}^2 \tag{2.114}$$

For random waves the joint probability density function of the wave height and the wave period $p(H_{br}, f_0)$ is used to calculate the average energy loss:

$$\overline{D}_{br,wave} = -\frac{1}{4}\alpha_{br}\rho g \int_0^\infty \int_0^\infty f_0 H_{br}^2 p(H_{br}, f_0)\, df_0 dH_{br} \tag{2.115}$$

The fraction of the breaking waves Q_{br} is used to calculate the loss for all waves:

$$\overline{D}_{br} = Q_{br}\overline{D}_{br,wave} \tag{2.116}$$

Battjes and Janssen (1978) then replaced the joint probability density function utilising a maximum wave height and the mean zero-crossing frequency f_0 and in terms of variance this yields:

$$\overline{D}_{br} = -\frac{1}{4}\alpha_{br} Q_{br}\overline{f_0} H_{max}^2 \tag{2.117}$$

It is then assumed that all unbroken waves with wave height smaller than H_{max} are Rayleigh distributed which leads to the following expression for Q_b:

$$\frac{1-Q_b}{\ln Q_b} = -\left(\frac{H_{rms}}{H_{max}}\right)^2 \tag{2.118}$$

This equation can be solved for example with the Newton-Raphson procedure. The root-mean-square of the wave height is $H_{rms} = \sqrt{8m_0}$. The maximum wave height can be

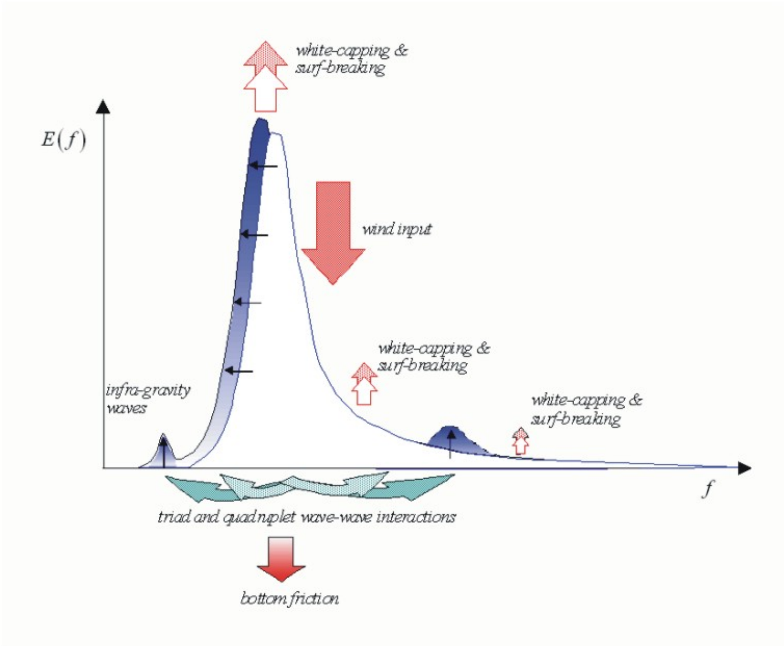

Figure 2.14: Energy flow in the wave spectrum (Source: Holthuijsen (2007))

estimated from the total water depth:

$$H_{max} = \gamma\left(h + \overline{\eta}\right) \tag{2.119}$$

The value of the coefficient γ is often taken as 0.73 (see Battjes and Stive 1985). Experiments showed that the corresponding spectral distribution of this dissipation rate can be represented using the relative frequency as

$$S_{ds,br} = \overline{D}_{br} E\left(\sigma, \Theta\right)/m_0. \tag{2.120}$$

2.2.10 Overview of all processes influencing the distribution of the wave spectrum

The source terms of the action balance equation (see equations 2.88 and 2.89) have been explained in the previous sections. The energy flow caused by the described processes can be seen in figure 2.14. The wind input is the main factor generating wave energy. The energy is dissipated by white-capping and close to the shore by bottom friction and depth-induced breaking. The wave-wave interactions redistribute energy inside the spectrum. The triad wave-wave interactions shift energy to higher frequencies thus creating new peaks at higher frequencies. The quadruplet wave-wave interactions shift energy and the peak frequency to lower frequencies and also to higher frequencies where the energy can be dissipated by white-capping or breaking.

2.3 Wave-current interactions

2.3.1 Radiation stress

The radiation stress is a phenomenon described in several publications (see e.g. Longuet-Higgins and Stewart 1964, Longuet-Higgins 1970, Mellor 2011). Longuet-Higgins and Stewart (1964) describe this effect as a flow of momentum that can also be observed in electromagnetic or acoustic waves (see e.g. Grashorn 2009). They define the radiation stress as the excess flow of momentum due to the presence of the waves.
To derive the expressions for the radiation stress Longuet-Higgins and Stewart (1964) consider a harmonic wave propagating in the x-direction over a uniform depth h. Then, the horizontal velocity u and the vertical velocity w of the orbital motion of the water particles are (see e.g. Dean and Dalrymple 1991):

$$u = a\sigma \frac{\cosh\left(k\left(h+z\right)\right)}{\sinh\left(kh\right)} \cos\left(kx - \sigma t\right) \tag{2.121}$$

$$w = a\sigma \frac{\sinh\left(k\left(h+z\right)\right)}{\sinh\left(kh\right)} \sin\left(kx - \sigma t\right) \tag{2.122}$$

Utilising the transfer of momentum ρu per unit volume at a rate u per unit time and following Longuet-Higgins and Stewart (1964) the total flux of momentum across a plane (x=constant) is:

$$I_x = \int_{-h}^{\eta} \left(p + \rho u^2\right) dz \tag{2.123}$$

Then, the radiation stress component S_{xx} is defined as the mean total flux of momentum minus the flux in the absence of waves with the hydrostatic pressure p_0:

$$S_{xx} = \overline{\int_{-h}^{\eta} (p + \rho u^2)\, dz} - \int_{-d}^{0} p_0 dz \tag{2.124}$$

This integral is now divided into three parts:

$$S_{xx}^{(1)} = \overline{\int_{-h}^{\eta} \rho u^2 dz} \quad (2.125)$$

$$S_{xx}^{(2)} = \overline{\int_{-h}^{0} (p - p_0)\, dz} \quad (2.126)$$

$$S_{xx}^{(3)} = \overline{\int_{0}^{\eta} p dz} \quad (2.127)$$

In the term $S_{xx}^{(1)}$ the integrand is of second order in amplitude (see equation 2.121), thus the contribution above the mean sea level will be of third order and can be neglected in a second-order approximation because there the integration interval again is proportional to the amplitude (see Holthuijsen 2007). The integration interval of the remaining part of the integral is constant in time and that leads to:

$$S_{xx}^{(1)} = \int_{-h}^{0} \rho \overline{u^2} dz \quad (2.128)$$

For term $S_{xx}^{(2)}$ the integration interval is also constant:

$$S_{xx}^{(2)} = \int_{-h}^{0} (\overline{p} - p_0)\, dz \quad (2.129)$$

With second-order accuracy the mean pressure in the water column at a certain position can be described by the combination of the mean wave-induced pressure (see figure 2.15) and the hydrostatic pressure $p_0 = \rho g z$ (see Longuet-Higgins and Stewart 1964):

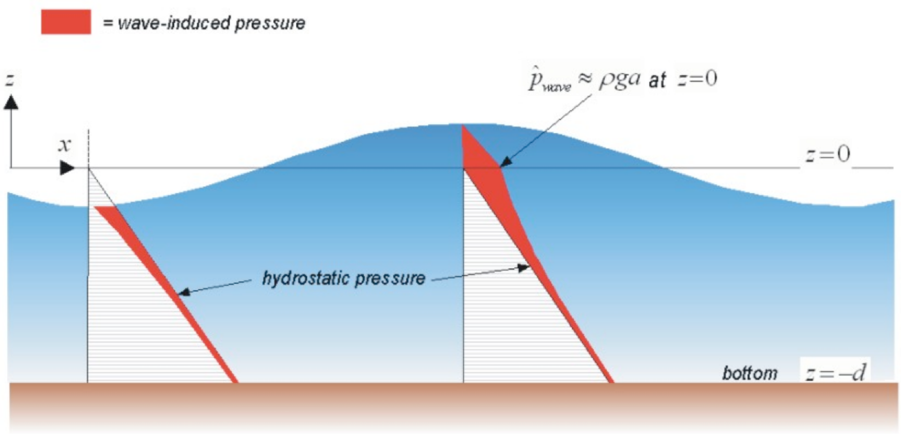

Figure 2.15: Wave-induced pressure (Source: Holthuijsen (2007))

$$\overline{p} = -\rho \overline{w^2} + \rho g z \quad (2.130)$$

Substituting equation 2.130 into equation 2.129 yields:

$$S_{xx}^{(2)} = \int_{-h}^{0} \left(-\rho\overline{w^2}\right) dz \tag{2.131}$$

Combining equations 2.128 and 2.131 and using equations 2.70, 2.121 and 2.122 will lead after integration to:

$$S_{xx}^{(1)} + S_{xx}^{(2)} = \frac{\rho g a^2 kh}{\sinh\left(2kh\right)} \tag{2.132}$$

The integration interval of the third term $S_{xx}^{(3)}$ can be reduced to the part above the mean sea level because the part below the mean sea level is constant in time. Following Longuet-Higgins and Stewart (1964) and Dean and Dalrymple (1991) the pressure below the free surface can be described as a combination of the hydrostatic pressure and the fluctuating part due to the wave motion:

$$p = \rho g \eta \frac{\cosh\left(k\left(h+z\right)\right)}{\cosh\left(kh\right)} - \rho g z \approx \rho g \eta - \rho g z \tag{2.133}$$

Substituting equation 2.133 and 2.81 into equation 2.127 and solving the integral yields:

$$S_{xx}^{(3)} = \frac{1}{2}\rho g \overline{\eta^2} = \frac{1}{2}E \tag{2.134}$$

Combining equation 2.132 and 2.134 leads to the final expression for the time-averaged transport of x-momentum in the x-direction per unit width and per unit time, the radiation stress component S_{xx}:

$$S_{xx} = \left(\frac{2kh}{\sinh\left(2kh\right)} + \frac{1}{2}\right) E = \left(2n - \frac{1}{2}\right) E \tag{2.135}$$

There is also a transport of momentum in the y-direction that can be derived in the same way as it has been done for the x-component, but this time the orbital velocities are zero and this results in (see Holthuijsen 2007)

$$S_{yy} = \left(n - \frac{1}{2}\right) E. \tag{2.136}$$

There is also a transport of x-momentum in the y-direction denoted by S_{xy} and a transport of y-momentum in the x-direction denoted by S_{yx}. These transports are zero for a wave traveling in the x-direction because it is assumed that there are no shear stresses and the orbital velocities in the y-direction are zero.

For a wave traveling at an angle Θ relative to the positive x-axis the shear components also contribute to the transport of momentum:

$$S_{xx} = \left(n - \frac{1}{2} + n\cos^2\Theta\right)E \tag{2.137}$$

$$S_{yy} = \left(n - \frac{1}{2} + n\sin^2\Theta\right)E \tag{2.138}$$

$$S_{xy} = S_{yx} = n\cos\Theta\sin\Theta E \tag{2.139}$$

This set of equations is called the radiation stress tensor (see Longuet-Higgins and Stewart 1964, Holthuijsen 2007).
Recently, Mellor (2011) derived vertically dependent wave radiation stress terms which are directly related to the equations derived by Longuet-Higgins and Stewart (1964) and Phillips (1977). Instead of neglecting Stokes drift and currents when addressing the problem of wave setup, he extended the equations for three-dimensional flow resulting in:

$$S_{\alpha\beta} = E\left[\frac{k_\alpha k_\beta}{k}e^{2kz} - \delta_{\alpha\beta}\left(ke^{2kz} - \frac{1}{2}\delta(z)\right)\right] \tag{2.140}$$

Both the Kronecker delta $\delta_{\alpha\beta}$ and the Dirac function $\delta(z)$ are used. In shallow water the equation given by Phillips (1977) can be derived by vertical integration (see Mellor 2011):

$$\int_{-h}^{\eta} S_{\alpha\beta}dz = E\left[\frac{k_\alpha k_\beta}{k^2}\frac{c_g}{c} + \delta_{\alpha\beta}\left(\frac{c_g}{c} - \frac{1}{2}\right)\right] \tag{2.141}$$

Here, α and β refer to horizontal coordinates.

2.3.2 Wave-induced set-down and set-up

Following Holthuijsen (2007) a gradient in radiation stress in a certain direction will create a force acting in the opposite direction :

$$F_x = -\frac{\partial S_{xx}}{\partial x} - \frac{\partial S_{xy}}{\partial y} \tag{2.142}$$

$$F_y = -\frac{\partial S_{yy}}{\partial y} - \frac{\partial S_{yx}}{\partial x} \tag{2.143}$$

The forces generated by the radiation stresses generate currents and change the mean surface elevation in the coastal area. Therefore, it is important to include those forces in the governing equations of an ocean model that is operated in coastal areas.
Close to the coast the gradient of the radiation stress is balanced by the hydrostatic pressure, thus a change in radiation stress in the x-direction will cause a change in the surface elevation and in a stationary situation this leads to:

$$\frac{dS_{xx}}{dx} + \rho g\left(h + \overline{\eta}\right)\frac{d\overline{\eta}}{dx} = 0 \tag{2.144}$$

If the elevation is very small $\overline{\eta} \ll h$, this simplifies to:

$$\frac{d\overline{\eta}}{dx} = -\frac{1}{\rho g h}\frac{dS_{xx}}{dx} \tag{2.145}$$

Thus, an increase of radiation stress will cause a decrease in surface elevation (set-down) and a decrease of radiation stress will result in an increase of the surface elevation (set-up).

Assuming an one-dimensional harmonic wave with a wave crest parallel to the coastline and that no energy dissipation occurs, then the variation of the wave amplitude is due to shoaling effects and using equation 2.135 leads to an expression for the set-down:

$$\overline{\eta} = -\frac{1}{2}\frac{a^2 k}{\sinh(2kh)} \tag{2.146}$$

This means that shoaling will cause a set-down and this effect depends only on the local depth, the wave amplitude and the wave number. In very shallow water this expression simplifies to

$$\overline{\eta} \approx -\frac{1}{16}\frac{H^2}{h}. \tag{2.147}$$

The elevation $\overline{\eta}$ is now proportional to the wave height which will be increasing before breaking and is inverse proportional to the depth which will be decreasing towards the coast. Thus, an overall set-down is caused.

After breaking the wave amplitude will decrease, which will also cause a decrease of the radiation stress. Then, the sign in equation 2.145 will change and an increase of the mean surface elevation (set-up) is caused. Assuming a non-dispersive wave in shallow water and using equations 2.73, 2.119 and 2.135 leads to:

$$\overline{\eta} = -\frac{3}{8}\gamma^2 \frac{d(h+\overline{\eta})}{dx} \tag{2.148}$$

The depth will decrease towards the shore, so the mean surface elevation will increase. Thus, an overall set-up is caused.

2.3.3 Longshore currents

One empirically based approach to estimate the magnitude of longshore currents caused by the radiation stress was presented by Longuet-Higgins (1970). He assumed a constant depth along the coast (y-direction) with waves approaching the coastline at a small angle of incidence Θ to the normal x perpendicular to the shoreline. The stress exerted by the waves into the y-direction can be described as follows:

$$\tau_y = -\frac{\partial}{\partial x}\frac{\sin\Theta}{c} E c_g \cos\Theta \tag{2.149}$$

The longshore component of the bed shear stress can be modelled using a longshore component of the current v and the orbital velocity vector $\vec{u}$:

$$\tau_y^b = \rho c_f \overline{|\vec{u}|} \overline{v} \tag{2.150}$$

Combining equation 2.149 and 2.150 by assuming a balance between both equations and neglecting the exchange of momentum due to horizontal turbulent eddies leads to:

$$\frac{2}{\pi} c_f \rho u_{max} \bar{v} = \frac{5}{4} \rho u_{max}^2 \left(s \sin \Theta\right) \tag{2.151}$$

The left part of the equation describes the bottom friction with the empirical bottom friction coefficient c_f the water density ρ and the maximum horizontal orbital velocity u_{max}. The right side of the equation represents the stress exerted by the waves with a gradual bottom slope s and the angle of incidence that was already mentioned above. A rough estimate of mixing processes is obtained by using a mixing length L at both sides of the breaker line that is connected to the width x_b of the surf zone by a coefficient γ_b. This coefficient can be substituted by the constant β_b that can vary between 0.167 and 0.5. Using β_b to describe the relationship between the current velocity in deep water and the velocity at the breaker line and α_b as the relationship between the wave amplitude and the maximum wave height results in an expression of the longshore velocity v_{LH} caused by waves at the breaker line in front of the coast

$$v_{LH} = \frac{5\pi}{8} \frac{\alpha_b \beta_b}{c_f} \left(g h_B\right)^{1/2} \left(s \sin \Theta_B\right) \tag{2.152}$$

where g is the gravitational acceleration, h_B is the height of the wave at the breaker line and the index LH refers to the longshore current velocity derived by Longuet-Higgins (1970).

Another approach to calculate the velocity of longshore currents caused by waves was presented by Thornton and Guza (1986). Assuming that the wave is stationary and parallel contours of the bathymetry compared to the wave crest, they give the energy flux balance equation with the average dissipation $\overline{\epsilon_b}$ as:

$$\frac{dEc_g \cos \Theta}{dx} = \overline{\epsilon_b} \tag{2.153}$$

The distribution of breaking waves is described as a weighted Rayleigh distribution and by multiplying the dissipation for a single broken wave by the probability of wave breaking and integrating over all wave heights results in an average dissipation

$$\overline{\epsilon_b} = \frac{3}{16} \sqrt{\pi} \rho g \frac{B^3}{\gamma^4 h^5 f_p H_{rms}^7} \tag{2.154}$$

where B, f_p and H_{rms} are the breaker type coefficient, the peak frequency and the wave height, respectively. The coefficient γ describes the relationship between the wave height and the depth:

$$H_{rms} = \gamma h \tag{2.155}$$

Combining equation 2.153 and 2.154 and replacing the energy with

$$E = \frac{1}{8}\rho g H_{rms}^2 \tag{2.156}$$

leads after integrating to an analytical solution for the wave height

$$H_{rms} = a^{1/5} h^{9/10} \left[1 - h^{23/4}\left(\frac{1}{h_0^{23/4}} - \frac{a}{r_0^{5/2}}\right)\right]^{1/5}, \tag{2.157}$$

$$0 \leq h \leq h_0$$

with

$$r_0 = H_0^2 h_0^{1/2}$$

and

$$a = \frac{23}{15}\left(\frac{g}{\pi}\right)^{1/2} \frac{\gamma^4 \tan\beta_s}{B^3 f_p}$$

The index 0 refers to the conditions at the most offshore shallow water location. It is assumed that the incident wave angle is smaller than 9° and the wave travels in shallow water on a plane beach with a slope $\tan\beta_s$. To calculate the longshore current velocity the radiation stress given by Longuet-Higgins (1970) and Snell's law of linear wave refraction are used to give a relationship between change in energy flux and breaking wave dissipation:

$$\frac{d}{dx}S_{yx} = \frac{\sin\Theta_0}{c_0}\frac{d}{dx}\left(E c_g \cos\Theta\right) = \frac{\sin\Theta_0}{c_0}\overline{\epsilon_b} \tag{2.158}$$

The alongshore momentum equation can be written as:

$$\frac{\sin\Theta_0}{c_0}\overline{\epsilon_b} = -\frac{d}{dx}S'_{yx} - t_y^b \tag{2.159}$$

The term S'_{yx} represents the turbulent component of the radiation stress and is subsequently neglected. The same formulation as in Longuet-Higgins (1970) for the bed shear stress is used here (see equation 2.150). Therefore, for a small angle of incidence and a weak mean longshore current the longshore current velocity induced by waves can be calculated as:

$$v_{TG} = \frac{3}{4} \frac{B^3 f_p g^{1/2}}{c_f \gamma^4} \frac{\sin\Theta_0}{c_0} \frac{H_{rms}^6}{h^{9/2}} \tag{2.160}$$

The index TG refers to the longshore current velocity derived by Thornton and Guza (1986). The orbital velocity was replaced here by using linear, shallow water wave theory and the Rayleigh wave height distribution and the dissipation term was substituted by equation 2.154. With equation 2.157 an analytical solution for a plane sloping beach limited to shallow water can be derived:

$$\begin{aligned} v_{TG} = \; & \tfrac{23}{20} \frac{g}{\pi^{1/2}} \frac{a^{1/5}}{c_f} \tan\beta_s \frac{\sin\Theta_0}{c_0} \\ \cdot \; & h^{9/10} \left[1 - h^{23/4} \left(\frac{1}{h_0^{23/4}} - \frac{a}{r_0^{5/2}} \right) \right]^{-6/5}, \end{aligned} \tag{2.161}$$

$$0 < h < h_0 \leq L/20$$

Here, L is the wavelength and a and r_0 are defined in 2.157.

2.4 Governing equations including wave-current interactions

Mellor (2003, 2005, 2008) describes the governing primitive equations in sigma coordinates as follows:

$$\frac{\partial uD}{\partial t} + \frac{\partial u^2 D}{\partial x} + \frac{\partial uvD}{\partial y} + \frac{\partial u\omega}{\partial \sigma} - fvD \tag{2.162}$$

$$= -D\frac{\partial}{\partial x}\left(g\eta + p_{atm}\right) - D\int_{\sigma}^{0}\left(D\frac{\partial b}{\partial x} - \sigma\frac{\partial D}{\partial x}\frac{\partial b}{\partial \sigma}\right)d\sigma$$

$$-\left(\frac{\partial DS_{xx}}{\partial x} + \frac{\partial DS_{xy}}{\partial y}\right) + \sigma\left(\frac{\partial D}{\partial x}\frac{\partial S_{xx}}{\partial \sigma} + \frac{\partial D}{\partial y}\frac{\partial S_{xy}}{\partial \sigma}\right) + \frac{\partial \tau_x}{\partial \sigma}$$

$$\frac{\partial vD}{\partial t} + \frac{\partial uvD}{\partial x} + \frac{\partial v^2 D}{\partial y} + \frac{\partial v\omega}{\partial \sigma} + fuD \tag{2.163}$$

$$= -D\frac{\partial}{\partial y}\left(g\eta + p_{atm}\right) - D\int_{\sigma}^{0}\left(D\frac{\partial b}{\partial y} - \sigma\frac{\partial D}{\partial y}\frac{\partial b}{\partial \sigma}\right)d\sigma$$

$$-\left(\frac{\partial DS_{xy}}{\partial x} + \frac{\partial DS_{yy}}{\partial y}\right) + \sigma\left(\frac{\partial D}{\partial x}\frac{\partial S_{xy}}{\partial \sigma} + \frac{\partial D}{\partial y}\frac{\partial S_{yy}}{\partial \sigma}\right) + \frac{\partial \tau_y}{\partial \sigma}$$

$$\frac{\partial Du}{\partial x} + \frac{\partial Dv}{\partial y} + \frac{\partial \omega}{\partial \sigma} + \frac{\partial \eta}{\partial t} = 0 \tag{2.164}$$

$$\frac{\partial T_{pot}D}{\partial t} + \frac{\partial T_{pot}uD}{\partial x} + \frac{\partial T_{pot}vD}{\partial y} + \frac{\partial T_{pot}\omega}{\partial \sigma} = \frac{1}{D}\frac{\partial}{\partial \sigma}\left(K_h\frac{\partial T_{pot}}{\partial \sigma}\right) + D\hat{H} + DF_{T_{pot}} \tag{2.165}$$

$$\frac{\partial SD}{\partial t} + \frac{\partial SuD}{\partial x} + \frac{\partial SvD}{\partial y} + \frac{\partial S\omega}{\partial \sigma} = \frac{1}{D}\frac{\partial}{\partial \sigma}\left(K_h\frac{\partial S}{\partial \sigma}\right) + DF_S \tag{2.166}$$

$$\rho = \rho\left(T_{pot}, S\right) \tag{2.167}$$

Here, x and y are the cartesian east and north directions respectively, and $\sigma = \frac{z-\eta}{D} = \frac{z+h}{D} - 1$ is the vertical terrain-following σ-coordinate; u and v are the corresponding components of the velocities in the x- and y-direction and ω is the velocity normal to the sigma surfaces that has to be set to 0 at the surface and the bottom of the water column (see Mellor 2008); τ_x and τ_y are the corresponding components of the wind stress; η is the sea surface elevation; h is the mean water depth; $D = h + \eta$ is the total water depth; T_{pot} the potential temperature; S the salinity; ρ is the density; p_{atm} is the air pressure; b is the buoyancy; f is the Coriolis parameter; $\hat{H}$ is the solar irradiance; K_h is the thermal vertical eddy diffusion coefficient; $F_{T_{pot}}$ and F_s represent the thermal and salt diffusion terms. The modified Mellor and Yamada level 2.5 (MY-2.5) as modified by Galperin et al. (1988) and Smagorinsky turbulence closure schemes are utilised as default setups for vertical and horizontal mixing, respectively (see Mellor and Yamada 1982, Smagorinsky 1963, Wu et al. 2011). S_{xx}, S_{yy}, S_{xy} and S_{yx} are the radiation stress terms that describe the wave-current interactions and are defined by Mellor (2008) as

$$S_{xx} = kE\left(\frac{k_x^2}{k^2}F_{CS}F_{CC} - F_{SC}F_{SS}\right) + E_D \tag{2.168}$$

$$S_{yy} = kE\left(\frac{k_y^2}{k^2}F_{CS}F_{CC} - F_{SC}F_{SS}\right) + E_D \tag{2.169}$$

$$S_{xy} = S_{yx} = kE\frac{k_x k_y}{k^2}F_{CS}F_{CC} \tag{2.170}$$

with the wave energy E

$$E = \frac{1}{2}ga^2 = \frac{1}{16}gH_s^2 \tag{2.171}$$

that can be seen as the sum of the kinetic and the potential wave energies and

$$E_D = 0 \text{ if } z \neq \eta \text{ and } \int_{-h}^{\eta^+} E_D dz = E/2. \tag{2.172}$$

Here, k_x, k_y and k are the wave numbers in the x-direction, in the y-direction and the absolute wave number, respectively and H_s is the significant wave height. The terms F_{SS}, F_{SC}, F_{CS} and F_{CC} are defined as follows:

$$F_{SS} \equiv \frac{\sinh k\,(z+h)}{\sinh kD} \tag{2.173}$$

$$F_{SC} \equiv \frac{\sinh k\,(z+h)}{\cosh kD} \tag{2.174}$$

$$F_{CS} \equiv \frac{\cosh k\,(z+h)}{\sinh kD} \tag{2.175}$$

$$F_{CC} \equiv \frac{\cosh k\,(z+h)}{\cosh kD} \tag{2.176}$$

This set of governing equations has been implemented into the source code of FVCOM to account for the wave-current interactions based on the radiation stress approach (see section 3.

The wave action equation for σ-coordinates can also be found in this publication.

2.5 Alternative approaches to estimate the wave-current interactions

Lane et al. (2007) compare the concepts of the radiation stress and the vortex force. Following their argumentation the wave-averaged effects of the waves on the currents are considered as the divergence of a stress tensor by the radiation stress approach. In the vortex force representation two components are utilised to explain the effect of the waves: the gradient of a Bernoulli-head and a vortex force. The vortex force is shown to represent an interaction between the vorticity of the flow and the Stokes drift after wave averaging and this force can be derived from the radiation stress representation. McWilliams et al. (2004) presented coupled equations similar to the set of equations presented in section 2.4 using a vortex force representation. Lane et al. (2007) state that there are some inconsistencies in the radiation stress approach and the physical decomposition is missing.

There are also other publications dealing with the choice of a radiation stress or vortex force representation of the wave effects. Ardhuin et al. (2008a) proposed some corrections for the governing equation using the radiation stress representation. In a reply by Mellor (2008) the governing equations were corrected. Bennis and Ardhuin (2011) stated that the equations presented in Mellor (2008) are inconsistent with the depth-integrated momentum balances in the presence of a sloping bottom thus producing unrealistic surface elevations and currents. They encourage ocean modelers to use the governing equations presented in McWilliams et al. (2004) and Ardhuin et al. (2008b). The publication by Mellor (2011) about the radiation stress representation was then motivated by the publications of McWilliams et al. (2004) and Ardhuin et al. (2008b). Moghimi et al. (2012) tested both representations using a 3D ocean model. The vortex force representation showed significant deviations from measurements but the results were still physically reasonable. The radiation stress approach showed unrealistic offshore-directed transport in the wave-shoaling regions and close to steep bathymetry.

However, the discussion on these topics is still ongoing and ocean modellers are curious of its outcome. This thesis focuses on the radiation stress representation because it is used in the source code of the model and the developers published some promising papers showing the realistic behavior of the coupling (see section 3.3).

3 FVCOM

In this chapter the ocean modelling system FVCOM is described in detail. In section 3.1 the finite volume method is introduced. The structure of FVCOM and its components are explained in section 3.2 and some key publications with FVCOM are presented in section 3.3. The procedure of creating a FVCOM model setup is described in section 3.4. In the last section 3.5 a problem concerning the FVCOM source code is presented.

3.1 Finite Volume Method (FVM)

The finite volume method is part of the weighted residual methods and assumes in contrast to finite difference methods that the solution can be represented analytically (see Fletcher 1991). It is closely related to finite difference methods and a FVM can often be interpreted as a finite difference approximation to the differential equation (see LeVeque 2002). A big advantage of the FVM is that the total mass within the computational domain is preserved or varies correctly provided proper boundary conditions are applied. The possibility to use a arbitrarily-sized triangular grid is another advantage of the FVM (see Chen et al. 2006a). Heinzl (2007) and Barth and Ohlberger (2004) give detailed descriptions of the FVM which are summarized here.

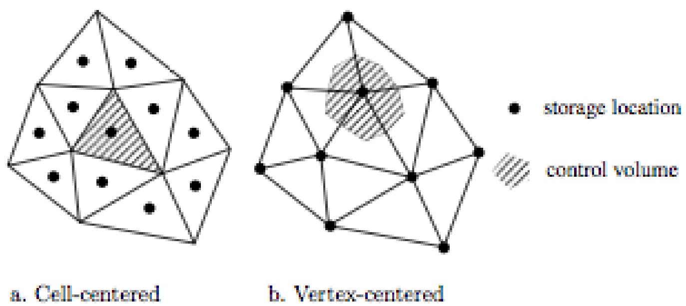

Figure 3.1: Different methods to form the control volumes for the finite volume method: (a) cell-centered and (b) vertex-centered control volume method (Source: Barth and Ohlberger (2004))

As a prototype the following divergence equation of the conservation law can be considered:

$$\partial_t u + \nabla \cdot f(u) = 0 \tag{3.1}$$

Here, u is the density of a tracer and $f(u)$ is the flux of this tracer.
The computational domain Ω of the area of interest is subdivided into cells (here triangles) and the applied equations are solved in an integral form on these cells. For this purpose the domain is again subdivided into non-overlapping control volumes V_i (see figure 3.1). In each of these control volumes an integral conservation law is imposed by spatial integration of equation 3.1 and application of the divergence theorem. For a fixed control volume V with a boundary ∂V the equation for the integral conservation law is

$$\partial_t \int_V u \; dV + \int_{\partial V} f(u) \cdot dA = 0. \tag{3.2}$$

Here, the nature of the normal dA depends on the number of dimensions used. Figure 3.1 shows two different methods to form the control volumes. In figure 3.1a the cell-centered finite volume method is shown. The triangles themselves are the control volumes and the calculated variables are stored in the center of the triangle. Figure 3.1b depicts the vertex-centered finite volume method. Here, the variables are stored in the nodes of the triangles. Both methods are used in FVCOM. Equation 3.2 can then be solved using the control volume cell average of every control volume and calculating the fluxes under certain assumptions (see Heinzl 2007, Barth and Ohlberger 2004).

3.2 The structure of FVCOM

The computations were performed with the modelling system FVCOM, version 3.1.4. The Fortran-based FVCOM is a prognostic, unstructured-grid, finite-volume, free-surface, 3D primitive equations ocean model that was originally developed by Chen et al. (2003). Following Chen et al. (2006a) it combines the best attributes of finite-difference methods for simple discrete coding and computational efficiency and finite-element methods for geometric flexibility. The descriptions of the structure of FVCOM and its coding were taken from the user manual (see Chen et al. 2006a) or directly extracted from the source code.

3.2.1 Summary of some theoretical aspects of the FVCOM model

In section 2.1 the theoretical framework of FVCOM was explained and can be summarised briefly here. The governing equations are solved either in a 2D- or 3D-mode using terrain-following σ- and spherical coordinates to account for the influence of the Coriolis force on the dynamics. The surface and bottom boundary conditions and friction effects are calculated using drag coefficients and a logarithmic boundary layer at the bottom. The bottom drag coefficient has been restricted by the developers to a maximum value cal-

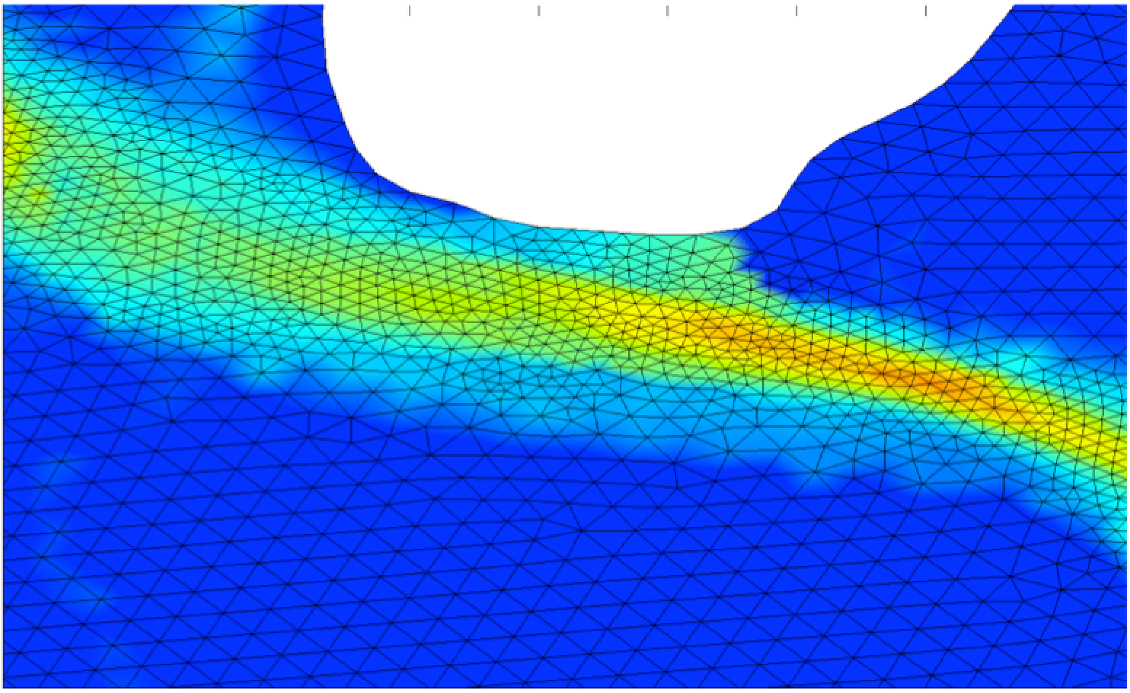

Figure 3.2: Grid with high resolution in the tidal channel in the East-Frisian Wadden Sea and an accurate representation of the coastline

culated with equation 2.23 for a depth of 3 m. Smaller depths will give the same drag coefficient. Otherwise the logarithmic function would become very small for very shallow water and produce unrealistic high values for the drag coefficient.
The chosen turbulence closure model for this thesis is the MY-2.5 model that was described in section 2.1.4, but had to be modified as outlined in section 3.5.

3.2.2 The triangular unstructured-grid approach and the resulting time step

The triangular unstructured-grid approach of FVCOM has some advantages compared to a structured-grid model. In figure 3.2 it can be seen that a triangular grid can provide an accurate representation of the coastline. In regions with a high interest the resolution can be refined with respect to e.g. the bathymetry and in outer domains the resolution can become very coarse. In this way the number of the nodes and the triangles are kept small, thus the costs of the computations are low, too. Structured-grid models do not have the opportunity to chose a high resolution in certain areas with just one model setup. Here, a nesting approach must be chosen which will increase the computing time.
In figure 3.3 a comparison of an unstructured grid and a structured grid can be seen. It can be clearly identified that it is impossible to achieve a representation of the coastline as good as the one created by using an unstructured grid with a similar resolution. An exception might be a curvilinear grid. But this approach will produce a very coarse reso-

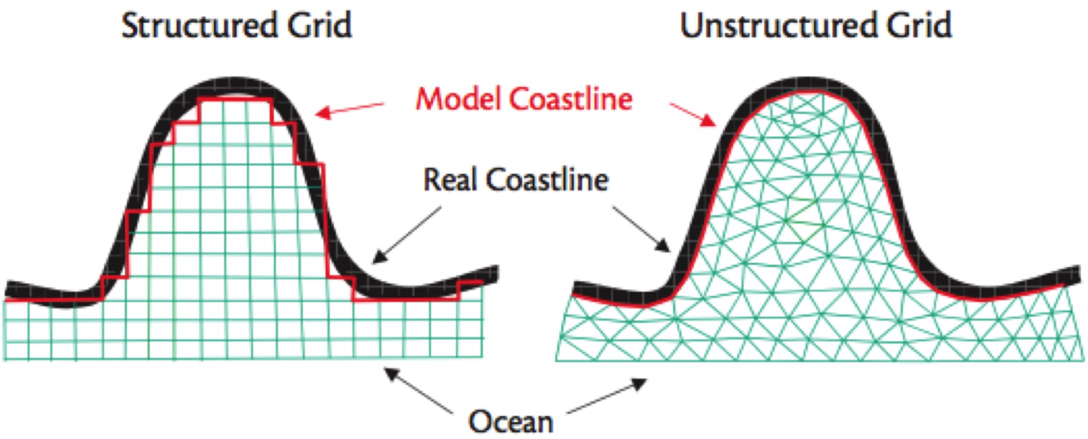

Figure 3.3: Example of a structured grid (left) and an unstructured grid (right) (Source: Chen et al. (2006b))

lution in areas that are not located close to the coast.

The ocean model FVCOM solves the integral form of the governing equations for momentum, continuity, temperature, salinity and density by calculating the fluxes over a triangular grid composed of non-overlapping horizontal control volumes using multi-stage time-stepping approaches as e.g. a modified fourth-order Runge-Kutta time-stepping scheme. The time step depends on the chosen grid size. The ratio between the internal and the external time step should be

$$I_{split} = \frac{\Delta t_I}{\Delta t_E} \leq 10 \tag{3.3}$$

and was chosen to be 5 (see section 2.1.3), because by using this value the probability of a stable model run with realistic results is high. The maximum time step for the external mode can be calculated using the Courant-Friedrichs-Lewy condition (CFL):

$$\Delta t_E \leq \frac{\Delta L}{U + \sqrt{gD}} \tag{3.4}$$

Here, ΔL is the shortest edge of an individual triangular grid element, U is the magnitude of the horizontal velocity and D is the local depth. With typical values for an East-Frisian Wadden Sea tidal channel with a high current velocity ($D = 25$ m, $g = 9.8$ m/s, $U = 1.5$ m/s) and a grid resolution of 50 m the external time step would be around 2.5 s. In fact, the time step had to be chosen as 0.4 s. Otherwise, the model became unstable.

For FVCOM it is possible to use a semi-implicit scheme that can be tuned by a factor determining the ratio between the explicit and implicit scheme. An implicit scheme allows higher time steps without stability issues during the calculations and thus a decrease in computation time can be achieved. Here, the semi-implicit scheme was not used because some irregularities appeared during the performance of a simple test case.

3.2.3 Calculation of the variables

In FVCOM not all variables are calculated or placed at the same positions. Tracers as e.g. temperature, salinity or surface elevation are calculated on each node of the unstructured

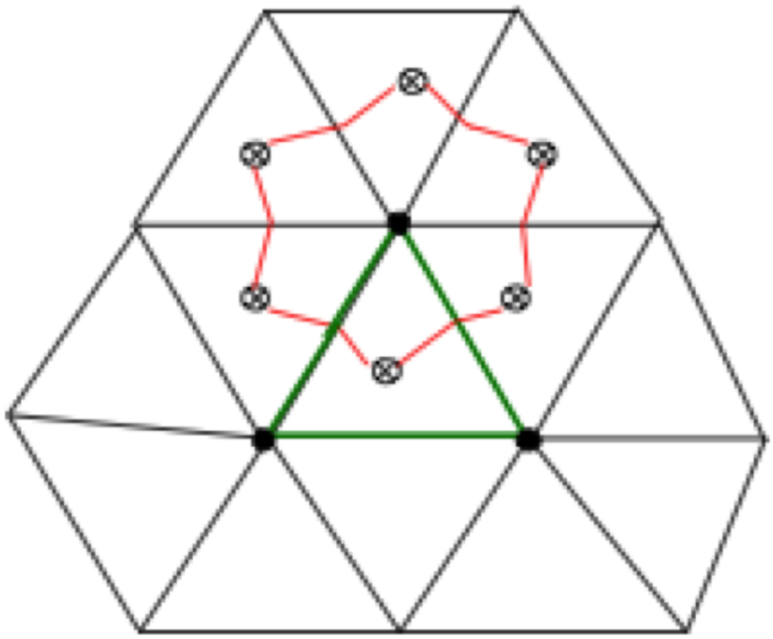

Figure 3.4: Example of a TCE (Tracer Control Element) framed with a red line and a MCE (Momentum Control Element) framed with a green line (Source: Chen et al. (2006a))

triangles while the velocities are calculated at the center of a triangle (see figure 3.4 and section 3.1). The separation has to be done due to numerical restrictions. Otherwise there will be numerical errors in the calculated results (see e.g. Versteeg and Malalasekera 2007). The scalar variables at each node are calculated by the net flux through the sections linked to the centre of the triangles and the mid-point of the adjacent sides in the surrounding triangle (tracer control element or TCE). The velocities at the centroids are determined using the net flux through the three sides of this triangle (momentum control element or MCE). In the vertical direction σ-layers are used to have an accurate representation of the bathymetry (see figure 3.5). All model variables are calculated on the mid-level of the layers, except the vertical velocity ω which is calculated on the layer surfaces. Different structures of the σ-coordinate can be used, but in this thesis an equidistant structure was chosen.

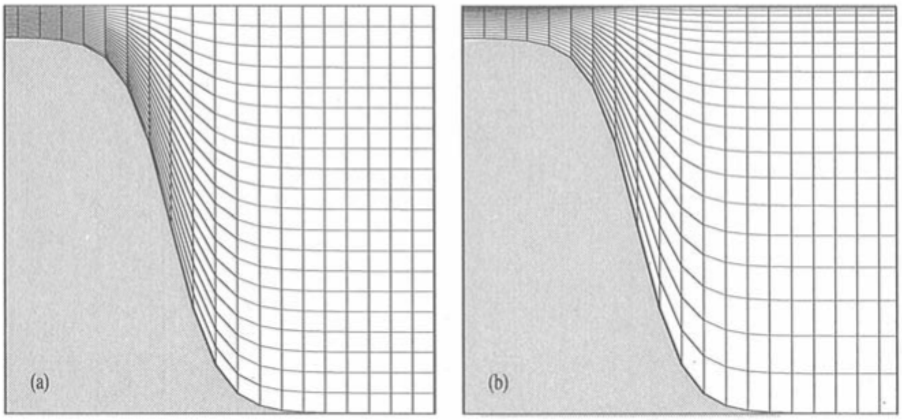

Figure 3.5: Example of the vertical structure of the terrain-following σ-coordinate. On the left part (a) an equidistant structure of the σ-coordinate can be seen and on the right part (b) a structure with an increased resolution near the surface is shown (Source: Haidvogel and Beckmann (1999))

3.2.4 Wet and dry treatment

Another important part of the FVCOM model is the wet and dry treatment. Especially in tidal flat areas that can be found in the East-Frisian Wadden Sea, a reliable method to estimate the status of a model cell must be found. In FVCOM the wet/dry point treatment method is used. In this method a static coastline as a boundary between land mass and water is defined, also defining the model domain and the numerical grid consists of wet and dry points. Nodes with a water depth of $D = h\,(x, y) + \eta\,(x, y, t) > h_c$ are defined as wet and points with a smaller depth are dry. The layer with the thickness h_c is called viscous boundary layer. The value for h_c should be sufficiently small to guarantee a motionless condition and mass conservation. In FVCOM this layer thickness is a minimum depth that is specified in an input-file that was chosen to be 0.05 m, plus a fixed value of $1 \cdot 10^{-5}$ m which is implemented in the source code. This fixed value guarantees that the depth is always higher than the minimum depth. To determine if a triangle is wet or dry the maximum surface elevation and the minimum depth of the surrounding nodes are used. If all nodes around a triangle are dry, the triangle is also treated as a dry triangle. Dry triangles are not taken into account for the flux calculation in the TCE or MCE to ensure the volume conservation. The wet and dry treatment is also connected to the values of I_{split} in equation 3.3, but the chosen value of 5 is sufficiently small.

3.2.5 Boundary treatment and external forcing

The treatment of triangles adjacent to a boundary is another important point in FVCOM. The flux in triangles next to a solid wall is calculated using the same method as for trian-

gles inside the grid and then the component normal to the wall is set to zero. Exceptions are triangles with a river inflow, but rivers were not taken into account in this thesis. For regions with a rapidly changing coastline a ghost cell treatment can be activated, but this was not done here, because some stability issues occurred while using this method.
There are several different types of external forcing that can be applied to the model. At the open boundaries a predetermined surface elevation provided by a global tide model or generated by tidal constituents (e.g. M_2) may be applied or various types of radiation open boundary conditions can be chosen. In this thesis a predetermined surface elevation was defined at every node of the open boundary. The wind forcing was also taken from a global model. Other types of external forcing like heat flux, precipitation, evaporation and groundwater input through the bottom were not taken into account.

3.2.6 FVCOM-SWAVE

The 2D third-generation structured-grid surface wave model SWAN (see Booij et al. 1999) has been added to the original source code of FVCOM as an unstructured-grid finite-volume version named FVCOM-SWAVE (see Qi et al. 2009) for the use in coastal ocean regions with a complex irregular geometry. The resultant modelling system can be applied to investigate e.g. the influence of wave energy generated by wind on the coast and the wave-induced currents. The surface wave model solves the action balance equation

$$\frac{\partial N}{\partial t} + \nabla \cdot [(\vec{c_g} + \vec{u})\, N] + \frac{\partial c_\sigma N}{\partial \sigma} + \frac{\partial c_\Theta N}{\partial \Theta} = \frac{S_{tot}}{\sigma} \tag{3.5}$$

that has already been described in section 2.2.4. The current velocity is added to the equation and also the frequency σ is influenced by the current as it has been mentioned in section 2.2.1. The surface wave model calculates the values for the wave-induced radiation stress which are delivered to the hydrodynamic model by coupling the governing equations (see section 2.4). The methods to calculate the energy source term S_{tot} have been described in chapter 2.2.
The equations utilised in FVCOM-SWAVE are solved using the Flux-Corrected Transport (FCT) algorithm in frequency space, the implicit Crank-Nicolson method in directional space and options of explicit and implicit second-order upwind finite-volume schemes in geographic space (see Qi et al. 2009).
The accuracy of the wave model depends on the resolution in frequency- and directional-space while the time step of the surface wave model is usually higher than the time step of the hydrodynamic model. The forcing of the model can be provided by global wave models or constant values generating a spectrum, for example a JONSWAP spectrum (see Holthuijsen 2007) can be chosen.
It should also be mentioned that SWAN itself can also be utilised as an unstructured-grid

model.

3.2.7 The code parallelisation

FVCOM has been parallelised using a Single Processor Multiple Data (SPMD) approach. The domain used for the calculations is decomposed using the METIS graph partitioning libraries and the interprocessor communication is explicitly defined utilising Message Passing Interface (MPI) calls. This enables FVCOM to be used on several different supercomputing architectures. Four different steps are carried out during a parallel computation. At first, the computation grid is decomposed into N subdomains with a more or less equal number of nodes and elements where N is the number of the processors. In every subdomain the responsible processor executes the FVCOM integration and during this calculation information between the boundaries is exchanged using halo nodes. At the end of this process the data is collected from every individual processor and the global array of the data is reconstructed and stored.
During the preparation of this thesis the computations were performed on the cluster of the North-German Supercomputing Alliance (Norddeutscher Verbund zur Förderung des Hoch- und Höchstleistungsrechnens - HLRN) and the cluster HERO (High-End Computing Resource Oldenburg), funded by the Deutsche Forschungsgemeinschaft (DFG) and the Ministry of Science and Culture (MWK) of the State of Lower Saxony, Germany. A short investigation of the benefit of a parallel computation has been carried out at the beginning of the work with FVCOM. A preliminary Wadden Sea setup with two and five simulated days was executed on different numbers of processors on the HLRN cluster and then the gain of speedup by using a higher number of processors was calculated by Dr. Karsten Lettmann (see figure 3.6). The result shows that on this architecture a positive gain of speedup can be reached until 400 processors are used. After that, the process of the exchange of information of data takes too much time and prevents a further gain in speedup. After coupling the surface wave model FVCOM-SWAVE to the hydrodynamic model FVCOM the ratio of the speedup to the number of involved processors decreased which might be caused by the implementation and parallelisation of the wave model. Cowles (2008) described the parallelisation procedure used in FVCOM and found that the implementation scales well on medium-sized clusters (around 256 processors) which is in agreement with the results presented here.

3.2.8 Overview of all modules and parts of FVCOM

In figure 3.7 the different parts of FVCOM are shown. The central part of FVCOM is the main code where the governing equations are solved. Before this is possible external forcings have to be defined and provided to the model. The output of the model is

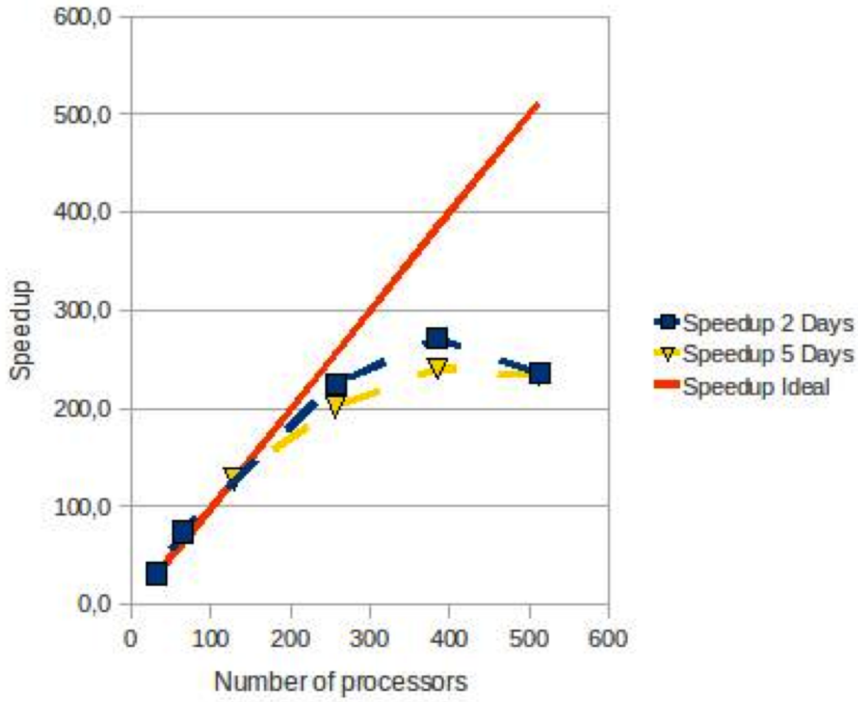

Figure 3.6: The speedup of a model run of a preliminary Wadden Sea setup. The model runs were performed by Sebastian Grashorn on the HLRN supercomputing cluster and the picture was created by Dr. Karsten Lettmann (ICBM, University of Oldenburg)

stored in a NETCDF-format and then processed by visualising tools. Most of this tools were written in the scientific progamming language MATLAB and the resulting toolbox is maintained and continuously extended by Dr. Karsten Lettmann and the work group "Physical Oceanography (Theory)" at the University of Oldenburg supervised by Prof. Dr. Jörg-Olaf Wolff. The modules that were used during the preparation of this thesis are the 3D Wet/Dry Treatment and the Surface Wave Model. Another interesting module for coastal investigations is the 3D Sediment Model that is based on the Community Model for Coastal Sediment Transport developed by the USGS and other researchers.

3.3 Publications with FVCOM

There are several papers that were published by the work group of Prof. Dr. Changsheng Chen, but also by other researchers using the ocean model FVCOM (see e.g. Justic and Wang 2009, Xing et al. 2012). In this section the key publications related to FVCOM and their outcome shall be reported.

One of the first papers and often cited as a reference is the publication by Chen et al. (2003). Here, the governing equations, the utilised turbulence scheme and other aspects of

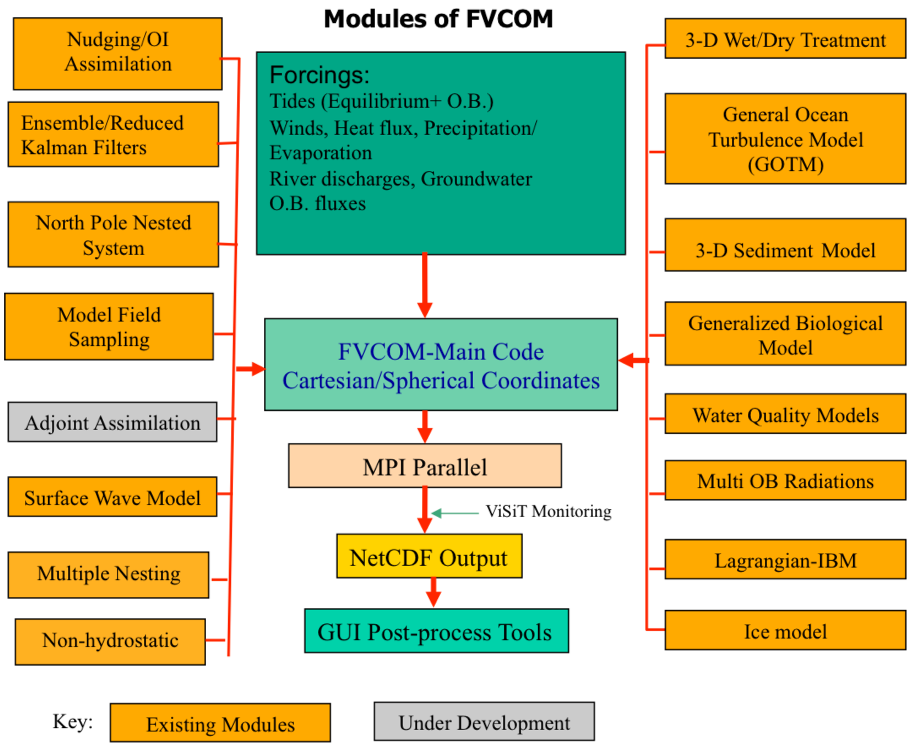

Figure 3.7: The structure of the ocean modelling tool FVCOM (Source: Chen (2013))

the model structure were explained. Some first model results were presented as well as a comparison to the semi-implicit Estuarine and Coastal Model (ECOM-si) (see Blumberg 1994) with different results around complex topographies.
In Chen et al. (2007) the three ocean models FVCOM, POM (see Blumberg and Mellor 1987) and ECOM-si were compared to each other. After running several test cases with all models the authors concluded that the finite volume method used in FVCOM provides a more accurate simulation than the two finite difference models in cases with complex coastal geometry and steep bottom slopes. The volume, mass and tracer conservation was ensured and the unstructured triangular grid fit to irregular coastlines very closely. This lead to accurate numerical solutions even in areas with a complex model geometry.
Qi et al. (2009) introduced in their publication the unstructured-grid surface wave model FVCOM-SWAVE. This model was also developed by the FVCOM staff. To proof the performance of the wave model they carried out four test cases dealing with numerical diffusion, wave-current interactions, wave shoaling and refraction and growth curves for wind-generated waves. As a realistic scenario an application to the Gulf of Maine has been created and the calculated data was compared to different buoys and measuring stations. The authors concluded that FVCOM-SWAVE provides an alternative version of a wave model based on an unstructured-grid finite-volume approach compared to the surface wave model SWAN. The test cases demonstrated that FVCOM-SWAVE has the

same accuracy as SWAN and the application to the Gulf of Maine suggests that FVCOM-SWAVE is robust and can capture the temporal and spatial variation of waves generated by different high-wind events over both continental shelf and near-shore regions.
In the publication by Wu et al. (2011) the capabilities of the two-way coupling of FVCOM and FVCOM-SWAVE were shown and the results of an additional coupled sediment model called FVCOM-SED were compared to the results produced with the structured-grid model ROMS. The authors also investigated the different current speeds generated by a model run with and without the coupled wave model. They found that the results agreed well with analytical solutions and laboratory experiments. The bed thickness patterns were similar to the results computed with ROMS.
Following these publications FVCOM seems to be a promising ocean modelling tool and it complies with the requirements to deal with the complex structures found in the East-Frisian Wadden Sea and around the Moorea island. These are the reasons why it was chosen for the investigations carried out during the preparation of this thesis.

3.4 Generating a model setup

In this section the process of generating a FVCOM model setup shall be explained. For this purpose again a MATLAB toolbox was developed by the work group and is maintained and continuously extended by Dr. Karsten Lettmann.
After choosing an area of interest the coastline of the model domain has to be provided either by downloading it from an internet source or extracting it from e.g. a nautical chart. Then, the bathymetry data has to be collected using the same sources or observational data. This bathymetric dataset can then be used to define rules for the creation of the unstructured grid. Since FVCOM does not include a grid generating system, a freely available finite element mesh generator called GMSH has been utilised (see Geuzaine and Remacle 2009). In the input-file of this tool a parabolic function is defined using the bathymetry data to calculate small grid sizes for a certain value of the depth and coarse sizes for depths not close to this value. Combining several rules results in the generation of a grid that can bee seen in figure 3.8. The figure shows that a coarse resolution of the grid was chosen for outer domains and a high resolution in the area of the East-Frisian Wadden Sea. Very often the grid has to be corrected using the following empirical quality criteria given by Chen et al. (2006a) to increase the stability of the model run:

1. The minimum interior angle must be greater than 30 degrees.
2. The maximum interior angle must be less than 130 degrees.
3. The area change of adjacent triangles must be less than a factor of 2.

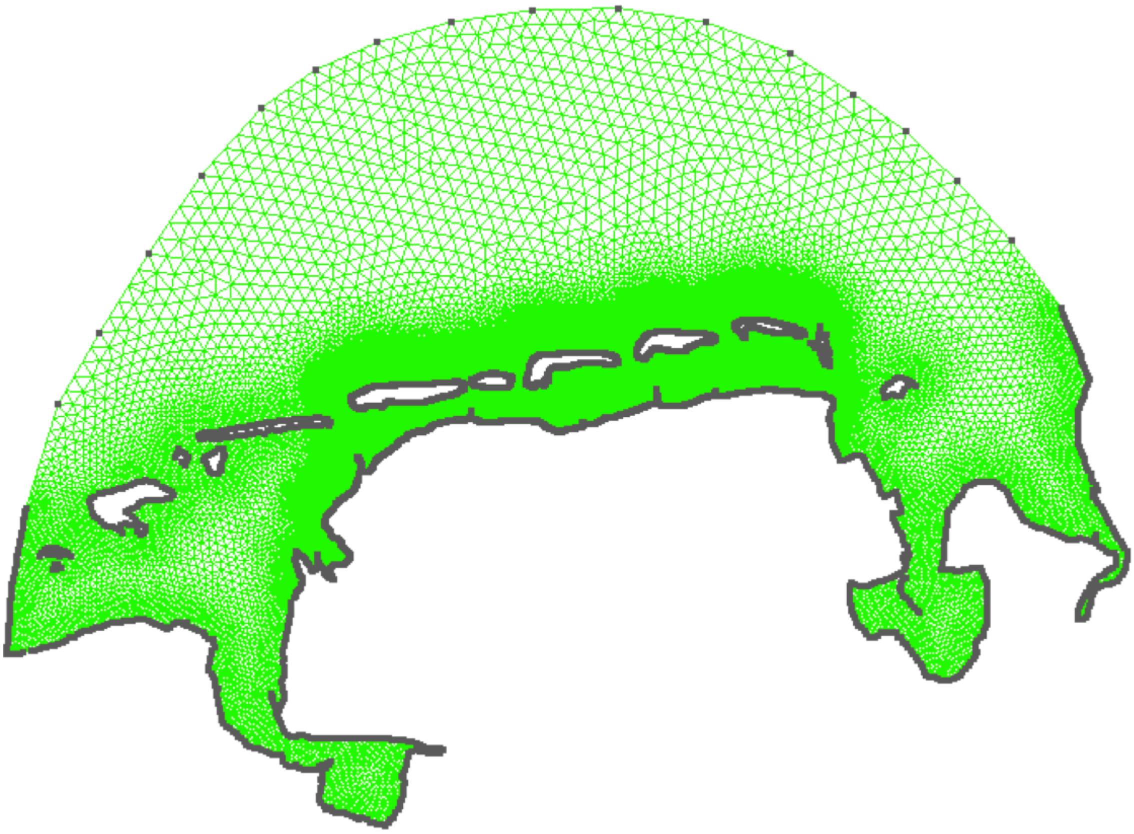

Figure 3.8: Resulting grid for the Wadden Sea area

Another aspect that should be paid attention to is the ratio between the grid resolution close to the coast and the resolution of the coastline itself since every point of the coastline will be a point of a triangle in the grid. If the ratio differs too much from being 1, the triangles will not fit into the coastline anymore and the grid will consist of stretched triangles in this area.

The next step is to interpolate the bathymetry data to the nodes of the generated grid. After this the bathymetry data can be smoothed. For example some criteria for the smoothing process proposed by Haidvogel and Beckmann (1999) for σ-coordinates can be used.

In the next step the input-files for FVCOM are created and provided to the model. One file describes the architecture of the grid and another one includes the bathymetry data. A sponge layer file can be defined to damp the surface elevation at the boundary of the model to increase the stability of the model. Two other files contain information about the locations of the boundary points and the location on Earth to calculate the Coriolis force. The most important file contains information on the physics, the time step, the start and end time of the run and other required model specifications (see chapter 7). There are extra input-files for the sediment or the surface wave model. Some forcing files may also be provided to the model. If the model run stops before the desired end time was reached because the offered wall time of a supercomputing cluster is exceeded, a so-called hotstart of the model can be performed, continuing the model run from the last time step of the previous run. In this case the hotstart-file must be provided to the model. The file that executes the model run is compiled from the source code of FVCOM. Before compiling the user has to decide which parts of the source code should be merged to form the execution file. If for example no wave module is needed, this option can be turned off. Having created all these files the model is ready for execution.

3.5 Changes in the source code of FVCOM

As already mentioned before FVCOM uses the MY-2.5 model turbulence closure model to calculate coefficients for the vertical eddy viscosity and thermal diffusion. In the tradi-

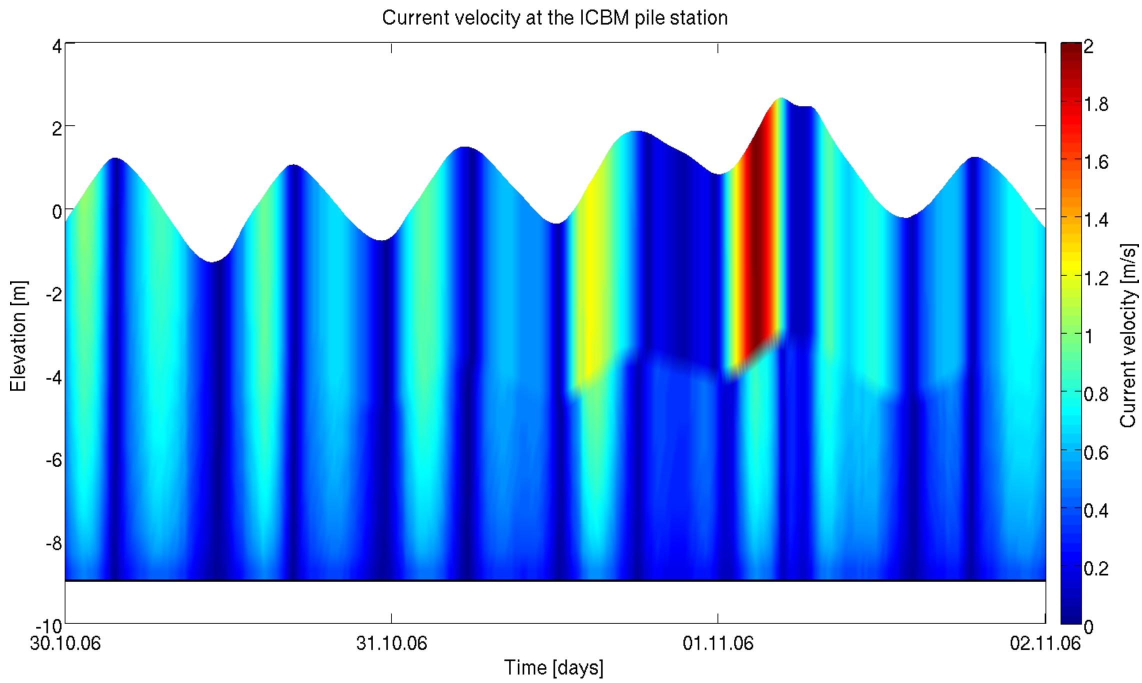

Figure 3.9: Unrealistic vertical distribution of the current velocity

tional MY-2.5 model these coefficients are zero at the lateral boundaries and at the surface and the bottom of the model (see section 2.1.4). For situations in the ocean with high waves this seems to be an unrealistic assumption since the surface waves will introduce some additional mixing into the water column. In FVCOM an effort was made to add this effect by implementing a parametrisation suggested by Mellor and Blumberg (2004), though the developers restricted this parametrisation on the upper half of the water column. This parametrisation does not affect the current velocity during moderate wind and wave conditions, but during storm conditions it has a negative effect on the model results. In figure 3.9 the vertical distribution of the current velocity at the pile station position between two barrier islands in the East Frisian Wadden Sea during a storm event in 2006 is shown (see also chapter 4). For this event it can be seen that the current velocity is very high in the upper half of the water column and an unphysical shear of the velocity is generated. This effect is not obvious in the depth-averaged velocities. The reason for the high velocities in the upper half of the water column is an overestimated turbulent eddy

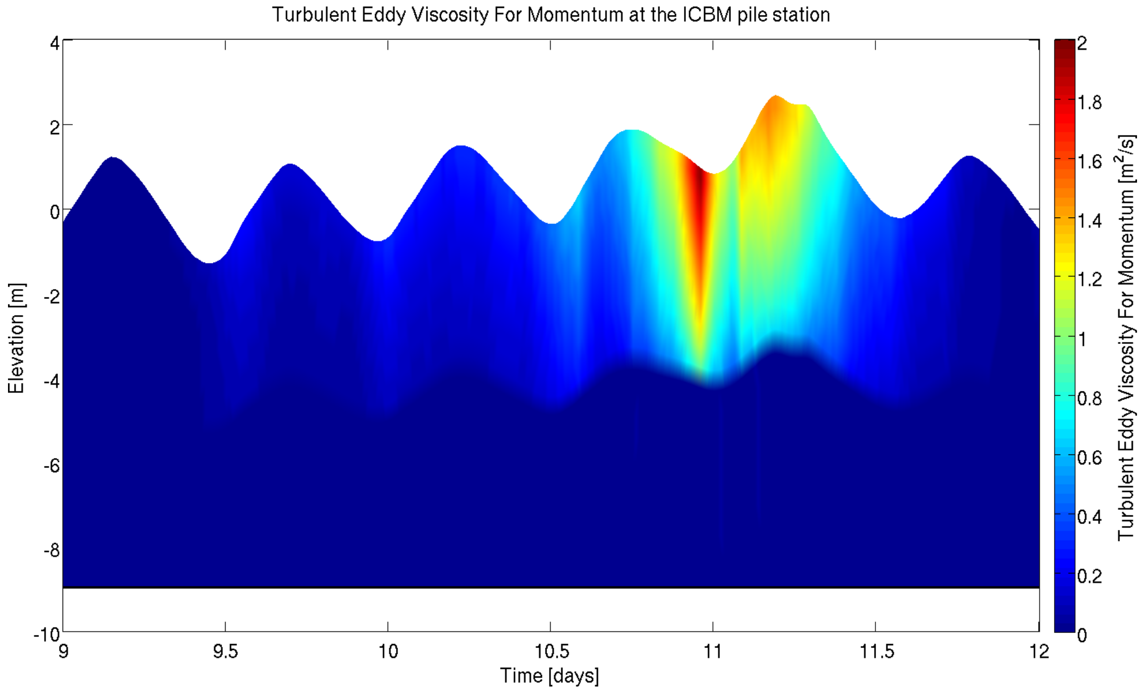

Figure 3.10: Unrealistic vertical distribution of the turbulent eddy viscosity

viscosity in the upper half of the water column (see figure 3.10). This parametrisation might work under conditions where the influence of the wave mixing does not reach depths lower than half of the water column, but for extreme events this approach fails. If the parametrisation is extended over the whole water column the current velocities are too low and reducing it to the surface layer will generate very high current velocities there and produce an unstable model run. Therefore, the parametrisation was deleted from the original source code and after this reasonable results that compare well with observations were produced by the model (see again chapter 4).

4 Part I: North Sea and East-Frisian Wadden Sea

In this chapter the influence of wave-current interactions in the area of the East-Frisian Wadden Sea islands is investigated. In section 4.1 some reasons to motivate this investigation are presented. The dynamics of the area of interest are analysed in section 4.2 and the model setups used for the investigation are explained in section 4.3. The performance of these model setups is tested in section 4.4. In the sections 4.5, 4.6 and 4.7 the models are used as tools to estimate the wave energy flux and the effects caused by the radiation stress. The outcome of this chapter is discussed in section 4.8.

4.1 Motivation

The barrier island system of the Dutch and German Wadden Sea located in the southern North Sea including various tidal inlets has been subject to many studies focusing on different features of this unique coastal system. Dastgheib et al. (2008), Dissanayake et al. (2009), van der Wegen et al. (2010) and Yu et al. (2012) used models to investigate aspects of the long-term morphological evolution of tidal inlet areas. In the East-Frisian Wadden Sea Stanev et al. (2003a,b, 2007a, 2008) and Staneva et al. (2009) used numerical modelling tools and observed data to describe different physical aspects of the hydrodynamics in this area. Stanev et al. (2006, 2007b) investigated driving factors of sediment dynamics and Lettmann et al. (2009) focused on the dynamical response of sediment dynamics for different scenarios including storm conditions using numerical modelling. Reuter et al. (2009) and Bartholomä et al. (2009) used measurements to investigate similar aspects. Most of these publications come to the conclusion that the East-Frisian Wadden Sea inlets are ebb-dominated (see e.g. Stanev et al. 2003a). Stanev et al. (2003a) also analysed the water transport and turbulence patterns inside this area to account for the possibility of a net sediment export/import. Sediment and bedload dynamics in coastal regions and especially in tidal flat systems are strongly coupled to water dynamics. Following Stanev et al. (2007b) four main factors of forcing influence the sediment and bedload transport in the coastal area: astronomical (tides), atmospheric (wind and wave climate), open ocean (mean sea level, curents and thermohaline fields) and coastal (fresh water flux). In

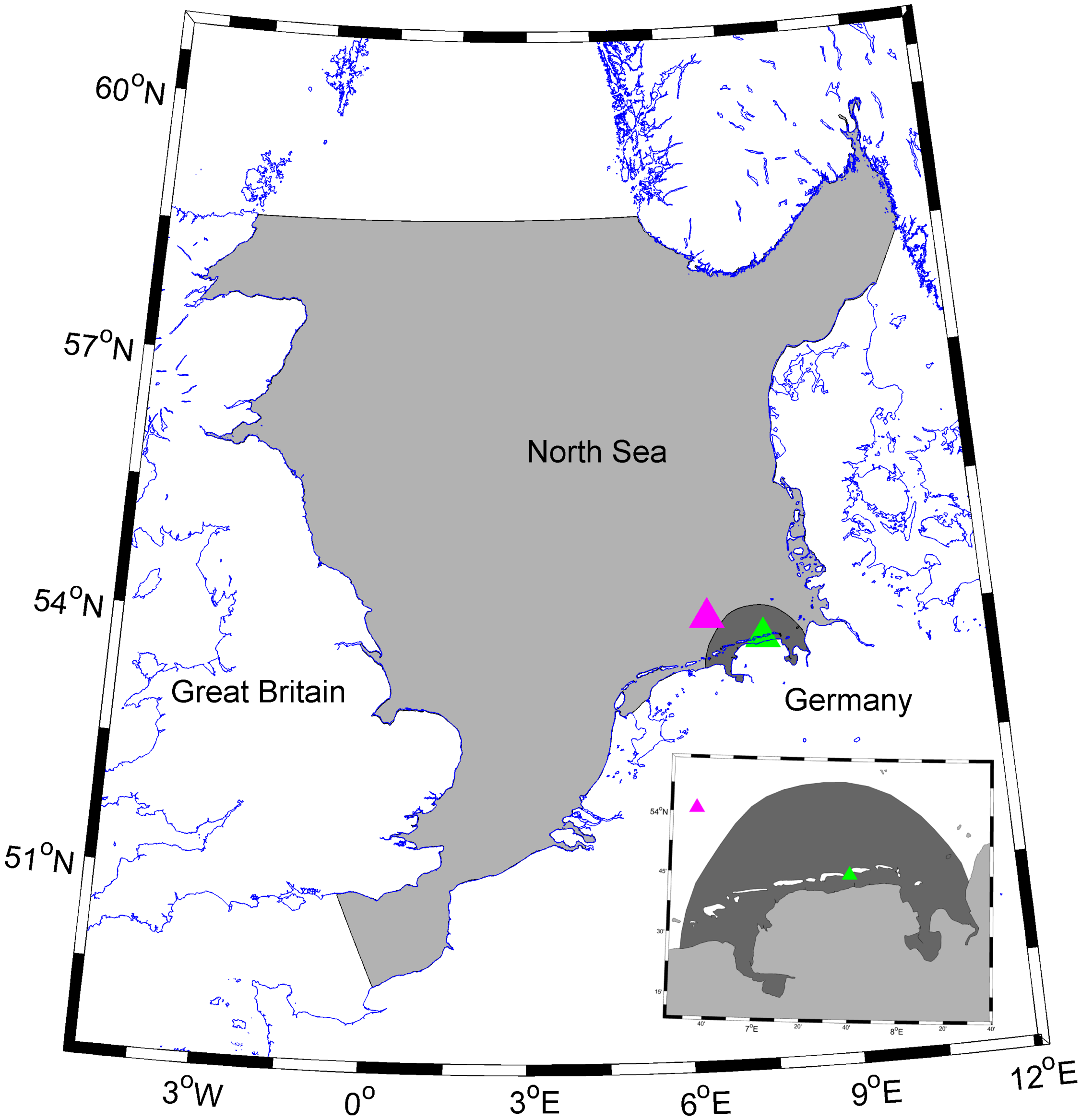

Figure 4.1: Area of interest including the North Sea and the German Bight. The two gray shaded areas depict the coverage of the North Sea and the high-resolution Wadden Sea model. A zoom into the area of the East-Frisian Wadden Sea can be seen in the lower right corner of the picture. The magenta-coloured triangle shows the position of the FINO I pile station and the green triangle shows the position of the ICBM pile station.

the East Frisian Wadden Sea the impact of waves on the sediment dynamics has been investigated by Stanev et al. (2007b). They concluded that high waves may influence the sediment budget in the area of the tidal flats behind the barrier islands. Bartholomä et al. (2009) investigated measurements in the area of an inlet between two barrier islands of the East-Frisian Wadden Sea and observed an export of material due to extreme events mainly controlled by the interference of wind/wave and tidal phase.

Another aspect that influences the sediment and bedload transport in this area is the generation of a longshore current by the interaction of waves and currents, especially in front of the barrier islands in the area of the East Frisian Wadden Sea. The model results published by Beach and Sternberg (1992) suggest that wave-current interactions enhance suspended sediment load and longshore sand transport by approximately 50-60% over the transport forced by waves alone. Different wind directions may produce different directions of the longshore current and thus influence the overall sediment and bedload transport in the Wadden Sea area. Therefore, the impact of wave energy generated by wind on the coast and the wave-generated currents in the area of the East-Frisian Wadden Sea have been investigated in this chapter.

The effects of wave-current interactions caused by radiation stress have been subject to several publications. Longuet-Higgins (1970) and Thornton and Guza (1986) derived equations for the magnitude of the longshore current. Pleskachevsky et al. (2009) investigated the impact of a storm surge on the North-Frisian island of Sylt by estimating the wave energy flux and the effects of wave-current interactions. Using a two-way-coupled modelling system they found that a wave-induced current of 1 m/s and a wave energy flux of about 160 kW/m can be estimated in their area of interest. Osuna and Monbaliu (2004) investigated various aspects of wave-current interactions with a focus on the Belgian coast.

An application of an unstructured-grid model that is two-way-coupled to a surface wave model with a high resolution of up to 50 m in the area of the chain of barrier islands in the East-Frisian Wadden Sea to investigate the wave-induced longshore currents and the energy flux along the coast has not been the focus of a study yet.

The unstructured-grid modelling system FVCOM coupled to the surface wave model FVCOM-SWAVE is applied to the North Sea and the chain of the barrier islands in the East-Frisian Wadden Sea using two setups with a high resolution in regions of high interest and with a reduced resolution towards the open North Sea. For an overview of other approaches to unstructured-grid modelling than FVCOM the author refers to Timmermann et al. (2009).

In order to test the sensitivity of the longshore current generated by wave-current interactions a North Sea model setup is used with different atmospheric forcing scenarios. In addition, data from the FINO I pile station has been analysed during the time period

2004-2013 to identify realistic atmospheric conditions.
This part of the thesis aims to (i) classify the wind climate in the area of the southern part of the German Bight and the hydrodynamics in the area of the East-Frisian Wadden Sea (see section 4.2); (ii) validate and compare the results given by a coarse North Sea model setup and a highly resolved Wadden Sea model setup (see section 4.3 and 4.4); (iii) calculate and discuss the wave energy input at the East-Frisian Wadden Sea coast for moderate and storm conditions (see section 4.5); (iv) test the sensitivity of longshore currents towards different wind directions in the area of the East-Frisian barrier island system (see section 4.6) and (v) calculate and discuss the effects of the wave-current interactions in the area of the East-Frisian Wadden Sea coast for moderate and storm conditions (see section 4.7).

4.2 Study site

The study site is located in the southern part of the North Sea including a W-E oriented chain of barrier islands and the northwestern coast of Germany (see figure 4.1). The area consists of several tidal flats and basins between the islands and the coast and the water exchange between the tidal flats and the deeper sea occurs via tidal channels. The tidal amplitude ranges from 1.5 m (spring tides) to 1.0 m (neap tides) (see Lettmann et al. 2009) and is characterised as a meso tidal zone (see Flemming and Bartholomä 1997, Stanev et al. 2003a). In the area of the tidal channels the current velocities can reach 1.5 m/s (see Santamarina Cuneo and Flemming 2000) and on the tidal flats they can reach 0.35 m/s (see Flemming and Delafontaine 1994). The energy flux in the tidal catchment is controlled by tidal currents, waves generated in the tidal basins and swells entering the inlet from the open North Sea and most of the energy transported by the swells is dissipated at the ebb delta and only 10 % of the energy is penetrating the inlet (see Krögel and Flemming 1998).
To investigate the wind climate in the area of the East Frisian Wadden Sea islands data collected in a height of 33 m at the FINO I pile station (provided by BSH, Federal Maritime and Hydrographic Agency of Germany) has been analysed. In figure 4.2 the dataset beginning at the 01.01.2004 and ending on the 31.12.2012 is plotted. There are several gaps in the data coming from missing wind speed and/or wind direction data. The data has been acquired at the station in a 10-minutes measuring interval. For further investigation the data has been hourly averaged. The overall mean wind speed and direction then are around 8.5 m/s and 200° (nautical convention, wind mainly coming from the wind direction south west), respectively.
In figure 4.3 the data was again averaged over every year, every month and every daytime. It can be seen that in 2008 the highest averaged wind speed can be observed and in 2010

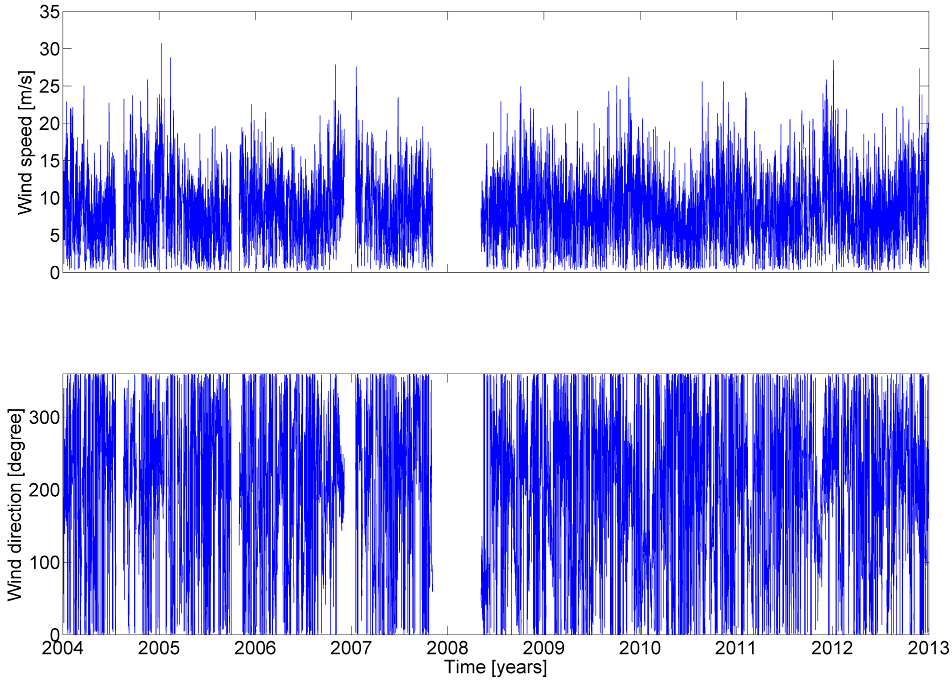

Figure 4.2: Measured wind speed and wind direction in a height of 33 m at the FINO I pile station.

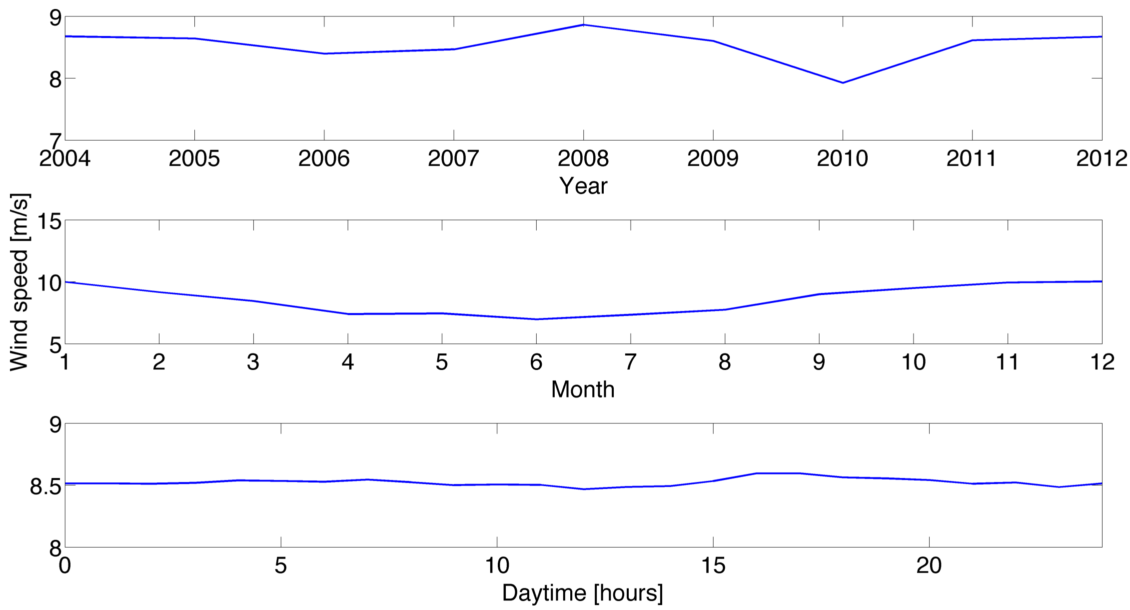

Figure 4.3: Yearly, monthly and hourly averaged wind speed data at the FINO I pile station.

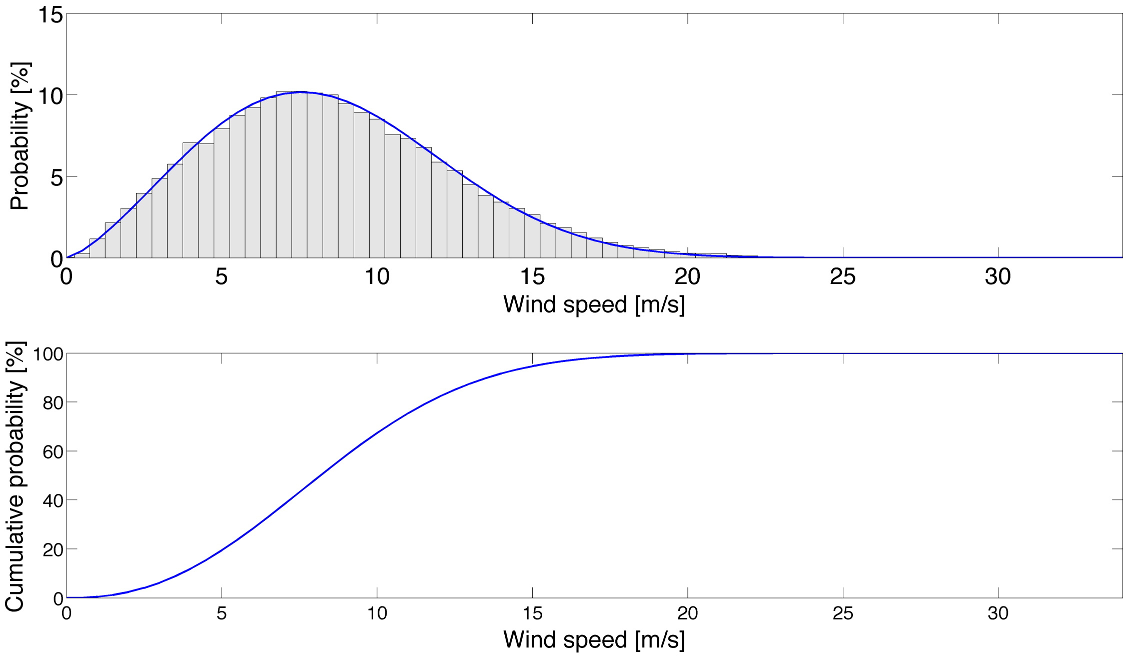

Figure 4.4: Probability (top panel) and cumulative probability density distribution (bottom panel) of the wind speed data at the FINO I pile station.

a minimum can be found. The range of the annual wind speed is between 8-9 m/s. The plot of the monthly averaged wind speed reveals the well known trend of high wind speeds in the winter months and reduced wind speeds in the summertime (see e.g. Coelingh et al. 1996). The diurnal plot of the averaged wind speed shows no significant trend and the wind speed is close to 8.5 m/s most of the time.

Figure 4.4 shows the probability and the cumulative probability density function of the wind speed data at the FINO I pile station. It can be seen that the wind speed data follows a Weibull distribution and that there is a maximum in the probability distribution around 7.5 m/s. The cumulative probability density function shows that around 90% of the wind speed data consists of values smaller than 15 m/s, indicating that storms with high wind speeds are really rare extreme events in this area.

The wind rose at the FINO I pile station shown in figure 4.5 reveals a clear dominance of north-eastern directed winds, but there are also significant occurrences of winds coming from the NW-, W- and E-direction.

Following these results it can be noted that there are remarkable occurrences of several wind directions and most of the time wind speeds are lower than 15 m/s. A seasonal dependance of the wind speed can be identified, but there is no trend in the yearly averaged data of the last decade.

In figure 4.6 the joint probability distribution of the wave data extracted from measurements of the wave buoy at the FINO I pile station beginning at the 01.01.2004 and ending

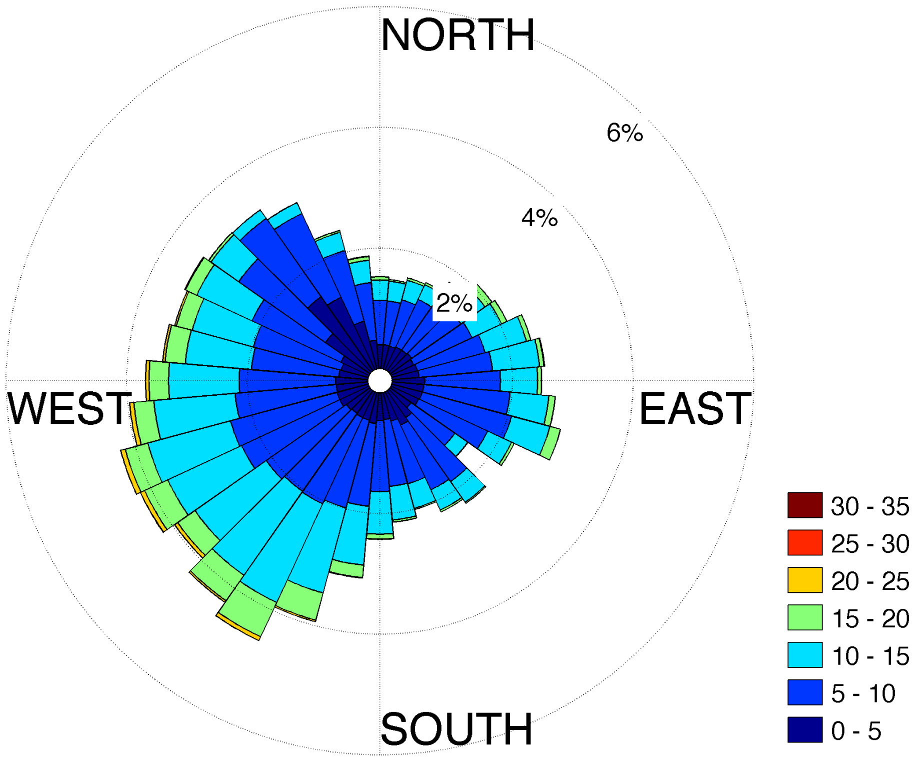

Figure 4.5: Wind rose of the wind speed data at the FINO I pile station in m/s.

at the 31.12.2012 can be seen. It can be noted that the significant wave height with the highest probability is around 1 m and the corresponding peak period and wave direction are around 5 s and 340°, respectively. This dominance of waves coming from the north-west might be a consequence of swells generated in the northern part of the North Sea and that the longest fetch follows a north-south direction. But there are also remarkable occurrences of waves coming from the east and south-west. The width of the bins of the FINO I data was chosen to be δH_{sig}=0.25 m for the significant wave height, δT_p=1 s for the peak period and δW_{dir}=15° for the wave direction. The total number of measurements is 100165.

4.3 Model setup

The digital topography of the East Frisian Wadden Sea is a combination of high-resolution data provided by the BSH and the NLWKN (Niedersächsischer Landesbetrieb für Wasserwirtschaft, Küsten- und Naturschutz). The topography data for the deeper North Sea were taken from the ETOPO2 (U.S. Department of Commerce, National Oceanic and Atmospheric Administration, National Geophysical Data Center, 2006. 2-minute Gridded Global Relief Data (ETOPO2v2)) data set (see Lettmann et al. 2009).
The coastline was extracted from the commercial software Cruising Navigator distributed

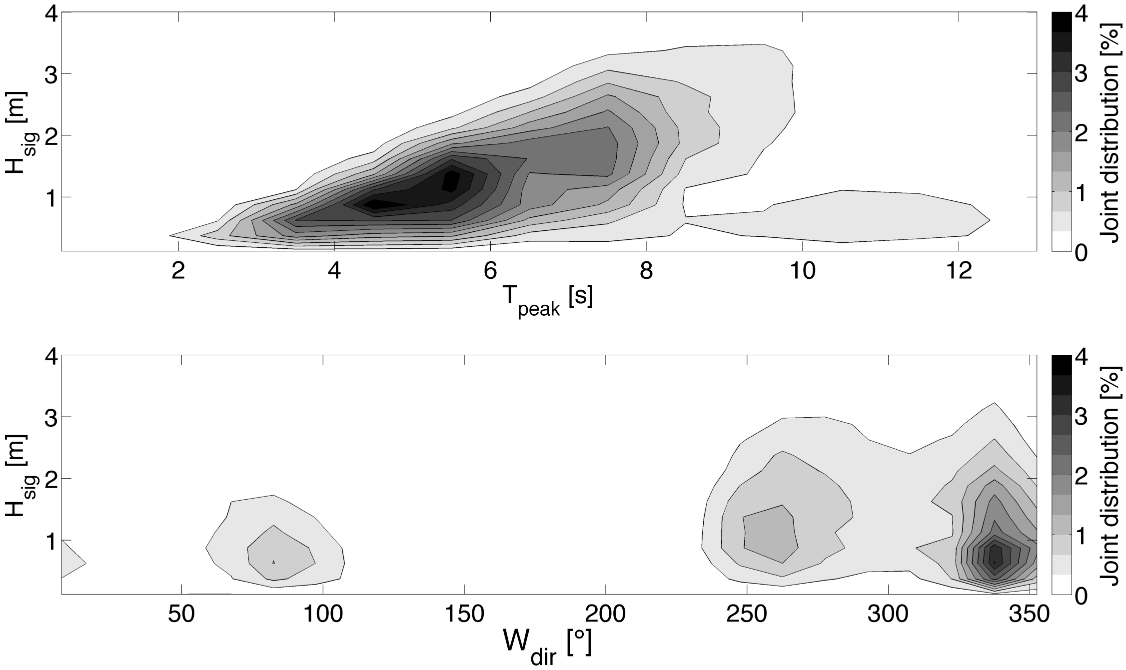

Figure 4.6: Joint probability distribution of the wave data at the FINO I pile station beginning at the 01.01.2004 and ending at the 31.12.2012. The width of the bins of the FINO I data was chosen to be δH_{sig}=0.25 m for the significant wave height, δT_p=1 s for the peak period and δW_{dir}=15° for the wave direction. The total number of measurements is 100165.

by Maptech Inc. and combined with the extracted coastline from the NOAA National Geophysical Data Center (WVS) (http://www.ngdc.noaa.gov/mgg/shorelines). The wind and pressure data that was used as the atmospheric forcing of the model, was provided by the atmospheric model COSMO-EU maintained by the DWD (German Weather Service) with a temporal resolution of 1h in 2006 and 2h in 2007. The spatial resolution is 7 km and 40 vertical layers. The boundary conditions for this local European model are delivered by the global atmospheric model GME.

Figure 4.7 shows a section of the grid that is used for the investigation of the wave-current interactions in the area of the East-Frisian Wadden Sea. The resolution of the coastline and inside the model area close to the area of interest is 120 m. It is reduced to 300 m and 500 m in an intermediate zone and finally to 2000 m in the region close to the boundary of the model. In the tidal channels the resolution is 50 m in order to resolve higher dynamics sufficiently (see figure 4.7). This grid is one-way coupled to the North Sea Model, that has also been generated with GMSH. This model has a resolution of 500 m in the area of the East-Frisian Wadden Sea and a reduced resolution of down to 6000 m in deeper areas. A vertical resolution of 20 σ-layers was chosen for both model setups. The Wadden Sea model consists of 163644 elements and 83239 nodes and the North Sea model consists of 220183 elements and 113314 nodes.

The modelling system FVCOM provides the opportunity to force the model at the open boundary using a predetermined surface elevation and/or wave conditions. For the surface elevation at the three open boundaries (see figure 4.1) of the North Sea model the output of the Global Tide model FES2004 (Finite Element Solution 2004) was used. FES2004 was produced by Legos and CLS Space Oceanography Division and distributed by Aviso, with support from CNES (http://www.aviso.oceanobs.com) (see Lyard et al. 2006). The surface elevation is affected by the inverse barometer effect, such that a change of 1 hPa will result in a change of 1 cm in surface elevation (see Kliem et al. 2006). This correction was applied to the FES2004 output data.
A southward-directed JONSWAP wave spectrum (see Holthuijsen 2007) with a significant wave height of 1 m and a peak period of 10 s is defined as a boundary condition in the FVCOM-SWAVE input-file for the North Sea setup.
The Wadden Sea model is one-way nested in the North Sea model, thus providing the surface elevation and wave conditions for the open boundary forcing of the highly resolved model. The peak period at the boundary had to be smoothed to guarantee a stable model run.
FVCOM-SWAVE was utilised in a non-stationary mode with a time step of 300 s for the North Sea model and a time step of 10 s for the Wadden Sea model. The default con-

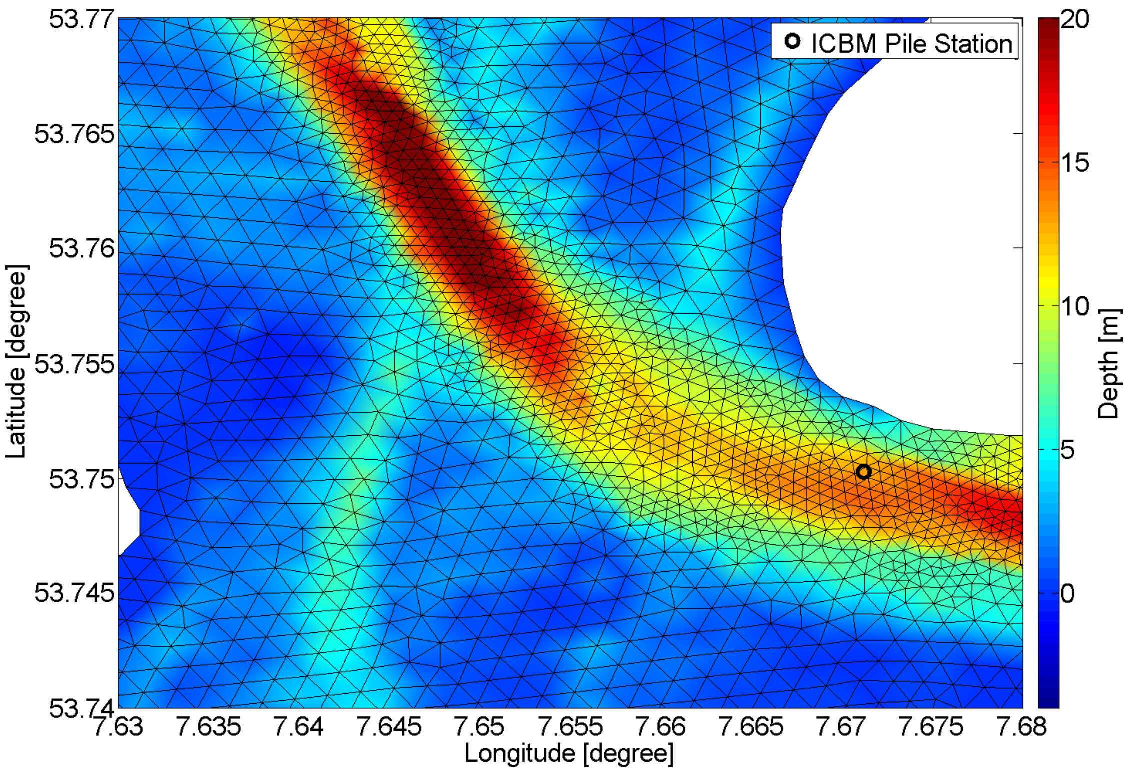

Figure 4.7: Tidal channel between the barrier islands Langeoog and Spiekeroog. The grid resolution is increased to 50 m here.

ditions for wave energy input and dissipation and for wave propagation were applied. In detail, the processes of wave growth, quadruplet wave interactions, white capping, wave breaking, bottom friction and triad wave interactions have been activated. The resolution of the frequency and the directional domain are 30 and 24 bins, respectively. The directional range is a full circle 360° and the frequency range is 0.04-0.4 Hz. The peak period had to be smoothed for the hotstart procedure.
For the hydrodynamic part of FVCOM a time step of 10 s for the North Sea model and a time step of 2 s for the Wadden Sea model were used. The salinity and the temperature were set to a constant value of 35 PSU and 10 °C, respectively. To use this approach might be justified by the fact that during the investigated period in autumn density gradients in the Wadden Sea show a seasonal minimum (see Wang et al. 2011). The default values for bottom friction and vertical and horizontal mixing were applied. A spin-up time of two days and one day were used for the North Sea model and the Wadden Sea model, respectively.
The computations were performed on the cluster of the North-German Supercomputing Alliance (Norddeutscher Verbund zur Förderung des Hoch- und Höchstleistungsrechnens - HLRN) and the cluster HERO (High-End Computing Resource Oldenburg), funded by the Deutsche Forschungsgemeinschaft (DFG) and the Ministry of Science and Culture (MWK) of the State of Lower Saxony, Germany. The number of the processors used for the computations was 32 and the integration time for one time step for both models was around 6 s.

4.4 Validation and comparison of the model results

For validation purposes of the model two time periods in 2006 and 2007 were analysed for the North Sea and the Wadden Sea model.
In figure 4.8 the calculated and measured significant wave height, peak period and wave direction and in figure 4.9 the surface elevation in Oct./Nov. 2006 and Nov. 2007 at the FINO I pile station and ICBM pile station (see figure 4.1) can be seen. The mean significant wave height in 2007 is around 3 m, but during a storm event in 2006 it can go up to more than 9 m. During the storm period, the model seems to reproduce the measured significant wave height, peak period and wave direction reasonably. It can also be seen that in 2006 and 2007 the main wave directions are N-NW (nautical convention) and the main peak period is about 7 s in 2007, but it can go up to 14 s during the storm event in 2006.
In 2007, the modelled results seem to reproduce the characteristics of the measured surface elevation well, but a phase shift in time of the sea level signal compared to observations is quite noticeable. In view of the theoretical results discussed here this forcing error has

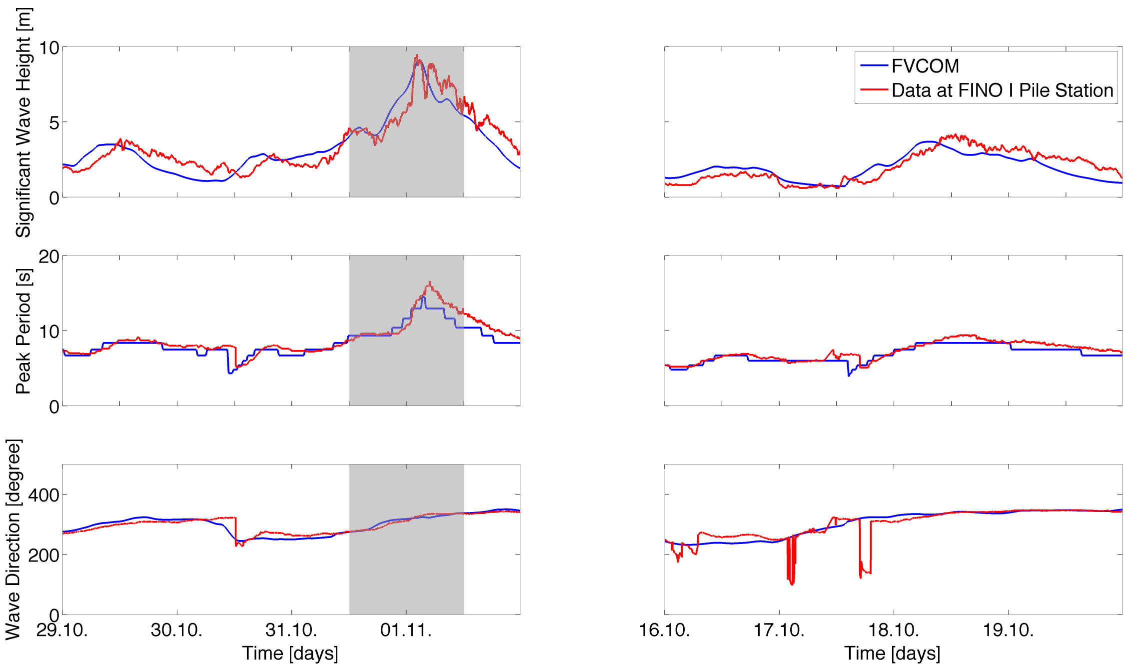

Figure 4.8: Measured and modelled significant wave height, peak period and wave direction at the FINO I pile station calculated with the North Sea setup. On the left hand the time period 29.10.06-02.11.06 including the storm surge Britta (grey colour) is shown. On the right hand the time period 16.10.07-20.10.07 is shown.

no direct consequences. In 2006, the peak of the surface elevation during the storm event is not reproduced by the model. The phase shift can be caused by the parametrisation of the bottom roughness. The drag coefficient could be too small or to high in some regions. In this setup the drag coefficient is constant over the whole model area. Additionally, the bathymetry data in the area of the open North Sea and at the coastline of other countries than Germany is very coarse. Some deeper channels close to the coastline might be missing in the dataset. The dataset has been interpolated on the nodes of the unstructured grid. This could also lead to errors in the bathymetry file that has been used for the model runs. The consequence could be an overestimated bottom roughness and a deceleration

Table 4.1: Calculated root-mean square errors for the two model setups and pile stations (FINO I pile station for the North Sea model and ICBM pile station for the Wadden Sea model)

	North Sea model		Wadden Sea model
	2006	2007	2006
$H_s [m]$	0.8370	0.6163	
T_p [s]	0.9917	0.6476	
W_{dir} [°]	13.0042	34.5072	
ζ [m]	0.2430	0.2721	0.4622

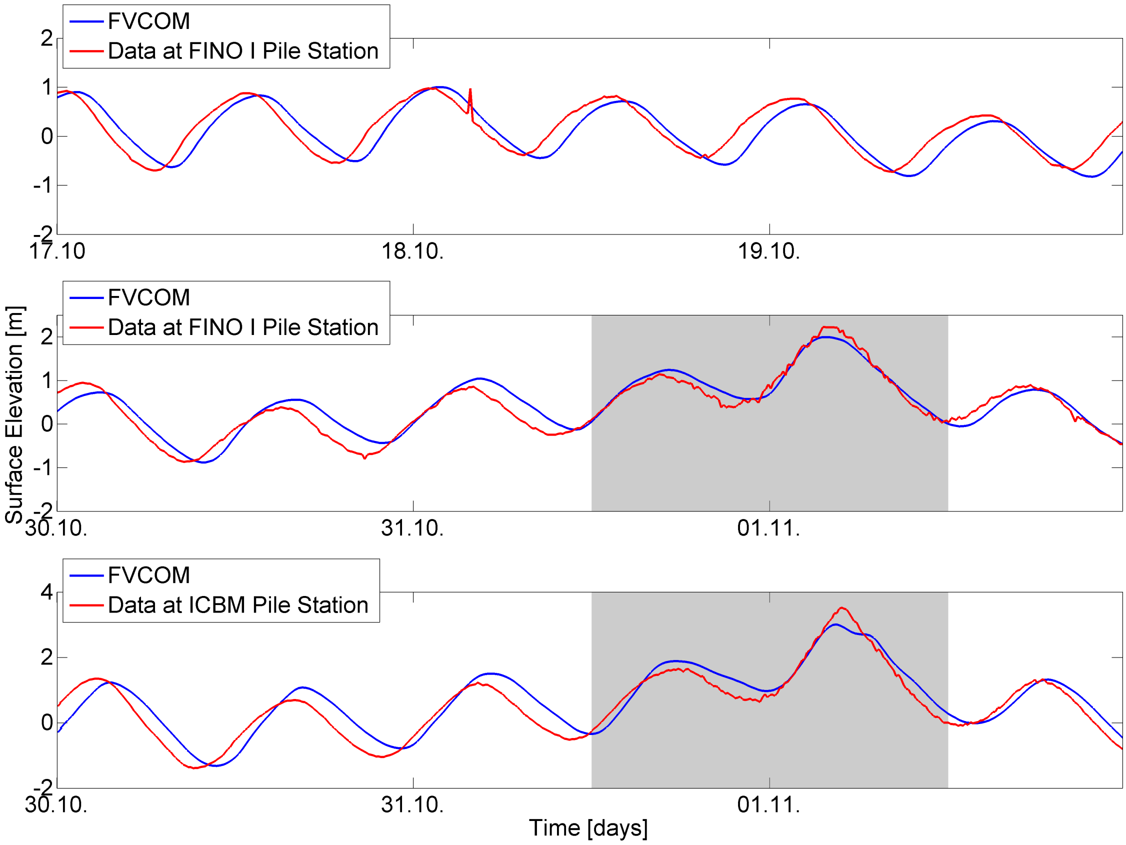

Figure 4.9: Measured and modelled surface elevation at the FINO I and ICBM pile station. The top plot depicts the surface elevation calculated with the North Sea setup at the FINO I pile station during the time period 17.10.07-20.10.07 and the middle plot shows the calculated surface elevation during the time period 30.10.06-02.11.06 including the storm surge Britta (grey colour). The bottom plot depicts the surface elevation during the storm Britta calculated with the Wadden Sea setup at the ICBM pile station.

of the tidal wave. During the storm event the water column increases and the effect of the bottom roughness on the surface elevation decreases. That is why the phase shift is reduced during the storm surge.

In figure 4.10 simulated velocities by the North Sea model are compared to measured data that was obtained during a ship cruise on a fixed position in October 2007. The model underestimates the velocities during the ebb phase and the process of the upcoming low tide takes longer than during the measurement. Again a phase shift in time has to be noticed.

A vertical distribution of the current velocity at the ICBM pile station (see figure 4.1) can be seen in figure 4.11. The North Sea model clearly underestimates the current velocity, but the Wadden Sea model shows reasonably results. However, both models can not reproduce short time fluctuations of the current velocity.

In table 4.1 the root-mean square errors for the different stations and variables are listed.

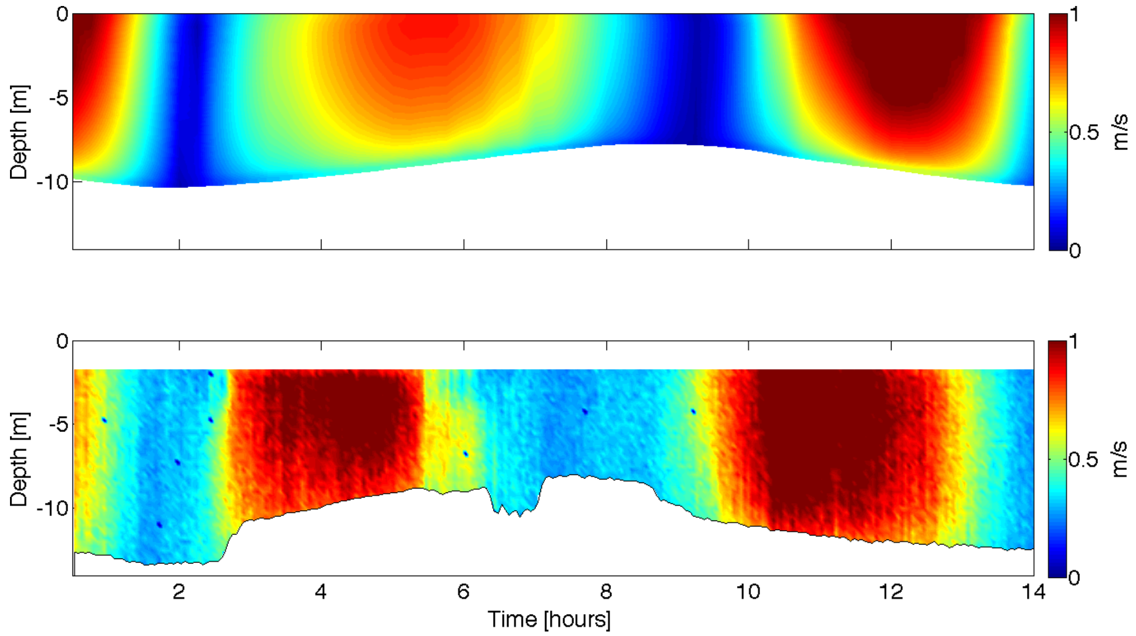

Figure 4.10: Measured and modelled current velocity of the North Sea model at a fixed position between two barrier islands. The measurements started at 17.10.07, 00:00:00 UTC.

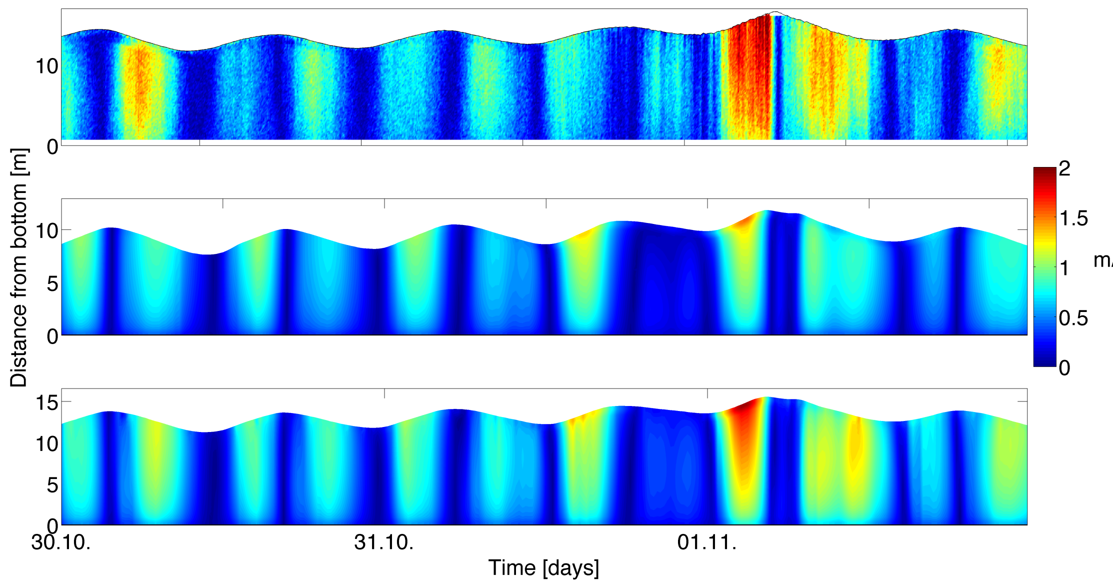

Figure 4.11: Measured and modelled current velocity at the ICBM pile station between two barrier islands between the 30.10.06 and 02.11.06. The top panel shows the measured data. In the middle panel the result of the North Sea model and in the bottom panel the result of the Wadden Sea model can be seen.

During the storm event the North Sea model performs better than in 2007 in relation to the maximum observed values. The Wadden Sea model reveals a high error for the surface elevation during the storm event. This is mainly caused by the phase shift and the underestimation of the peak of the surface elevation.

4.5 Wave energy flux

Energy is transported by a wave in the direction of propagation. In the region of the East Frisian Wadden Sea the chain of barrier islands acts like a natural protection of the north-western German coast and "absorbs" most of the energy. Here, the amount of wave energy or wave energy flux is calculated to estimate the impact on the barrier islands during a storm event and a time period with no significant storms using equation 2.86 (see section 2.2.3).
The resulting mean wave energy flux can be seen in figure 4.12 for the two different time periods in 2006 and 2007. In 2006, a mean wave energy of about 70 kW/m is approaching the coast. In 2007, less energy is transported by the waves, but in all three cases the barrier islands absorb most of the wave energy. The influence of the ebb-tidal delta in front of the inlet can also be identified.
Figure 4.13 shows the profile of the maximum daily mean and the mean of wave energy

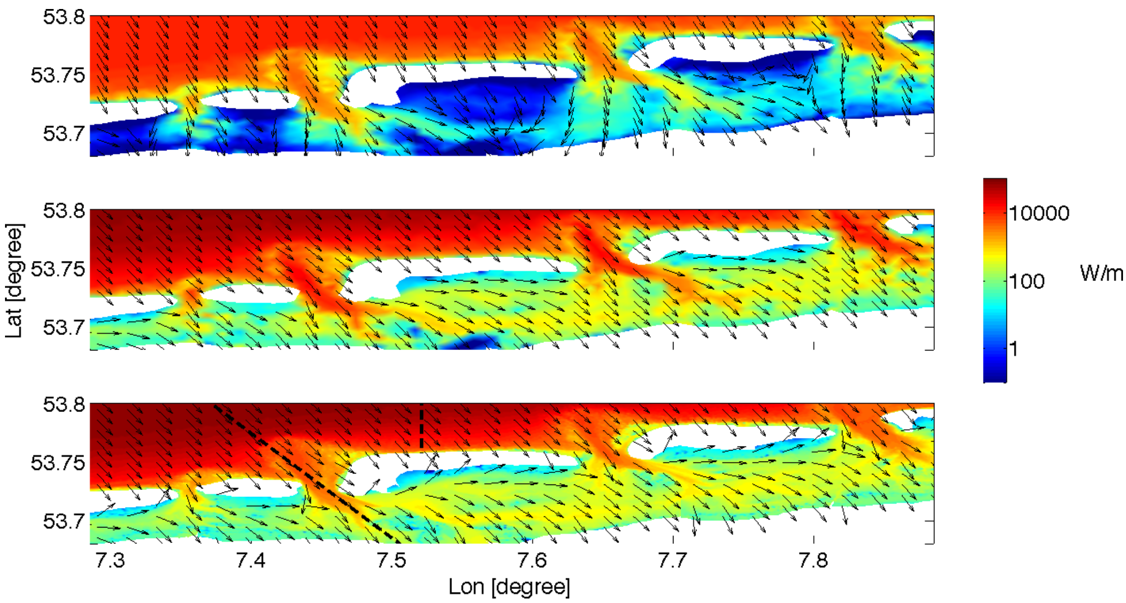

Figure 4.12: Modelled mean wave energy flux. The figure in the top position (North Sea model) shows the mean wave energy flux during the time period 16.10.07-20.10.07. The middle (North Sea model) and bottom (Wadden Sea model) figures depict the time period 30.10.06-02.11.06 including the storm surge Britta. The arrows have been interpolated onto an uniform grid and normalised to 1. The sections in the bottom panel are used to analyse the wave energy flux and the v-component of the longshore current in this chapter.

during the time period 30.10.06-02.11.06 interpolated on a section in front of the coast of a barrier island and along a tidal inlet (see figure 4.12). It can be seen that the maximum daily mean wave energy flux can reach up to 190 kW/m in front of the coast during the storm event, a similar result compared to the value of around 160 kW/m found by Pleskachevsky et al. (2009) for the island of Sylt. In front of the barrier island the wave energy flux shows a strong decrease starting at 4 km before reaching the barrier island

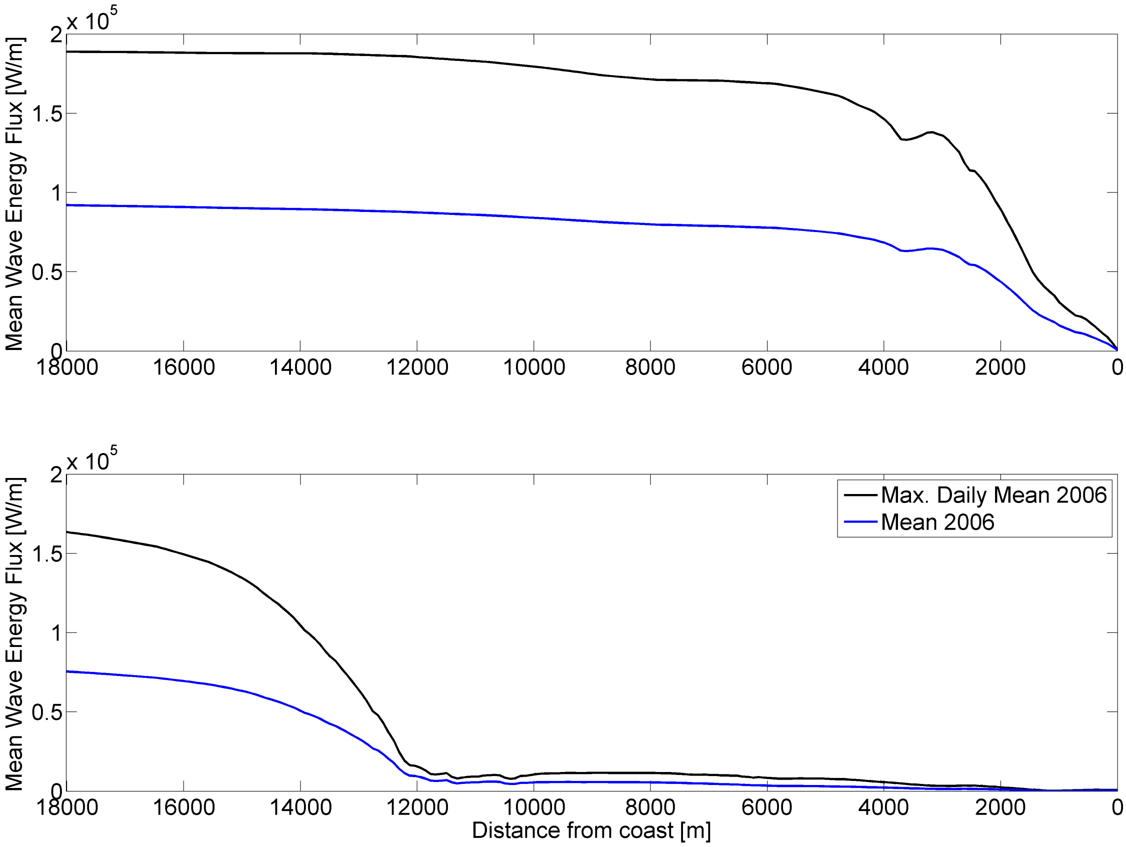

Figure 4.13: Profile of the mean wave energy flux calculated by the Wadden Sea model. The maximum of daily mean and the mean of wave energy flux during the time period 30.10.06-02.11.06 is shown. The upper plot depicts the section in front of the barrier island Langeoog. The plot at the bottom shows the wave energy flux along a tidal inlet. The position of the sections can be seen in the bottom panel of figure 4.12.

Langeoog. Along the tidal inlet it decreases at the area of the ebb-tidal delta rapidly to a value of less than 10 % of the high value in front of the barrier islands like it was mentioned by Krögel and Flemming (1998).

4.6 Sensitivity of the longshore current to the wind direction

The radiation stress can be described as a momentum transport by waves that acts as a horizontal stress (see section 2.3). The gradients in these (shear) stresses act as forces and generate currents. This effect is especially obvious inside the surf zone. Higher waves

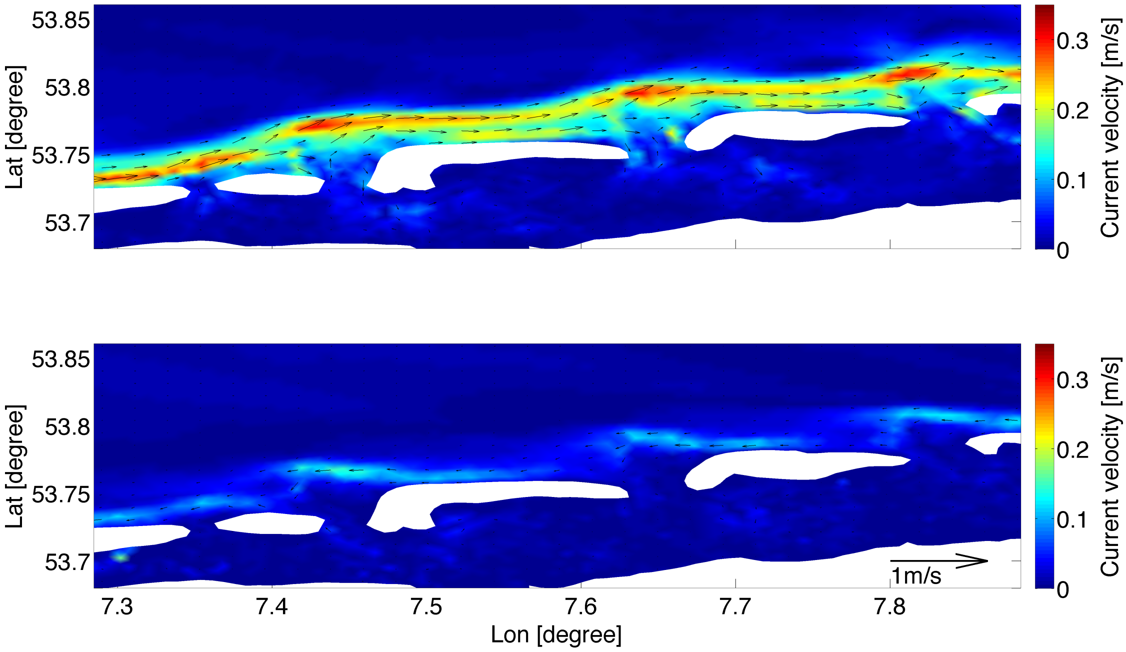

Figure 4.14: Modelled difference in current velocity due to current-wave interaction. The plot in the upper panel shows the longshore current generated by eastward directed winds and the plot in the lower panel depicts the current resulting from westward directed winds. The wind speed was constant at 15 m/s for four days. The current velocity is calculated from the difference of two model runs with and without the wave model coupled to the hydrodynamic model. The arrows have been interpolated onto an uniform grid.

will result in higher wave energy and thus generate higher radiation stress gradients. When approaching the coast this effect will contribute to increased current velocities in the coastal area. Especially during a storm event high waves occur and generate strong longshore currents (see Pleskachevsky et al. 2009).

In this section a sensitivity study of the longshore current to the wind direction is carried out. The four main wind directions in this area are winds coming from SW, W, NW and E, thus four scenarios with different wind directions were created (see section 4.2). For a spin-up time of two days a constant wind speed of 5 m/s was applied and no pressure influence was considered here. The surface elevation at the boundary was taken from the scenario in 2007 described in section 4.4. A four days model run with a wind speed of 15 m/s was then carried out and the results for the different wind directions can be seen in the figures 4.14 and 4.15. The wave-induced current velocity has been integrated over one tidal cycle and then the difference between a North Sea model run with and without the wave model coupled to the hydrodynamic model is calculated. It is shown that the strongest longshore currents are generated by eastward and south-eastward directed winds (Cartesian convention). The dominant north-eastward directed winds do not contribute to the longshore currents, but the westward directed winds are able to generate a longshore

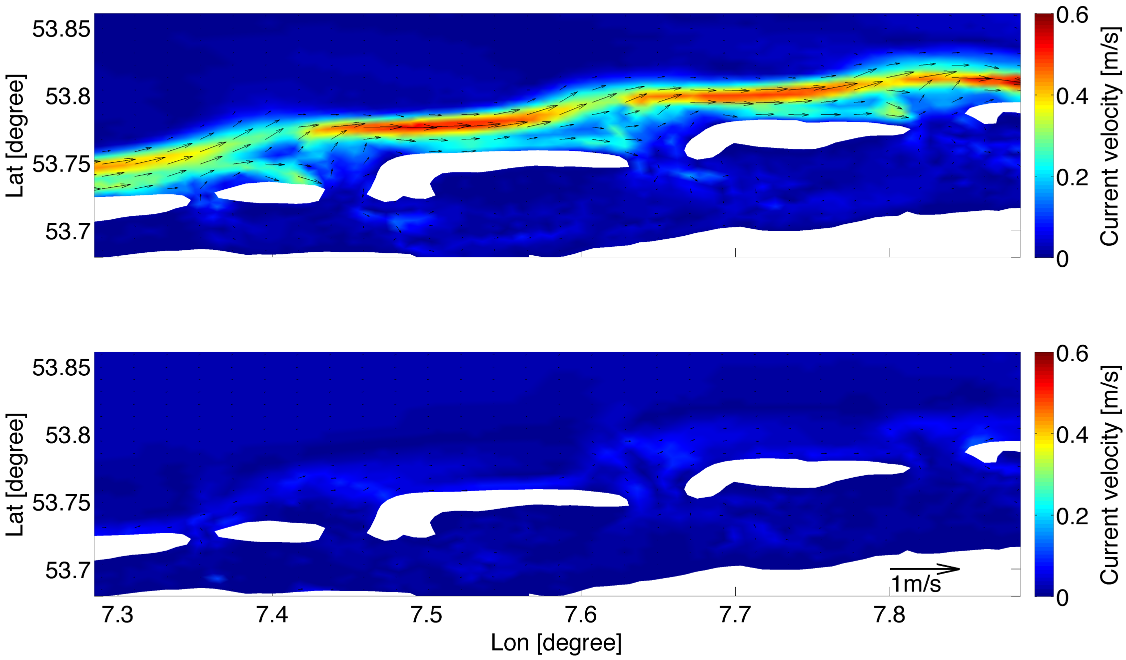

Figure 4.15: Modelled difference in current velocity due to current-wave interaction. The plot in the upper panel shows the longshore current generated by south-eastward directed winds and the plot in the lower panel depicts the current resulting from north-eastward directed winds. The wind speed was constant at 15 m/s for four days. The current velocity is calculated from the difference of two model runs with and without the wave model coupled to the hydrodynamic model. The arrows have been interpolated onto an uniform grid.

current in a westward direction. The magnitude of this current is much smaller than the eastward-directed longshore currents. This results from a smaller fetch which starts at the coastline close to Hamburg. However, this current also contributes to the transport of bedload and sediment that is generated by the currents. The dominant direction of the longshore currents is to the east.

4.7 Radiation stress effects on the hydrodynamics

The North Sea model setup and the Wadden Sea model setup of FVCOM were used to calculate the wave-generated velocities at the East-Frisian coast during a storm period and a moderate situation. The wave-induced current velocity is calculated from the difference between a model run with and without the wave model coupled to the hydrodynamic model. In figure 4.16 it can be seen that during the storm period in 2006 the strongest currents were generated with values up to around 0.7 m/s in the North Sea model and around 1.0 m/s in the Wadden Sea model. During 2007 no significant storm surges occurred and the highest longshore currents reached a maximum value of around 0.6 m/s. The current-wave interaction also influences the surface elevation in the East Frisian

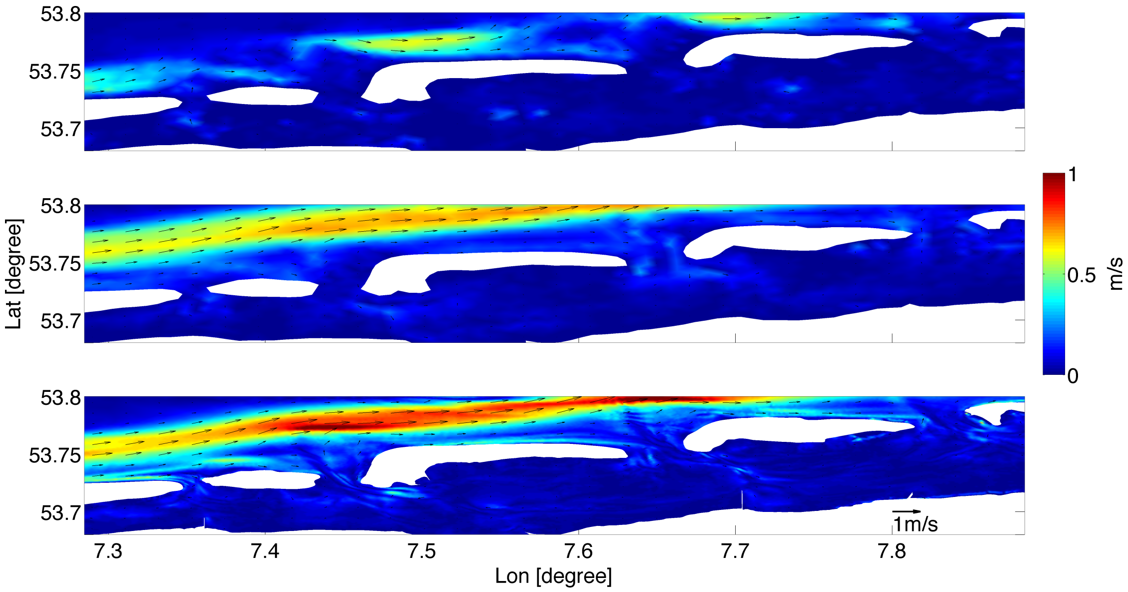

Figure 4.16: Modelled difference in current velocity due to current-wave interaction. The plot in the top position (North Sea model) shows the difference in current velocity at 18.10.2007, 08:00:00 UTC. The middle (North Sea model) and bottom (Wadden Sea model) plots depict the time point 01.11.06, 01:00:00 UTC during the storm surge Britta. The current velocity is calculated from the difference of two model runs with and without the wave model coupled to the hydrodynamic model. The arrows have been interpolated onto an uniform grid.

Wadden Sea area. Figure 4.17 shows the surface elevation during the storm surge Britta and the residual currents during the time period 31.10.06/01.11.06. The waves produce an increased surface elevation of around 0.15 m in most of the tidal flat area. The overall maximum residual current during the storm event is around 1 m/s. The increase of the surface elevation might be explained by an increased volume transport via the tidal inlets. In figure 4.18 the difference in the volume transport between a model run with and without the wave model coupled to the hydrodynamic model through the inlet between Langeoog and Spiekeroog during the 31.10.2006 can be seen. During the storm event the transport directed into the back barrier Wadden Sea is enhanced and thus more water enters this area and increases the mean water level.

Because no validation data for the longshore currents are available, the model results are tested by calculating the magnitude of the longshore current as a combination of theoretical approaches and model data. To calculate the magnitude of the longshore current velocity generated by wave-current interactions the approaches of Longuet-Higgins (1970) and Thornton and Guza (1986) were used (see section 2.3.3).

The output of the Wadden Sea model coupled with the wave model FVCOM-SWAVE for the significant wave height, the peak frequency, wave direction and the bottom orbital velocity is interpolated on the section in front of the barrier island Langeoog shown in figure 4.12 during the storm event in 2006 (01.11.06, 01:00:00 UTC) and is used to calculate

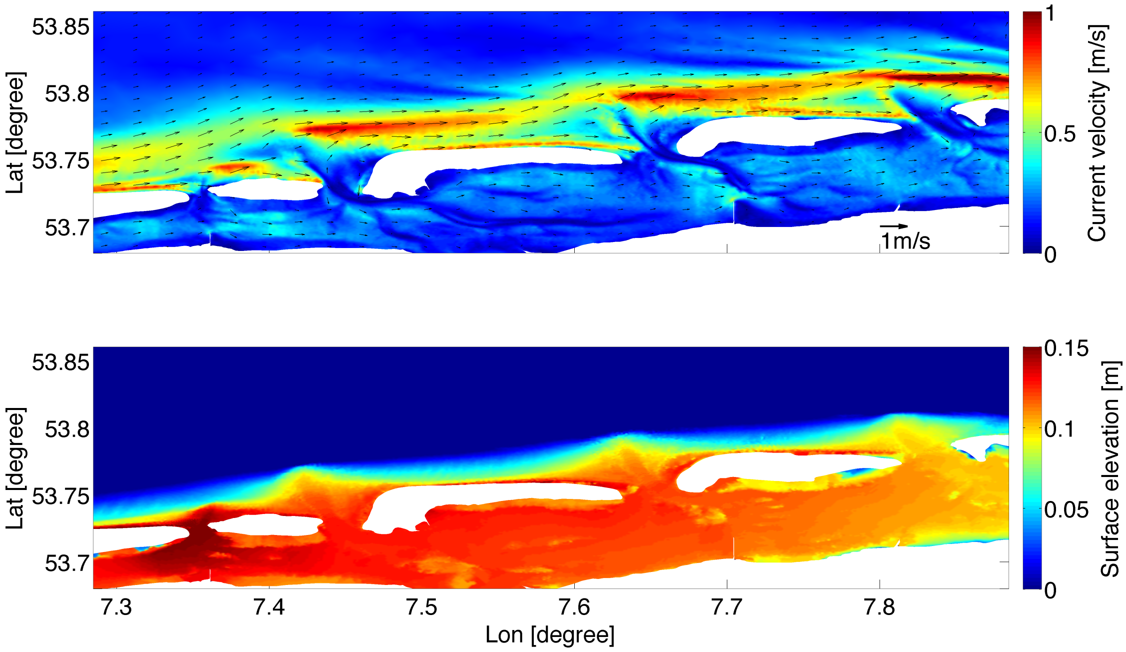

Figure 4.17: Modelled overall residual current and the difference in surface elevation due to current-wave interaction (Wadden Sea model). The top picture shows the residual currents during the time period 31.10.06/01.11.07. Again the arrows have been interpolated onto an uniform grid. The bottom picture depicts the difference in surface elevation between two model runs with and without the wave model coupled to the hydrodynamic model during the storm surge Britta.

the longshore current velocities in the shallow water area using the two formulas 2.152 and 2.161. Assuming a Rayleigh wave height distribution H_{rms} can be calculated using the significant wave height H_s and equation 2.83. The bottom friction coefficient can be calculated using equation 2.113.

For the Wadden Sea model χ was chosen to have a value of 0.067 m^2s^{-3} which is also recommended in the literature (see section 2.2.8). The longshore current velocity v_{LH} in the shallow water zone was then calculated using the depth and the wave angle at around 800 m away from the coast. The bottom friction coefficient is calculated using the bottom orbital velocity taken from the model. The value of β_b was chosen to be 0.290 to fit the velocity calculated by the model. As α_b is half the value of the wave breaking coefficient used in the model, it can be calculated as $0.5 \cdot 0.73$. The slope was calculated as the gradient between the first seven points on the section close to the coast. The resulting values for v_{LH} can be seen in table 4.2.

To calculate the velocity v_{TG} the breaking coefficient γ was chosen to be 0.73 as it was defined in the model. The breaker coefficient B was set to 1. The resulting values for v_{TG} are also listed in table 4.2.

The formula for v_{TG} is only valid for small values of v_{TG} compared to $|\vec{u}|$ that can be

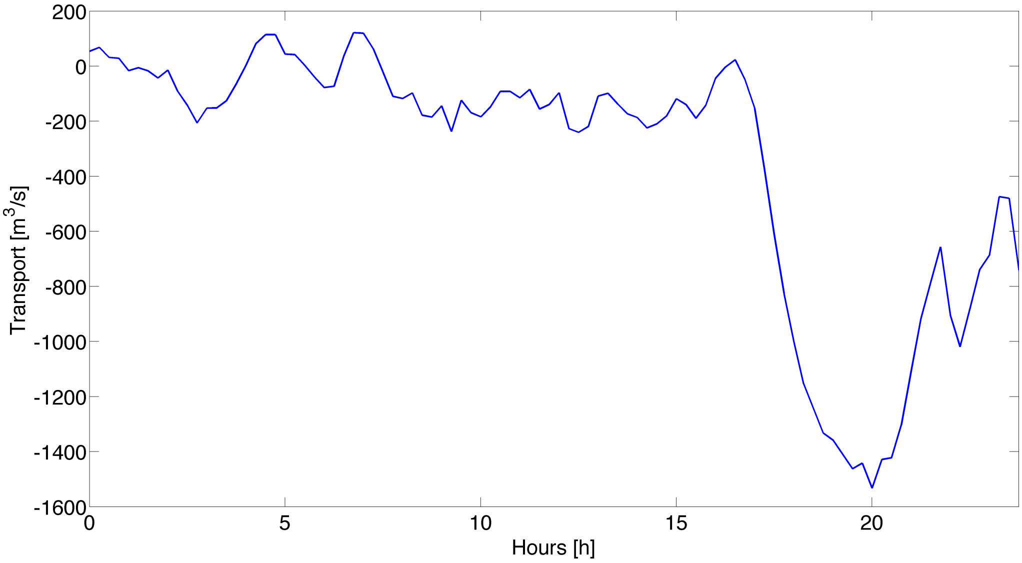

Figure 4.18: Modelled difference in volume transport due to current-wave interaction (Wadden Sea model). The plot shows the volume transport via a tidal inlet between the barrier islands Langeoog and Spiekeroog during the 31.10.06. The difference in transport is calculated from the difference of two model runs with and without the wave model coupled to the hydrodynamic model.

calculated using:

$$\overline{|\vec{u}|} = \frac{1}{2}\left(\frac{g}{h}\right)^{1/2}\left[\frac{\sqrt{\pi}}{2}H_{rms}\right]\left(\frac{2}{\pi}\right) \tag{4.1}$$

Until a distance of 268.7 m to the coast the velocities calculated with output data of the model seem to be comparable to the velocity difference of a model run with and without the wave model FVCOM-SWAVE. Since the coastline almost exactly follows a W-E-direction the u-component (eastward) of the model output was used to compare to the values presented in table 4.2.

In order to check for the unrealistic offshore-directed transport in the wave-shoaling re-

Table 4.2: Calculated values for the longshore current at different positions in front of the barrier island Langeoog

Distance from coast $[m]$	v_{FVCOM} $[m/s]$	v_{LH} $[m/s]$	v_{TG} $[m/s]$	$\overline{\|\vec{u}\|}$ $[m/s]$
0	0.28	0.22	0.06	0.72
134.3	0.41	0.28	0.16	0.59
268.7	0.33	0.34	0.24	0.64
403.0	0.28	0.36	0.29	0.67
537.3	0.25	0.37	0.36	0.68
671.7	0.21	0.38	0.46	0.69

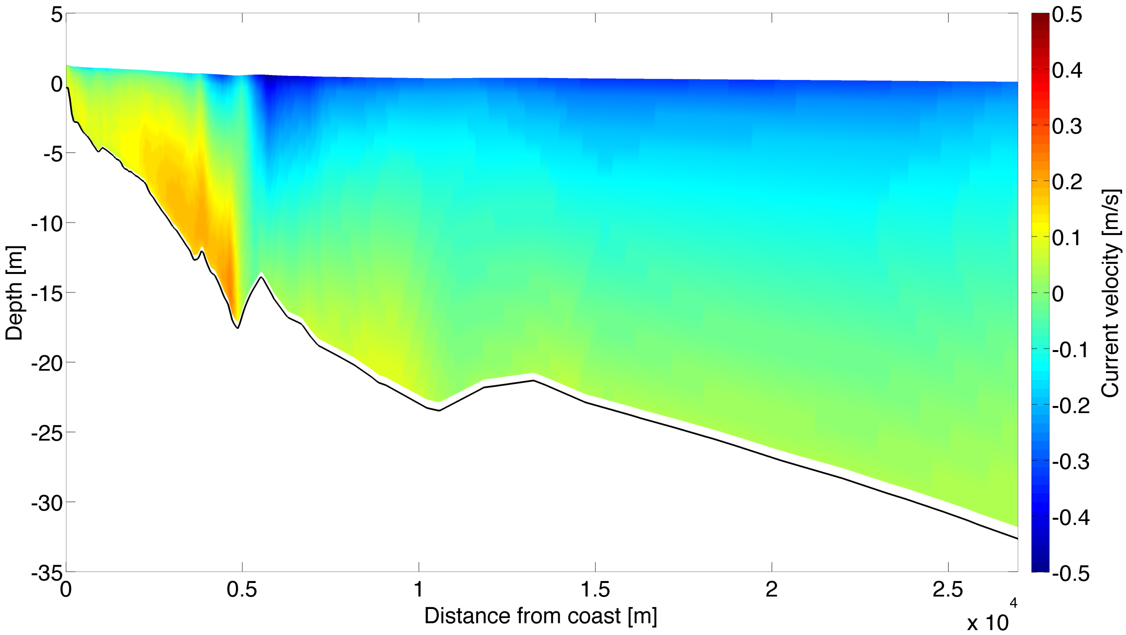

Figure 4.19: Vertical profile of the offshore directed current velocities with the wave model coupled to the hydrodynamic model (Wadden Sea model). The plot shows the v-component of the current velocity that was interpolated on the section in front of the barrier island Langeoog shown in figure 4.12 at the time point 01.11.06, 01:00:00 UTC during the storm surge Britta.

gions and close to steep bathymetry which was reported by Moghimi et al. (2012) the v-component was interpolated again on the section in front of the barrier island Langeoog shown in figure 4.12 at the time point 01.11.06, 01:00:00 UTC during the storm surge Britta. In figure 4.19 it can be seen that a offshore directed velocity is present in the shoaling zone and close to a steep slope at the bottom of the ocean. In a realistic test case that was analysed by Moghimi et al. (2012), the radiation stress formulation caused offshore transport at the surface of the water column. Here, the transport is directed to the coast at the top of the ocean and at the bottom of the water column a strong cross-shore component can be noticed. Close to the coast the cross-shore transport becomes zero at the water surface. This behavior is similar to the test case analysed by Moghimi et al. (2012). Only the transport close to the coast at the top of the ocean is not zero in their test case. So generally speaking, the transport predicted by the model seems to be realistic. But, there are differences in the structure of the topography and the wave conditions between the test case and the storm surge that has been modelled in this thesis. Additionally, there are no wave-induced mixing and wave roller effects included in the FVCOM setup. This limits the comparability of both cases. The effect of the strong cross-shore transport close to the coast is absent for a model run without the wave model coupled to the hydrodynamic model (see figure 4.20). Here, the weak

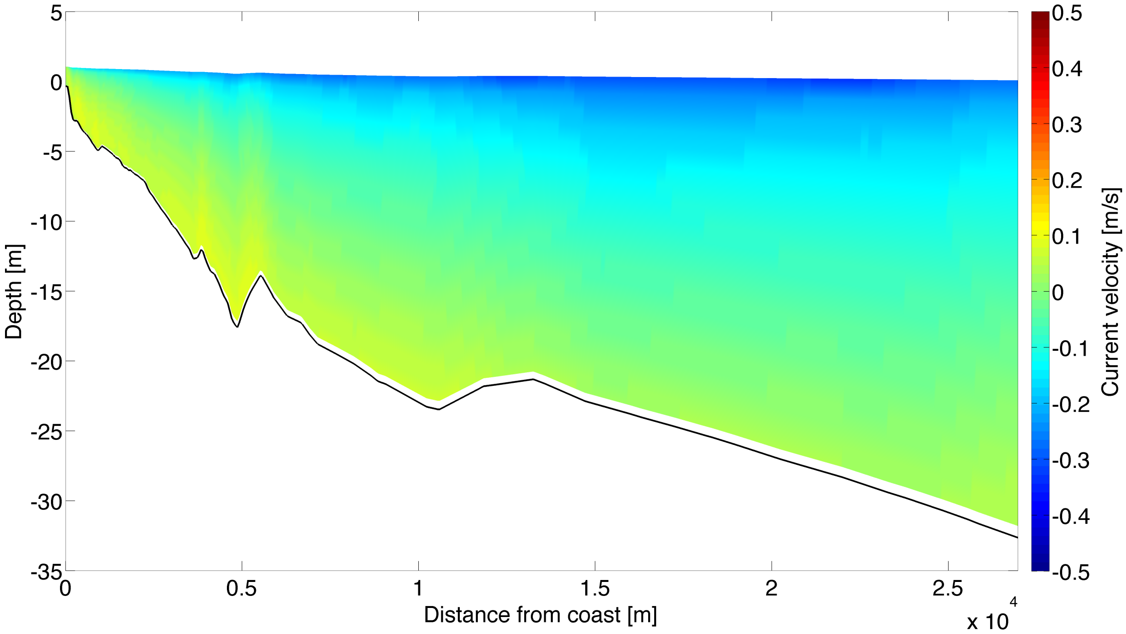

Figure 4.20: Vertical profile of the offshore directed current velocities without the wave model coupled to the hydrodynamic model (Wadden Sea model). The plot shows the v-component of the current velocity that was interpolated on the section in front of the barrier island Langeoog shown in figure 4.12 at the time point 01.11.06, 01:00:00 UTC during the storm surge Britta

transport at the bottom is homogeneously directed to the open ocean and the transport at the top of the water column is directed to the coast and is reduced to zero close to the shoreline. The figure 4.21 depicts the overall magnitude of the current velocity generated by the wave-current interactions. It can be seen that the longshore current extends to the whole water column close to the coast and will therefore strongly affect he sediment and bedload transport in this region. Without the wave-current interactions the current velocity is only strong at the surface due to wind stress. Thus, the ability of the current to transport sediment would be underestimated in this case.

4.8 Discussion

The wind and wave climate in the area of interest have been investigated and the main wind directions have been identified. Then, an unstructured-grid ocean model with a North Sea and a Wadden Sea model setup has been tested and validated for a moderate and a storm situation in 2007 and 2006, respectively. The results are reasonable and the Wadden Sea model with a high resolution shows a better performance in predicting the magnitude of the current velocities. A first estimate of the wave-induced energy flux has been calculated, showing a high energy flux under storm conditions and the ability of the

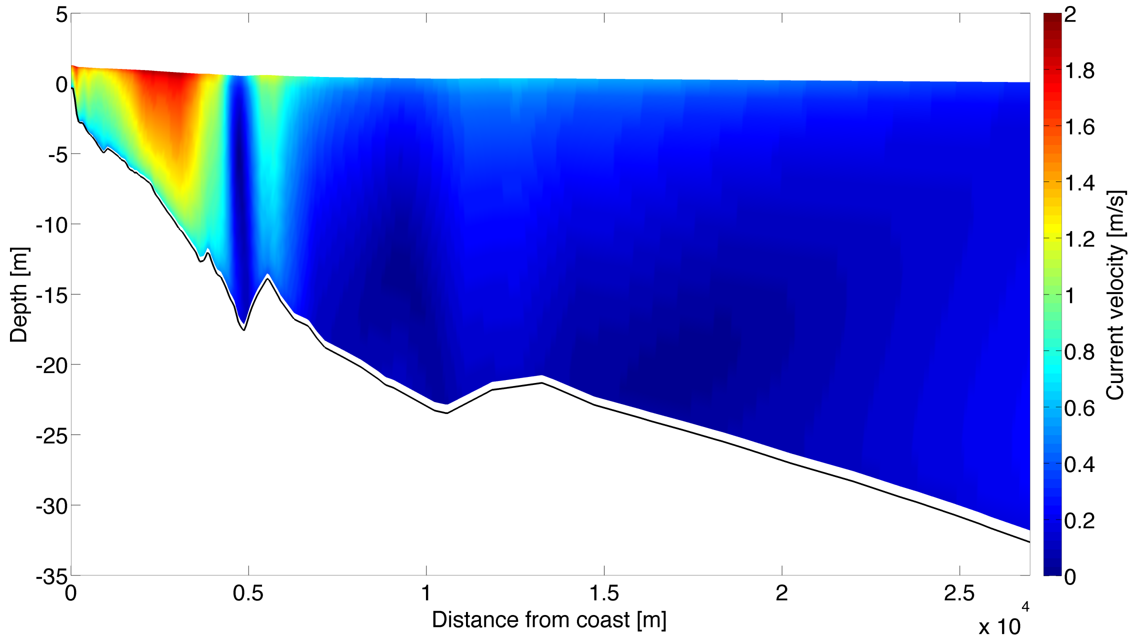

Figure 4.21: Vertical profile of the overall current velocity (Wadden Sea model). The plot shows the magnitude of the current velocity that was interpolated on the section in front of the barrier island Langeoog shown in figure 4.12 at the time point 01.11.06, 01:00:00 UTC during the storm surge Britta.

barrier island system to absorb most of the energy as it was mentioned by Krögel and Flemming (1998). Some of the energy entered the inlet and was dissipated while traveling through the channel, also providing erosion potential in this area. The sensitivity of the longshore currents to different wind directions was tested and the main contribution to the longshore current results from E-SE-directed winds (Cartesian convention) which produce a current directed to the east. Strong longshore currents that were expected to occur under storm conditions could be reproduced by the model's implemented wave-current interaction mechanisms. The calculated effects of the wave-current interactions compare well with the results found by Pleskachevsky et al. (2009) for the island of Sylt. There have not been measurements for the longshore current during storm events, so these results are a first approach to estimate the magnitude of this effect in the East Frisian barrier island system. This effect may play a major role in sediment transport. The formulas for longshore currents derived by Longuet-Higgins (1970) and Thornton and Guza (1986) were used to calculate the magnitude of these currents with model output as input values and the results are of the same magnitude as the currents predicted by the model. The surface elevation during a storm event was also influenced by the wave-current interaction. This could be explained by an enhanced volume transport trough the tidal inlets. The unrealistic offshore-directed transport in the wave-shoaling regions and close to steep bathymetry which was reported by Moghimi et al. (2012) could not be noticed in the model results. Compared to model runs without the wave model coupled to the hydrodynamic model the currents are much stronger in front of the barrier island. Therefore, a coupled modelling system could be essential to calculate e.g. the sediment or bedload transport in this area.

5 Part II: Moorea Island

In this chapter the influence of wave-current interactions in the area of the South Pacific island Moorea is investigated. In section 5.1 some reasons to motivate this investigation are presented. The dynamics of the area of interest are reported in section 5.2 and the model setup used for the investigation is explained in section 5.3. The wave-induced set-down and set-up are calculated in section 5.4 and the current pattern in this region predicted by the model is shown in section 5.5. The outcome of this chapter is discussed in section 5.6.

5.1 Motivation

The water flow on coral reef systems is of interest to a wide range of scientists including coastal engineers, marine biologists, oceanographers, coral reef ecologists or wastewater engineers (see Gourlay and Colleter 2005). Most of the coral reef systems are spatially inhomogeneous and consist of different sub-systems which have different benthos and widely varying geomorphology, including the reef itself, lagoons, outflow and inflow areas and regions of the neighboring ocean that are affected by the reefs (see Hearn 2011). These sub-systems are connected hydrodynamically by different processes. Most of the processes happening in front of the reef are controlled by its topographic complexity. Especially the process of wave breaking is influenced by the gradient of the decreasing depth towards the reef flat. Shallow reefs dissipate wave energy very efficiently and can be seen as natural breakwaters (Munk and Sargent 1954). The lagoon is fed with water from the reef and has its own circulation pattern (Hench et al. 2008). The currents inside a reef system are produced by wave driven currents, astronomical tides, wind stress and on some reefs other influences like thermohaline processes and long period ocean oscillations (von Arx 1948, Munk and Sargent 1954, Kench 1998, Monismith et al. 2006, Hearn 2011). The most important process is wave breaking and the main processes of the water flow across a reef include wave breaking on a well-defined fore-reef and flowing across the adjoining reef flat into the lagoon (Hearn 2011). This flow is very different from the flow generated by radiation stress processes in a beach zone. At the beach, the waves are influenced by shoaling and breaking and the water flow is forced into an alongshore direction (Monismith et al. 2013). The net transport normal to beaches is zero. On the

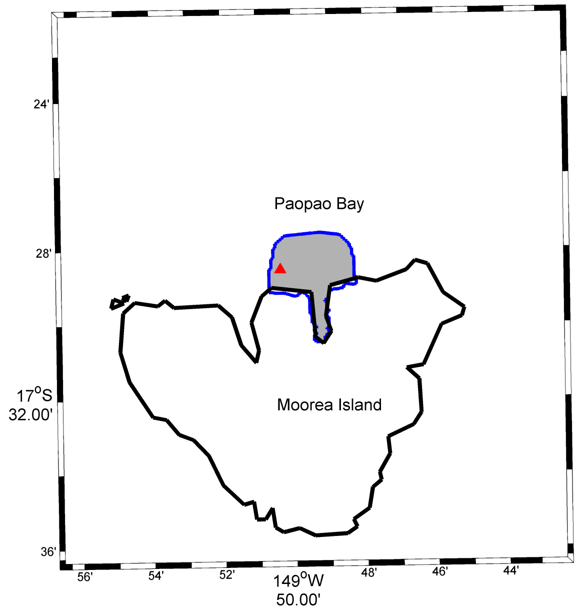

Figure 5.1: Area of interest including the Moorea island and the Paopao Bay. The blue line depicts the coverage of the model. The red triangle shows the position of the measuring spot where the data was collected that was used by Ahmerkamp (2010) to calculate quantities as e.g. the radiation stress.

contrary, shoaling normal to a reef can drive cross-shore flows and thus the net transport normal to a barrier-type reef is non-zero.

One of the first physical model approaches to study wave-generated currents across reefs was published by Gourlay (1965). Two-dimensional laboratory model experiments were performed by Gourlay (1996a). He investigated the wave set-up and wave-generated flows over a horizontal reef platform with a steep seaward face and he reported that the wave-induced flow was driven by the wave set-up created by the breaking waves on the exposed side of the reef and this set-up increased with both increasing wave height and period and decreased with increasing depth over the reef-top. A theoretical analysis for wave set-up on a reef with a steep face was given by Gourlay (1996b) which was extended by Gourlay and Colleter (2005) to include the influence of an unidirectional flow upon the magnitude of the set-up on a two-dimensional reef. A predictive type model for wave propagation and breaking over a arbitrary reef slope was presented by Massel and Gourlay (2000). Knowledge of the influence of different reef-face slopes and wave conditions on the wave-induced set-up is essential for the prediction of flooding of a low lying reef-top island. A review on the different conceptual and numerical modelling approaches for different reef systems was published by Monismith (2007).

The reef system that is investigated in this chapter is a bay on the northern shore of the Pacific island Moorea, French Polynesia (see Ahmerkamp 2010). This study site has some typical features that can be utilised to investigate the current system generated

Figure 5.2: Photo of the Paopao Bay, Moorea (Source: Hench et al. (2008)). The photo was taken by Jacques Beauregard.

by a wave-driven flow which was first done by Hench et al. (2008). They reported that this reef system is characterised by a very steep face and compared observed data to the theoretical approaches given by Hearn (1999) and Gourlay and Colleter (2005) and found significant deviations. Observations allowing to estimate the magnitude of the radiation stress have been analysed by Ahmerkamp (2010) and are used to evaluate the modelling results given in this chapter.
The modelling system FVCOM has been utilised to investigate the wave-current-related processes in the Paopao Bay on the Moorea island. The aims of this part of the thesis are (i) to estimate the wave-related quantities on a cross-section over the reef crest and the lagoon towards the shore and (ii) to reproduce the pattern of the current circulation; (iii) discuss the results of the modelling approach and the capabilities of the application of FVCOM in this area.

5.2 Study site

The study site is located at the Paopao Bay (see figure 5.1) on the northern shore of the South Pacific island Moorea, French Polynesia (see Hench et al. 2008, Ahmerkamp 2010). The island Moorea is a volcanic island in a medium development status and barrier reefs can be found around this island. These reefs typically consist of a steep fore reef, a reef crest or flat, a lagoon and the shore. The Paopao Bay is about 4 km long and 1 km wide

surrounded by land on three sides. It is connected to the open ocean via a narrow deep passage which divides the reef flat into two parts (see figure 5.2) and runs approximately north-south. The whole bay and the lagoon have a mean depth of 25-30 m and 10-20 m, respectively. The depth of the reef crest can be less than 10 m. The fore-reef has an average slope of 1 : 8 and decreases to -500 m into the direction of the open ocean. Coral colonies cover the shallow part of the fore-reef, the back reef and the shallower edges of the lagoon.
The tidal amplitudes are small (around 15 cm) so Hench et al. (2008) hypotise that the circulation through the reef flat-lagoon-reef passage system is driven primarily by surface gravity wave forcing, which can be modified by wind stress and buoyancy effects. They distinguish between three components of the flow process: (1) the wave-driven flow over the reef and through the shallow lagoon; (2) the return flow through the passage and (3) the momentum jet that exits the passage into the prevailing alongshore flow and is at least partially reentrained into the reef-lagoon system by wave-driven flow. This circulation pattern and the resulting exchange of water between the open ocean and the lagoon have a significant importance for the local ecosystem (see Ahmerkamp 2010).
During the measurements of Hench et al. (2008) the wind speed was typically small (<5 m/s) and coming generally from a NE-direction. The significant wave heights were between 0.85 m to 2.60 m and the significant wave periods ranged from 8 s to 22 s. On average, the waves were mainly coming from a NNW-direction (around 345°). The current velocities in the passage and over the reef crest are strongly coupled to the offshore wave forcing with little connection to the winds and can reach up to 0.4 m/s. The wave-induced set-up can increase the water level at the reef crest to a maximum value of around 0.2 m. Ahmerkamp (2010) calculated values of the radiation stress mostly between 0 and 12 m^3s^2. He found that for small values of the radiation stress the results compared well with values calculated from linear theory. The values for the radiation stress were divided by the density of seawater, so the unit is m^3s^2 and not N/m. This procedure is done for all values of the radiation stress presented in this chapter.

5.3 Model setup

The digital coastline and bathymetry data was provided by Soeren Ahmerkamp and taken from Hench et al. (2008).
The wind and pressure data were taken from the NCEP Reanalysis on a T62 Gaussian grid with a resolution of 192×94 grid points in space and a temporal resolution of 6 hours and a global grid with a resolution of 144×73 grid points and the same temporal resolution, respectively. The NCEP Reanalysis data was provided by the NOAA/OAR/ESRL PSD, Boulder, Colorado, USA, from their Web site at http://www.esrl.noaa.gov/psd/

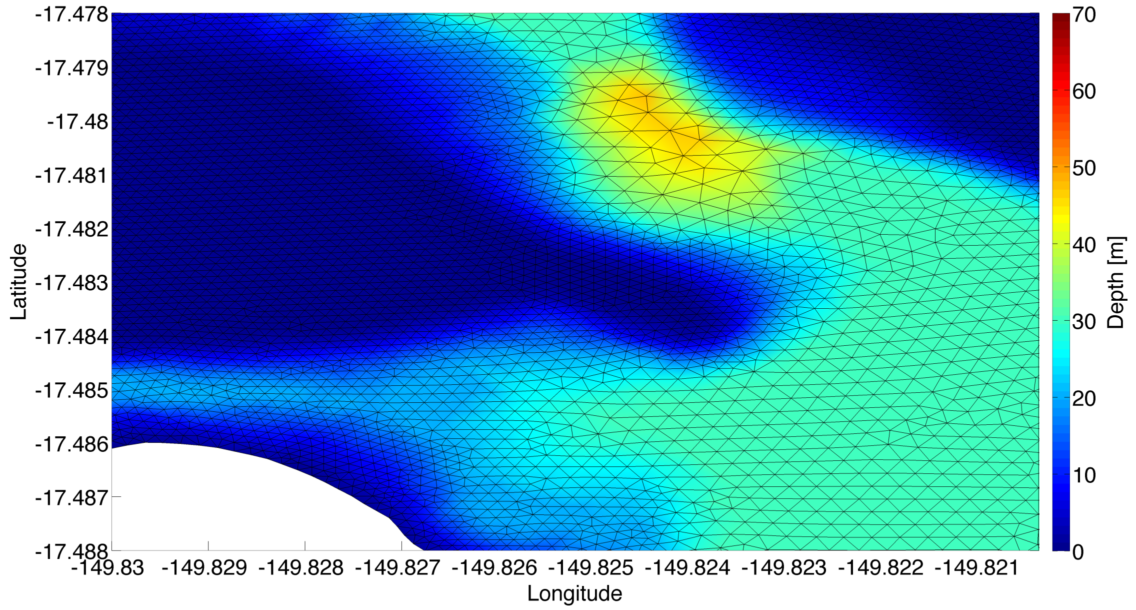

Figure 5.3: Model grid at the location of the passage between the two reef flats. The resolution of the grid is high on the reefs and coarse in the area of the deep passage.

(see Kalnay et al. 1996).
The wave conditions at the open boundary (see figure 5.1) were taken from the NOAA WAVEWATCH III CFSR Reanalysis Hindcast dataset from the Web site at http://polar.ncep.noaa.gov/waves/CFSR_hindcast.shtml (see Chawla et al. 2012). The output of the global model has a resolution of $1/2°\times1/2°$ in space and 3 hours in time. The spectral domain of the global model has been divided into 50 frequency and 36 directional bins. The directional range is a full circle 360° and the frequency range is 0.0035-0.963 Hz. The wave direction of the waves at the open boundary of the local model was fixed to 355° because the wave direction from the global model was directed out of the model area during the investigated time period (08.02.09-10.02.09). The value of the wave direction was chosen from the measurements of Hench et al. (2008) and to generate a wave direction almost normal to the wave crest.
For the surface elevation at the open boundary the output of the Global Tide model FES2004 (Finite Element Solution 2004) was used.
The resolutions of the global grids are very coarse, so the model results will not mirror reality, but the typical physical processes should be visible.
A section of the grid can be seen in figure 5.3. The grid has a fine resolution on the reef tops and close to the boundary of up to 8.4 m and a coarser resolution in deeper areas of the model with a maximum value of 58 m. A vertical resolution of 20 σ-layers was chosen. The grid was generated by Soeren Ahmerkamp during a student project in the work group "Physical Oceanography (Theory)" at the University of Oldenburg. It consists of 70324

elements and 35545 nodes.
The surface wave model FVCOM-SWAVE was utilised in a non-stationary mode with a time step of 4 s. The default conditions for wave energy input and dissipation and for wave propagation were applied. In detail, the processes of wave growth, quadruplet wave interactions, white capping, wave breaking, bottom friction and triad wave interactions have been activated. The resolution of the frequency and the directional domain are 30 and 24 bins, respectively. The directional range is a full circle 360° and the frequency range is 0.04-0.4 Hz. The peak period had to be smoothed for the hotstart procedure at the open boundary.
For the hydrodynamic part of FVCOM a time step of 0.5 s was used. The salinity and temperature were set to a constant value of 35 PSU and 20 °C, respectively.
The first six hours of the model run were used as the spin-up period. The analysed time period was 08.02.09, 06:00:00 - 11.02.09, 00:00:00 UTC.
The computations were performed on the cluster of the North-German Supercomputing Alliance (Norddeutscher Verbund zur Förderung des Hoch- und Höchstleistungsrechnens - HLRN) and the cluster HERO (High-End Computing Resource Oldenburg), funded by the Deutsche Forschungsgemeinschaft (DFG) and the Ministry of Science and Culture (MWK) of the State of Lower Saxony, Germany. The number of the processors used for the computations was 32 and the integration time for one time step was around 2.4 s.

5.4 Wave-induced set-down and set-up

As it has been mentioned in section 5.2 the investigated area includes a reef with a very steep slope. Most of the time waves are coming from a northern direction, so they will hit the reef with a wave crest almost parallel to the reef crest. This makes this area appropriate for the investigation of wave-induced effect as e.g. the wave set-up and set-down.
In figure 5.4 the time-averaged significant wave height can be seen. The breaking process at the reef crest can be clearly identified. Before the process of breaking the wave height increases to a value of around 2.2 m due to the shoaling process. Some waves enter the lagoon through the outflow area between the crests. The process of wave propagation inside the lagoon is missing the effects of diffraction because this process is not included in the FVCOM model yet.
In figure 5.5 the depth, the modelled surface elevation, the modelled significant wave height and the radiation stress that were interpolated onto the section indicated in figure 5.4, are shown. The radiation stress is calculated using linear theory and thus depends directly on the significant wave height (see equation 2.138) and starts to increase during the process of the wave shoaling. The maximum value of the radiation stress is still of the

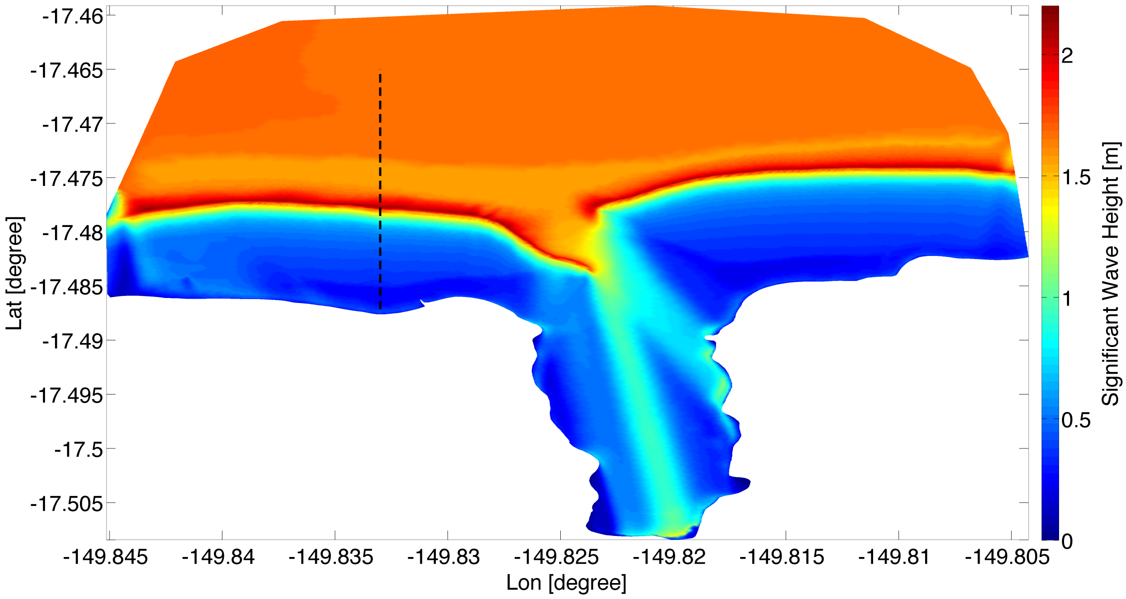

Figure 5.4: Time-averaged modelled significant wave height in the Paopao Bay, Moorea. The cross-section is used to investigate different wave-related quantities.

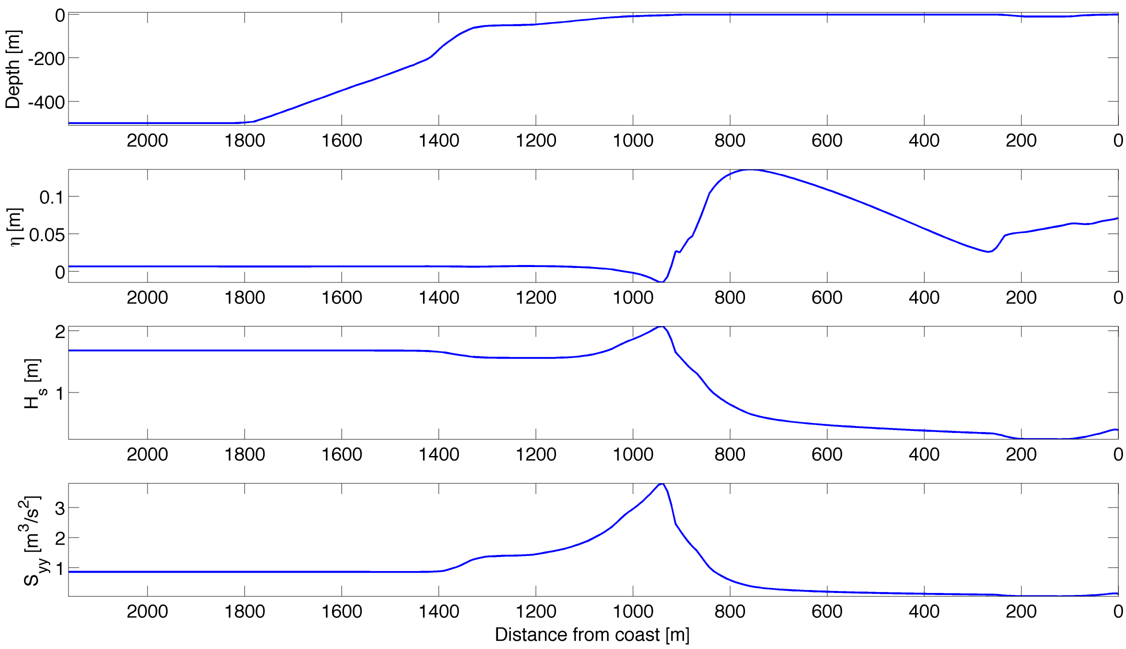

Figure 5.5: The depth, the modelled surface elevation, the modelled significant wave height and the radiation stress are shown (top to bottom) and were interpolated on the section seen in figure 5.4. The radiation stress was calculated using linear theory.

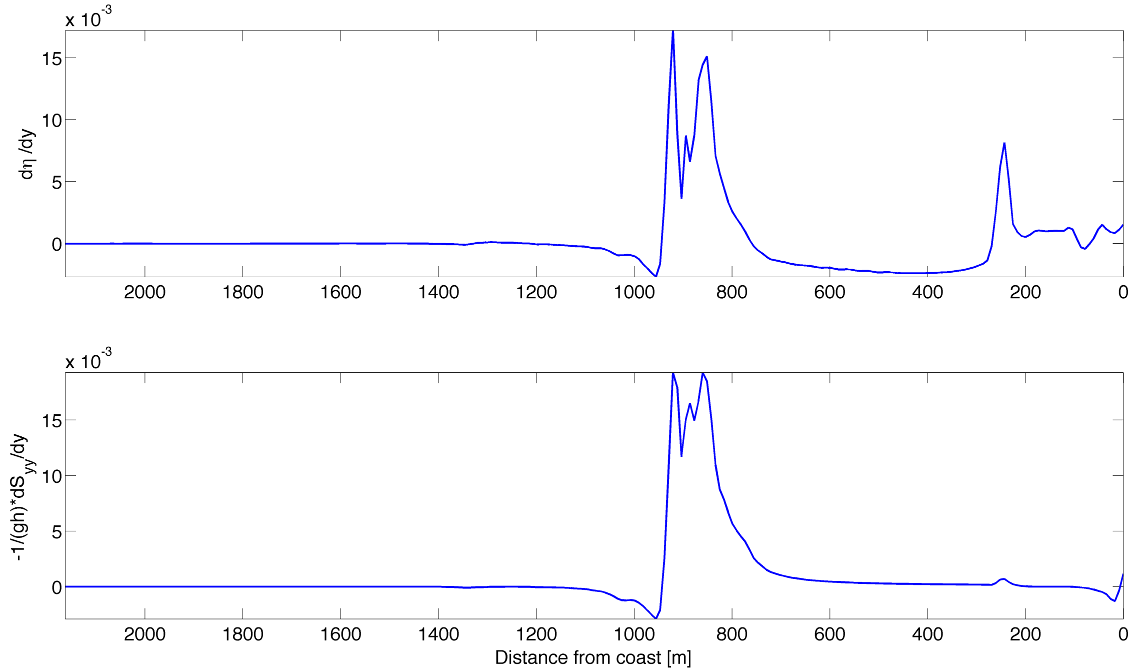

Figure 5.6: The modelled gradient of the surface elevation and the radiation stress are shown (top to bottom) and were interpolated on the section seen in figure 5.4. The radiation stress was multiplied by -1 and divided by the depth and the gravitational acceleration and is non-dimensional.

same magnitude of the values estimated by Ahmerkamp (2010) using linear theory that compared well to observational data. When the waves start to break at the crest of the reef, the radiation stress decreases along the reef flat. The surface elevation is inversely proportional to the radiation stress. As the radiation stress increases at the fore-reef, the surface elevation reaches a minimum (wave-induced set-down). Behind the breaker line the surface elevation reaches a maximum at the beginning of the reef flat (wave-induced set-up). After that, the elevation decreases again due to a pressure gradient along the reef flat that causes a water flow into the lagoon and is balanced by the bottom friction (see Hearn 2011).

The relation between the gradient of the surface elevation and the gradient of the radiation stress can be seen in figure 5.6. The plots are very similar. The deviations in the area of the reef crest can be explained by the fact that the wave crests are not normal to the reef crest, there is also a y-component of the radiation stress and a current present, so there is no stationarity in the y-direction as it is assumed in idealised theoretical approaches.

The theoretical value of the wave-induced set-down can be calculated using equation 2.146. The theoretical value is -0.0313 m and the modelled value is -0.0147 m. A value for the wave-induced set-up at the reef flat can be calculated using the equation proposed by Tait

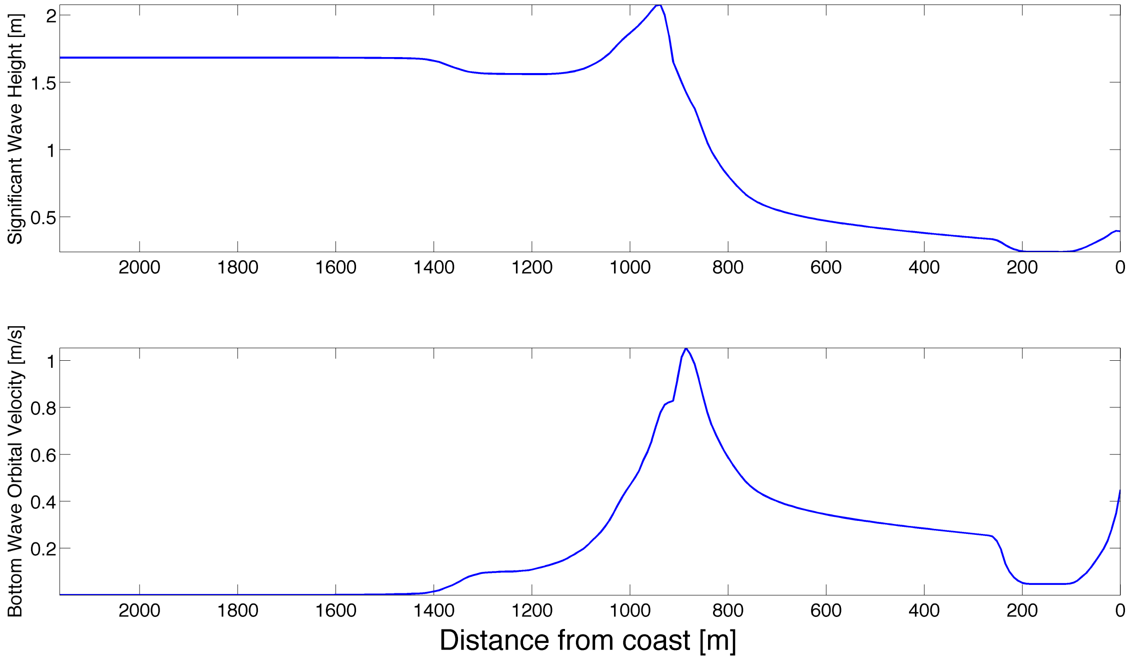

Figure 5.7: The modelled significant wave height and the modelled bottom wave orbital velocity are shown (top to bottom) and were interpolated on the section seen in figure 5.4.

(1972):

$$\overline{\eta}_{set-up} = -\frac{1}{16}\gamma^2 h_b + \left[\frac{1}{1+\frac{8}{3\gamma^2}}\right](h_b - h_{max}) \tag{5.1}$$

Here, γ, h_b and h_{max} are the wave breaking coefficient, the depth at the breaker line and the depth at the location of the maximum wave-induced set-up, respectively.
The theoretical value of the wave-induced set-up is 0.4806 m and the modelled value is 0.1358 m and is closer to the observational values from Hench et al. (2008).
In figure 5.7 the significant wave height compared to the bottom wave orbital velocity can be seen. The dissipation of wave energy due to the bottom friction is directly related to the orbital velocity. This is the dominant influence on the significant wave height before the shoaling and breaking process starts.

5.5 Current pattern in the Paopao Bay

The time-averaged current pattern in the Paopao Bay can be seen in figure 5.8 and its structure compares well to the pattern estimated by Hench et al. (2008). The current was averaged over one tidal cycle and then the difference between two model runs with and without the wave model coupled to the hydrodynamic model was calculated. The main flow directions are highlighted with black arrows. The waves induce a flow over the reef flats. At the shoreline this flow is directed to the middle part of the lagoon and then the

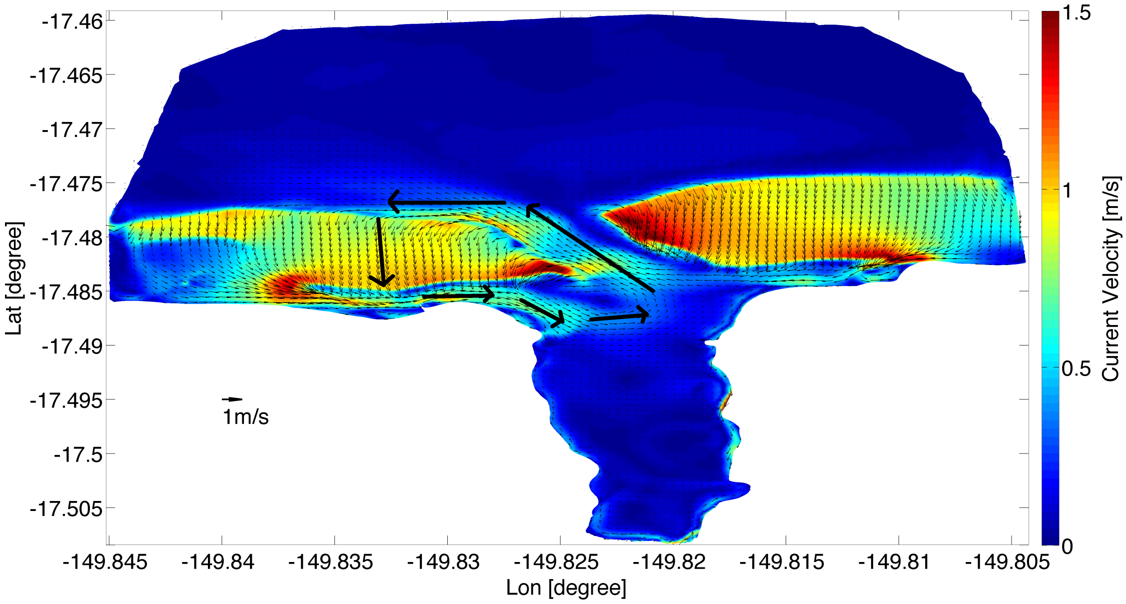

Figure 5.8: The time-averaged current pattern in the Paopao Bay. The current was averaged over one tidal cycle and then the difference between two model runs with and without the wave model coupled to the hydrodynamic model was calculated. The black arrows highlight the main flow directions.

flow leaves the lagoon via the passage between the reefs. The flow follows the reef crest and is directed again onto the reef.

Unfortunately the current velocities predicted by the model are up to four times too high. In figure 5.9 two locations are shown where extremely high velocities occur. The depth is very shallow here, so the high velocities could be caused by a Bernoulli effect and a pressure gradient. The drag coefficient for the bottom roughness may also be too small. There are coral colonies located on the reef which will increase the bottom roughness, but it is not easy to specify the drag coefficient a priori (see Monismith et al. 2013).

5.6 Discussion

The application of FVCOM to model wave-induced processes in the area of a reef region produced reasonable results at the position of the reef crest. The wave-induced set-down and set-up were too small compared to the theoretical values under idealised assumptions, but the wave-induced set-up compared well to the measured values by Hench et al. (2008). The deviations from the theoretical values may be caused by the theoretical assumption that the waves and all resulting processes are directed normal to the reef crest. The relationship between the gradient of the surface elevation and the radiation stress could be observed, too.

The structure of the current pattern of the Paopao Bay was reproduced by the model,

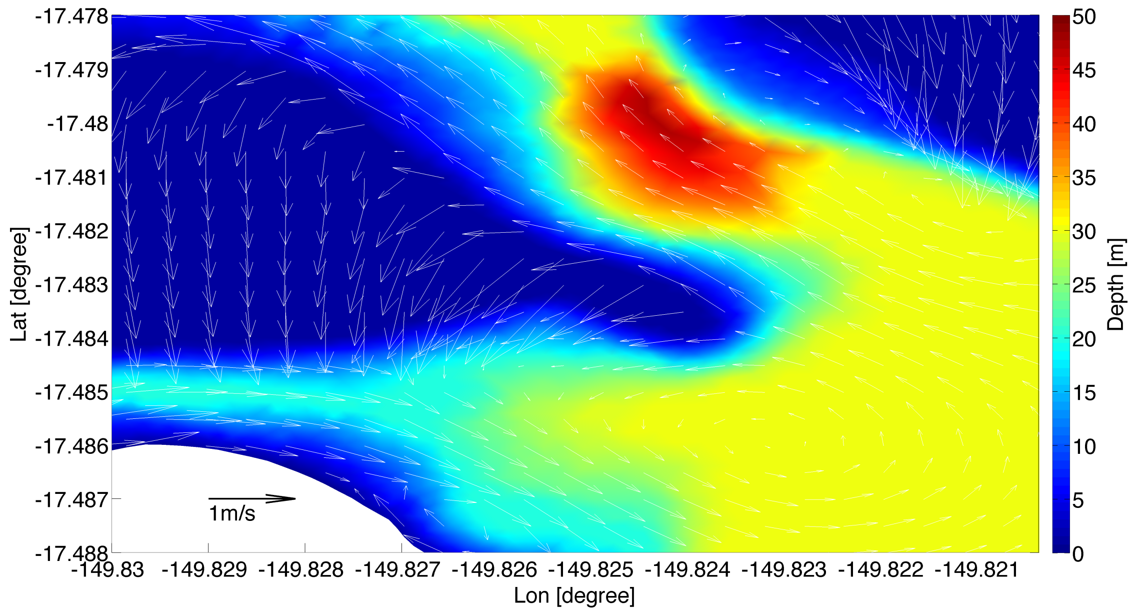

Figure 5.9: The time-averaged current pattern inside the lagoon of the Paopao Bay. Here, two locations with extremely high current velocities can be seen.

but the current velocities are too high. An increased drag coefficient could improve the model performance.

6 Conclusion

During the preparation of this thesis several FVCOM model setups have been created to investigate wave-current interactions in coastal areas. The model set-ups for the North Sea and East-Frisian Wadden Sea have been validated using observational data. The results show reasonable results, but the Wadden Sea model with a high resolution shows a better performance in predicting the magnitude of the current velocities. The wave energy flux was calculated for the area of the East-Frisian Wadden Sea and the results show that the barrier island system absorbs most of the energy. A small amount of the energy enters the inlet between two barrier islands and provides erosion potential in this area. The wave-current interactions in this area produce longshore-currents. The main contribution to the longshore current results from E-SE-directed winds and the current velocity can reach 1 m/s under storm conditions. The transport though the inlets and thus the surface elevation is also increased by the interactions. Compared to model runs without a wave model coupled to the hydrodynamic model the currents are stronger in front of the barrier islands. Therefore, a coupled modelling system could be essential to calculate e.g. the sediment or bedload transport in the area of the East-Frisian Wadden Sea.

The FVCOM modelling system was also applied to a reef region on the South Pacific island Moorea. The model produced reasonable results for the wave-induced set-up in front of the reef. The set-down was too small compared to theoretical values. The current pattern of this region could be identified in the model output, but the current velocities were overestimated. In future approaches the drag coefficient should be increased to improve the model performance.

The overall performance of the FVCOM modelling system was satisfying. Some aspects of the wave-current interactions in these specific areas could be investigated and interesting consequences of these interactions could be observed in the model output. The model benefits from the unstructured-grid approach especially in coastal areas. The governing equations of the model are based on the radiation stress theory. It will be interesting to see if this approach or the vortex force theory will deliver better results in future modelling approaches.

7 Appendix

7.1 Appendix 1: Example of an input-file for the hydrodynamic part of FVCOM

```
!================================================================!
  FVCOM 3.0
-- Beta Release
 !================================================================!
 !                                        !
 !========DOMAIN DECOMPOSITION USING: METIS 4.0.1 ================!
 !======Copyright 1998, Regents of University of Minnesota========!
 !                                        !
 &NML_CASE
 CASE_TITLE     = 'wattenmeer'
 TIMEZONE       = 'UTC',
 DATE_FORMAT    = 'YMD'
 START_DATE     = '2006-10-29 00:00:00'
 END_DATE       = '2006-11-2 00:00:00'
 /
 &NML_STARTUP
 STARTUP_TYPE      = 'coldstart'                ,
 STARTUP_FILE      = 'wattenmeer_restart_0001_1_11_12uhr.nc'                  ,
 STARTUP_UV_TYPE   = 'default'                              ,
 STARTUP_TURB_TYPE = 'default'                              ,
 STARTUP_TS_TYPE   = 'constant'                  ,
 STARTUP_T_VALS    = 10.0     ,
 STARTUP_S_VALS    = 35.0  ,
 STARTUP_DMAX      = -10.00000
 /
 &NML_IO
 INPUT_DIR      = './'        ,
 OUTPUT_DIR     = './wattenmeer_test'                 ,
 IREPORT =         10,
 VISIT_ALL_VARS  = F,
 WAIT_FOR_VISIT  = F,
 USE_MPI_IO_MODE = F
 /
 &NML_INTEGRATION
 EXTSTEP_SECONDS =  0.40 ,
 ISPLIT         =  5,
 IRAMP          =  21600,
 MIN_DEPTH      =  0.05000000E+00,
 STATIC_SSH_ADJ  =  0.0000000E+00
 /
 &NML_RESTART
 RST_ON  = T,
 RST_FIRST_OUT    = '2006-11-2 00:00:00'                ,
 RST_OUT_INTERVAL = 'seconds=900.'                      ,
 RST_OUTPUT_STACK =         3
 /
 &NML_NETCDF
 NC_ON   = T,
 NC_FIRST_OUT    = '2006-10-29 00:00:00',
 NC_OUT_INTERVAL = 'seconds=900.'                 ,
```

```
NC_OUTPUT_STACK =          0,
NC_GRID_METRICS = F,
NC_VELOCITY    = T,
NC_SALT_TEMP   = F,
NC_TURBULENCE  = T,
NC_AVERAGE_VEL = T,
NC_VERTICAL_VEL = F,
NC_WIND_VEL    = F,
NC_WIND_STRESS = F,
NC_EVAP_PRECIP = F,
NC_SURFACE_HEAT = F,
NC_GROUNDWATER = F
NC_WAVE_PARA   = T,
NC_WAVE_STRESS = T
/
&NML_NETCDF_AV
NCAV_ON = F,
NCAV_FIRST_OUT = 'none'   ,
NCAV_OUT_INTERVAL     = 'none'                     ,
NCAV_OUTPUT_STACK     =          0,
NCAV_SUBDOMAIN_FILES  =            ,
NCAV_GRID_METRICS     = F,
NCAV_FILE_DATE = F,
NCAV_VELOCITY  = F,
NCAV_SALT_TEMP = F,
NCAV_TURBULENCE = F,
NCAV_AVERAGE_VEL      = F,
NCAV_VERTICAL_VEL     = F,
NCAV_WIND_VEL  = F,
NCAV_WIND_STRESS      = F,
NCAV_EVAP_PRECIP      = F,
NCAV_SURFACE_HEAT     = F,
NCAV_GROUNDWATER      = F,
NCAV_BIO       = F,
NCAV_WQM       = F,
NCAV_VORTICITY = F
/
&NML_SURFACE_FORCING
WIND_ON = T,
WIND_TYPE      = 'speed'                                ,
WIND_FILE      = 'winde_DWD_storm_Britta_2006_watt.nc'
,
WIND_KIND      = 'variable'                  ,
WIND_X =  0.0000000E+00,
WIND_Y =  0.0000000E+00,
HEATING_ON     = F,
HEATING_TYPE   = 'flux'                                 ,
HEATING_KIND   = 'variable'                  ,
HEATING_FILE   = 'wrf_for.nc'                                  ,
HEATING_LONGWAVE_LENGTHSCALE   =  6.3   ,
```

```
HEATING_LONGWAVE_PERCTAGE      =  0.78000000    ,
HEATING_SHORTWAVE_LENGTHSCALE  =  1.4000000    ,
HEATING_RADIATION      =  0.0000000E+00,
HEATING_NETFLUX =  0.0000000E+00,
PRECIPITATION_ON       = F,
PRECIPITATION_KIND     = 'variable'                    ,
PRECIPITATION_FILE     = 'wrf_for.nc'                  ,
PRECIPITATION_PRC      =  0.0000000E+00,
PRECIPITATION_EVP      =  0.0000000E+00,

AIRPRESSURE_ON  = T,
AIRPRESSURE_KIND       = 'variable'                    ,
AIRPRESSURE_FILE       = 'SLP_DWD_storm_Britta_2006_watt.nc'                    ,
AIRPRESSURE_VALUE      =  0.0000000E+00
/

&NML_PHYSICS
HORIZONTAL_MIXING_TYPE  = 'closure'              ,
HORIZONTAL_MIXING_FILE  = 'none'                          ,
HORIZONTAL_MIXING_KIND  = 'constant'                                            ,
HORIZONTAL_MIXING_COEFFICIENT   =  0.2000000    ,
HORIZONTAL_PRANDTL_NUMBER      =  1.00000000    ,
VERTICAL_MIXING_TYPE   = 'closure'                                           ,
VERTICAL_MIXING_COEFFICIENT    =  1.0000E-04    ,
VERTICAL_PRANDTL_NUMBER =  1.000000    ,
BOTTOM_ROUGHNESS_TYPE   = 'orig'           ,
BOTTOM_ROUGHNESS_KIND   = 'constant'                                             ,
BOTTOM_ROUGHNESS_FILE   = 'none'                                                  ,
BOTTOM_ROUGHNESS_LENGTHSCALE    =  0.001    ,
BOTTOM_ROUGHNESS_MINIMUM       =  0.0025    ,
CONVECTIVE_OVERTURNING  = F,
SCALAR_POSITIVITY_CONTROL      = T,
BAROTROPIC      = T,
BAROCLINIC_PRESSURE_GRADIENT    = 'sigma levels'           ,
SEA_WATER_DENSITY_FUNCTION     = 'dens2'     ,
RECALCULATE_RHO_MEAN    = F,
INTERVAL_RHO_MEAN      = 'seconds= 1800.0'                    ,
TEMPERATURE_ACTIVE     = F,
SALINITY_ACTIVE = F,
SURFACE_WAVE_MIXING    = F,
WETTING_DRYING_ON      = T,
ADCOR_ON       = F
/
&NML_RIVER_TYPE
RIVER_NUMBER    =          0,
RIVER_TS_SETTING       = 'specified'
RIVER_INFLOW_LOCATION   = 'edge'
RIVER_INFO_FILE   = 'RIVERS_NAMELIST.nml'
RIVER_KIND       = 'variable',
/
```

```
&NML_OPEN_BOUNDARY_CONTROL
OBC_ON                  = T,
OBC_NODE_LIST_FILE      = 'wattenmeer_obc.dat'                              ,
OBC_ELEVATION_FORCING_ON   = T,
OBC_ELEVATION_FILE      = 'wattenmeer_ele_29_10_2_11_2006_neu_3d.nc'
,
OBC_TS_TYPE             = 3,
OBC_TEMP_NUDGING        = F,
OBC_TEMP_FILE           = 'none'                                ,
OBC_TEMP_NUDGING_TIMESCALE =  0.0000000E+00,
OBC_SALT_NUDGING        = F,
OBC_SALT_FILE           = 'none'                                ,
OBC_SALT_NUDGING_TIMESCALE =  0.0000000E+00,
OBC_MEANFLOW            = F,
OBC_MEANFLOW_FILE       = 'none'                                ,
OBC_LONGSHORE_FLOW_ON     = F,
OBC_LONGSHORE_FLOW_FILE    = 'none'
/
&NML_GRID_COORDINATES
GRID_FILE       = 'wattenmeer_grd.dat'                          ,
GRID_FILE_UNITS = 'degrees'                 ,
PROJECTION_REFERENCE  = 'proj=tmerc +datum=NAD83 +lon_0=-70d10 lat_0=42d50
k=.9999666666666667 x_0=900000 y_0=0'
SIGMA_LEVELS_FILE       = 'M2_sigma.dat'                        ,
DEPTH_FILE      = 'wattenmeer_dep.dat'                          ,
CORIOLIS_FILE   = 'wattenmeer_cor.dat'                          ,
SPONGE_FILE     = 'wattenmeer_spg.dat'
/
&NML_GROUNDWATER
GROUNDWATER_ON  = F,
GROUNDWATER_TEMP_ON     = F,
GROUNDWATER_SALT_ON     = F,
GROUNDWATER_KIND        = 'none'                ,
GROUNDWATER_FILE        = 'none'                                ,
GROUNDWATER_FLOW        =  0.0000000E+00,
GROUNDWATER_TEMP        =  0.0000000E+00,
GROUNDWATER_SALT        =  0.0000000E+00
/
&NML_LAG
LAG_PARTICLES_ON        = F,
LAG_START_FILE  = 'none'                                ,
LAG_OUT_FILE    = 'none'                                ,
LAG_FIRST_OUT   = 'none'                                ,
LAG_RESTART_FILE        = 'none'                                ,
LAG_OUT_INTERVAL        = 'none'                ,
LAG_SCAL_CHOICE = 'none'
/
&NML_ADDITIONAL_MODELS
DATA_ASSIMILATION       = F,
DATA_ASSIMILATION_FILE  = 'none'                                ,
```

```
 BIOLOGICAL_MODEL       = F,
 BIOLOGICAL_MODEL_FILE   = 'none'                        ,
 SEDIMENT_MODEL  = F,
 SEDIMENT_MODEL_FILE     = 'wattenmeer_sediment.inp',
 SEDIMENT_PARAMETER_TYPE     = 'constant',
 BEDFLAG_TYPE     = 'constant',
 ICING_MODEL     = F,
 ICING_FORCING_FILE      = 'wrf_for.nc'                    ,
 ICING_FORCING_KIND      = 'variable'                    ,
 ICING_AIR_TEMP  =  0.0000000E+00,
 ICING_WSPD      =  0.0000000E+00,
 ICE_MODEL      = F,
 ICE_FORCING_FILE       = 'none'                     ,
 ICE_FORCING_KIND       = 'none'                     ,
 ICE_SEA_LEVEL_PRESSURE  =  0.0000000E+00,
 ICE_AIR_TEMP    =  0.0000000E+00,
 ICE_SPEC_HUMIDITY       =  0.0000000E+00,
 ICE_SHORTWAVE   =  0.0000000E+00,
 ICE_CLOUD_COVER =  0.0000000E+00
 /

&NML_STATION_TIMESERIES
 OUT_STATION_TIMESERIES_ON       = F,
 STATION_FILE    = 'none',
 LOCATION_TYPE   = 'node',
 OUT_ELEVATION   = F,
 OUT_VELOCITY_3D = F,
 OUT_VELOCITY_2D = F,
 OUT_WIND_VELOCITY       = F,
 OUT_WIND_STRESS = F,
 OUT_SALT_TEMP   = F,
 OUT_INTERVAL    = 'days= 0.0'
 /

 &NML_PROBES
 PROBES_ON       = F,
 PROBES_NUMBER   =           0,
 PROBES_FILE     = 'none'
 /
 &NML_NCNEST
 NCNEST_ON       = F,
 NCNEST_BLOCKSIZE        =          90,
 NCNEST_NODE_FILES       = 'file_locations_for_nesting.dat'
 /

 &NML_NCNEST_WAVE
 NCNEST_ON_WAVE  = F,
 NCNEST_BLOCKSIZE_WAVE   =          90,
 NCNEST_NODE_FILES_WAVE  = 'file_locations_for_nesting.dat'
 /
```

```
&NML_NESTING
NESTING_ON     = F,
NESTING_BLOCKSIZE      =        90,
NESTING_FILE_NAME      = 'node_nest.nc'
/

&NML_BOUNDSCHK
BOUNDSCHK_ON    = F,
CHK_INTERVAL    = 0,
VELOC_MAG_MAX   =  0.0000000E+00,
ZETA_MAG_MAX    =  0.0000000E+00,
TEMP_MAX        =  0.0000000E+00,
TEMP_MIN        =  0.0000000E+00,
SALT_MAX        =  0.0000000E+00,
SALT_MIN        =  0.0000000E+00
/

&NML_SEMI
IFCETA  =  0.5500000    ,
BEDF    =   1.000000    ,
KSTAGE_UV      =          1,
KSTAGE_TE      =          1,
KSTAGE_TS      =          1,
MSTG    = slow
/

&NML_NESTING_WAVE
NESTING_ON_WAVE = T,
NESTING_BLOCKSIZE_WAVE  =        15,
NESTING_FILE_NAME_WAVE  = 'watt_2006_wellen_29_10_2_11_neu_nesting_wave.nc'
/
```

7.2 Appendix 2: Example of an input-file for the wave model FVCOM-SWAVE

```
!======== Section 1. Start-up ==========================================
!-------- PROJECT  reading of project title and description
PROJECT = defined      !defined, default
!$$if PROJECT == defined
NAME = simple
NR = nr1
!title1 =
!title2 =
!title3 =
!$$endif PROJECT

!------- SET  setting physical parameters and error counters
SET = default       !defined, default
!$$if SET == defined
LEVEL = 0.50
NOR = 90.0
DEPMIN = 0.05
MAXMES = 0
MAXERR = 3
GRAV = 9.81
RHO = 1025.00
INRHOG = 0
HSRERR = 0.1
NAUTICAL = F
PWTAIL = 3.0
FROUDMAX = 0.8
PRINTF = 4
PRTEST = 4
!$$endif SET

!------- MODE  Set STATionary, DYNamic (NONSTAtionary) or 1D SWAN model
MODE = defined      !defined, default
!$$if MODE == defined
STATIONARY = F         !Keep this F now
ONED = F              !Keep this F now
ACUPDAT = T           !Keep this T now
!$$endif MODE

!------- COORD  spherical or cartesian coordinates
COORDINATES = defined       !defined, default
!$$if COORDINATES == defined
KSPHER = 1              !KSPHER = 0    for cartesian coordinates
                   !        1    for spherical coordinates
!REARTH = 6366198.       !radius of the earth
!PROJ_METHOD = 1         !PROJ_METHOD = 0 for quasi-cartesian projection method
(spherical option)
                   !          = 1 for uniform Mercator projection (spherical option)
                   !            default for spherical coordinates
!KREPTX = 0             !The option only for academic cases
!$$endif COORDINATES
```

```
!======== Section 2. Model Description
==========================================================
ALPC = 0.0
FULCIR = T
MDC = 24 !21
!$$if FULCIR == F
DIR1 = 0.0    !30.0
DIR2 = 360.0  !210.0
!$$endif FULCIR
MSC = 30 !25
FLOW = 0.04
FHIGH = 0.4

!======== Section 3. Input
==============================================================
INP_CUR = F
!$$if INP_CUR == T
INP_CUR_STAT = F
INP_CUR_NAME =  curr.xy
!$$if INP_CUR_STAT == F
CUR_TBEGINP = 0
CUR_DELTINP = 1
CUR_TENDINP = 100
!$$endif INP_CUR_STAT
INP_CUR_SERI = F
!$$endif INP_CUR

!INP_WI = T
!$$if INP_WI == T
!INP_WI_STAT = F
!INP_WI_NAME =  wind.xy
!$$if INP_WI_STAT == F
!WI_TBEGINP = 0.0         !unit = hour
!WI_DELTINP = 1.0         !unit = hour
!WI_TENDINP = 738.0         !unit = hour
!$$endif INP_WI_STAT
INP_WI_SERI = T
!$$endif INP_WI

INP_FR = F
!$$if INP_FR == T
INP_FR_STAT = T
INP_FR_NAME =  fr.xy
!$$if INP_FR_STAT == F
FR_TBEGINP = 0
FR_DELTINP = 1
FR_TENDINP = 100
!$$endif INP_FR_STAT
INP_FR_SERI = F
```

```
!$$endif INP_FR

INP_WLEV = F
!$$if INP_WLEV == T
INP_WLEV_STAT = F
INP_WLEV_NAME = wlev.xy
!$$if INP_WLEV_STAT == F
WLEV_TBEGINP = 0
WLEV_DELTINP = 1
WLEV_TENDINP = 100
!$$endif INP_WLEV_STAT
INP_WLEV_SERI = F
!$$endif INP_WLEV

!-------- WIND  parameters uniform wind field -------------------------
!WIND = F     !T
!$$if WIND == T
!U10 =  0.0
!WDIP = 90.0
!$$endif WIND

!======== Section 4. Boundary and initial conditions
==================================
BOUNDARY = defined     !default     !defined
!$$if BOUNDARY == defined
BOUND_CHOICE = NESTING  !UNIFORM (or CONSTANT), NESTING
NESTING_FILE = ./watt_2006_wellen_29_10_2_11_neu_nesting_wave.nc
SHAPESPEC = JON       !JON, PM, GAUS, BIN
!$$if SHAPESPEC == JON
GAMMA = 3.3
!$$else if SHAPESPEC = GAUS
SIGFR = 0.01
!$$end if SHAPESPEC
CHAR_WAVE_PERIOD = PEAK      !PEAK, MEAN
DSPR = POW                  !POW, DEGREES

HSIG = 1.0
PER = 10.0
DIR = 270.0
DD = 2.0
!$$endif BOUNDARY

INITIAL = default
!INIT_COND = HOTS          !DEF, ZERO, PAR, HOTS
!HSIG = 1.0
!PER = 1.0
!DIR = 180.0
!DD = 30.0
!if INIT_COND == HOTS, use parameters below
!HOTS_FNAME = wattenmeer_restart_0001.nc
```

```
!======== Section 5. Nesting Configuration and Output
=================================
NESTING_OUT_ON = F
INP_NEST_NAME = nesting_node.dat
NEST_INT = 1



!======== Section 6. Physics
=======================================================
GEN = 3                  !the mode generation
QUAD = T                  !this option can be used to influence the computation of
                 !nonlinear quadruplet wave interations. Default: activated.
!$$if QUAD == T
IQUAD = 2
!LIMITER = 0.1
!LAMBDA  = 0.25
!CNL4    = 3.E7
!CSH1    = 5.5
!CSH2    = 0.833
!CSH3    = -1.25
!$$endif QUAD

AGROW = T                 !if True, the wave growth term of Cavaleri and Malanotte (1981)
                 !is activated.
!$$if AGROW == T
A = 0.0015
!$$endif AGROW

!$$if GEN == 1
GEN1_CF10   = 188.
GEN1_CF20   = 0.59
GEN1_CF30   = 0.12
GEN1_CF40   = 250.
GEN1_EDMLPM = 0.0036
GEN1_CDRAG  = 0.0012
GEN1_UMIN   = 1.
GEN1_CFPM   = 0.13
!$$endif GEN == 1

!$$if GEN == 2
GEN2_CF10   = 188.
GEN2_CF20   = 0.59
GEN2_CF30   = 0.12
GEN2_CF40   = 250.
GEN2_CF50   = 0.0023
GEN2_CF60   = -0.223
GEN2_EDMLPM = 0.0036
GEN2_CDRAG  = 0.0012
```

```
GEN2_UMIN   = 1.
GEN2_CFPM   = 0.13
!$$endif GEN == 2

!$$if GEN == 3
GROWTH = KOM    !JANS, KOM, WESTH
!$$if GROWTH == JANS
GEN3_JANS_CDS1 = 4.5
GEN3_JANS_DELTA = 0.5
!$$else if GROWTH == KOM
GEN3_KOM_CDS2 = 2.36E-5
GEN3_KOM_STPM = 3.02E-3
!$$else if GROWTH == WESTH
GEN_WESTH_CDS2 = 5.0E-5
GEN_WESTH_BR = 1.75e-3
GEN_WESTH_P0 = 4.
GEN_WESTH_POWST = 0.
GEN_WESTH_POWK = 0.

!-------- WCAP  parameters whitecapping ------------------------------
WCAP = KOM      !KOM, JANS, LHIG, BJ, KBJ, CSM, AB, OFF
!$$if WCAP == KOM
WCAP_KOM_CDS2 = 0.0000236
WCAP_KOM_STPM = 0.00302
WCAP_KOM_POWST = 2.
WCAP_KOM_DELTA = 0.5
WCAP_KOM_POWK = 1.0
!$$else if WCAP == JANS
WCAP_JANS_CDS1 = 4.5
WCAP_JANS_DELTA = 0.5
WCAP_JANS_PWTAIL = 5.0
!$$else if WCAP == LHIG
WCAP_LHIG_CFLHIG = 1.0
!$$else if WCAP == BJ
WCAP_BJ_BJSTP = 0.88
WCAP_BJ_BJALF = 1.0
!$$else if WCAP == KBJ
WCAP_KBJ_BJSTP = 0.88
WCAP_KBJ_BJALF = 1.0
WCAP_KBJ_KCONV = 0.75
!$$else if WCAP == CSM
WCAP_CSM_CST = 4.0
WCAP_CSM_POW = 2.0
!$$else if WCAP == AB
WCAP_AB_CDS2 = 0.00005
WCAP_AB_BR = 0.00175
WCAP_AB_P0 = 4.0
WCAP_AB_POWST = 0.0
WCAP_AB_POWK = 0.0
!$$endif WCAP
```

```
!-------- MDIA  this part is not tested -----------------------------
MDIA = F
!$$if MDIA == T
!MDIA_LAM = F
!$$if MDIA_LAM == T
MDIA_LAMBDA = -1
!$$enfif MDIA_LAM
MDIA_CNL4C = CNL4_12
!$$if MDIA_CNL4C == CNL4_12
MDIA_CNL4_1 = 0.0
MDIA_CNL4_2 = 0.0
!$$elseif MDIA_CNL4C == CNL4
MDIA_CNL4 = 0.0
!$$endif MDIA_CNL4C
!$$endif MDIA

!-------- BREAK  parameters surf breaking ---------------------------
BRE = T
!$$if BRE == T
CONSTANT = CON          !CON, VAR
!$$if CONSTANT == CON
BRE_CON_ALPHA = 1.0
BRE_CON_GAMMA = 0.73
!$$else if CONSTANT == VAR
BRE_VAR_ALPHA = 1.5
BRE_VAR_GAMMIN = 0.55
BRE_VAR_GAMMAX = 0.81
BRE_VAR_GAMNEG = 0.73
BRE_VAR_COEFF1 = 0.88
BRE_VAR_COEFF2 = 0.012
!$$endif CONSTANT
!$$endif BRE

!-------- bottom friction parameters --------------------------------
FRICTION = T
!$$if FRICTION == T
FRIC_FORM = JON     !JON, COLL, MAD
!$$if FRIC_FORM == JON
CFJON = 0.067
!$$else if FRIC_FORM == COLL
CFW = 0.0
CFC = 0.0
!$$else if FRIC_FORM == MAD
KN = 0.05
!$$endif FRIC_FORM
!$$endif FRICTION

!-------- nonlinear 3 wave interaction parameters --------------------
TRIAD = T
```

```
!$$if TRIAD == T
TRFAC = 0.05
CUTFR = 2.5
URCRIT = 0.2
URSLIM = 0.01
!$$endif TRIAD

!-------- LIM setting parameters in conjunction with action limiter --
LIM = F
!$$if LIM == T
URSELL = 0.0
QB     = 0.0
!$$endif LIM

!-------- OBSTACLE   Definition of obstacles in comp grid. -----------
OBSTACLE = F

!  SETUP     include wave-induced set-up in SWAN calculation
SETUP = F      !T
!$$if SETUP == T
SUPCOR = 0.0     !2.0
!$$endif SETUP

!-------- DIFFRac   include diffraction approximation ----------------
DIFFRAC = F

!-------- OFF      switching standard options off --------------------
OFF = F
!$$if OFF == T
OFF_REF     = YES
OFF_FSH     = YES
OFF_BRE     = YES
OFF_WCAP    = YES
OFF_QUAD    = YES
OFF_WINDG   = YES
OFF_BNDCHK  = YES
OFF_RESCALE = YES
!$$endif OFF

!======== Section 7. Command COMPUTE
=============================================
COMPUT = COMP
NS_DELTC = 10.0
TIME_UNIT = SECOND   ! DAY, HOUR, MINUTE, SECOND
SOURCE_TERM_DTMAX = 300.0
SOURCE_TERM_DTMIN = 10.0
```

Bibliography

Ahmerkamp SH (2010) On wave motions at the steep slope of a coral reef. Bachelor Thesis, University of Oldenburg

Ardhuin F, Jenkins AD, Belibassakis KA (2008a) Comments on "The Three-Dimensional Current and Surface Wave Equations". J Phys Oceanogr 38(6): 1340-1350

Ardhuin F, Rascle N, Belibassakis KA (2008b) Explicit wave-averaged primitive equations using a generalized Lagrangian mean. Ocean Model 20(1): 35-60

Barth T, Ohlberger M (2004) Finite Volume Methods: Foundations and Analysis. Encyclopedia of Computational Mechanics Volume 1, Fundamentals, John Wiley and Sons Ltd., pp. 439-473

Bartholomä, A, Kubicki A, Badewien TH, Flemming BW (2009) Suspended sediment transport in the German Wadden Sea - seasonal variations and extreme events. Ocean Dyn 59(2): 213-225

Battjes JA, Janssen JPFM (1978) Energy loss and set-up due to breaking of random waves. In: Proceedings of the 16th International Conference on Coastal Engineering (Hamburg), New York, ASCE, pp. 569-587

Battjes JA, Stive MJF (1985) Calibration and verification of a dissipation model for random breaking waves. J Geophys Res 90(C5): 9159-9167

Beach RA, Sternberg RW (1992) Suspended sediment transport in the surf zone: Response to incident wave and longshore current interaction. Mar Geol 108(3-4): 275-294

Bennis AC, Ardhuin F (2011) Comments on "The Depth-Dependent Current and Wave Interaction Equations: A Revision". J Phys Ocenogr 41(10): 2008-2012

Blumberg AF (1994) A primer for ECOM-si. Technical Report, HydroQual, Mahwah, N. J., 66 pp.

Blumberg AF, Mellor GL (1987) A Description of a Three-Dimensional Coastal Ocean Circulation Model. In: Three-Dimensional Coastal Ocean Models, Coastal Estuarine Sciences, vol. 4, edited by N. S. Heaps, AGU, Washington, D. C., pp. 1-16

Booij N, Ris RC, Holthuijsen LH (1999) A third-generation wave model for coastal regions: 1. Model description and validation. J Geophys Res 104(C4): 7649-7666

Bouws E, Komen GJ (1983) On the Balance Between Growth and Dissipation in an Extreme Depth-Limited Wind-Sea in the Southern North Sea. J Phys Oceanogr 13(9): 1653-1658

Bryan K (1969) A Numerical Method for the Study of the Circulation of the World Ocean. J Comput Phys 4(3): 347-376

Bryan K, Cox MD (1967) A numerical investigation of the oceanic general circulation. Tellus 19(1): 54-80

Burchard H (2002) Applied Turbulence Modeling in Marine Waters. Springer-Verlag, Berlin, Heidelberg, New York

Burchard H, Bolding K (2002) GETM - a general estuarine transport model. Sci Doc EUR 20253 EN, Inst. for Environ. and Sustainability, Ispra, Italy

Cavaleri L, Rizzoli PM (1981) Wind wave prediction in shallow water: Theory and applications. J Geophys Res 86(C11): 10961-10973

Chawla A, Spindler D, Tolman H (2012) 30 Year Wave Hindcasts using WAVEWATCH III with CFSR winds - Phase 1. Tech. Note 302, NOAA/NWS/NCEP/MMAB, 12 pp.

Chen C (2013) Lecture 1: FVCOM-An unstructured grid Finite-Volume Community Ocean Model. Lecture during the PASI - The science of predicting and understanding tsunamis, storm surges, and tidal phenomena on January 2-13, 2013 at Universidad Técnica Federico Santa Mara, in Valparaso, Chile, (http://www.bu.edu/pasi-tsunami/files/2013/01/Chen-Lecture-1-Introduction-FVCOM.pdf), received on the 29th of May, 2013

Chen C, Liu H, Beardsley RC (2003) An Unstructured Grid, Finite-Volume, Three-Dimensional, Primitive Equations Ocean Model: Application to Coastal Ocean and Estuaries. J Atmos Oceanic Technol 20(1): 159-186

Chen C, Beardsley RC, Cowles G (2006a) An Unstructured Grid, Finite-Volume Coastal Ocean Model, FVCOM User Manual 2nd edn. SMAST/UMASSD Tech. Rep. 060602, School for Marine Science and Technology, University of Massachusetts Dartmouth, New Bedford, MA, 315 pp.

Chen C, Beardsley RC, Cowles G (2006b) An unstructured grid, finite-volume, coastal ocean model (FVCOM) system. Special Issue entitled "Advances in Computational Oceanography", Oceanography 19(1): 78-89

Chen C, Huang H, Beardsley RC, Liu H, Xu Q, Cowles G (2007) A finite volume numerical approach for coastal ocean circulation studies: Comparisons with finite difference models. J Geophys Res 112(C03018), doi: 10.1029/2006JC003485

Coelingh JP, van Wijk AJM, Holtslag AAM (1996) Analysis of wind speed observations over the North Sea. J Wind Eng Ind Aerod 61(1): 51-69

Collins JI (1972) Prediction of shallow-water spectra. J Geophys Res 77(15): 2693-2707

Cornett A, Zhang J (2008) Nearshore Wave Energy Resources, Western Vancouver Island, B.C., Technical Report CHC-TR-51, Canadian Hydraulics Centre

Cowles GW (2008) Parallelization of the FVCOM Coastal Ocean Model. Int J High Perform Comput Appl 22(2): 177-193

Dastgheib A, Roelvink JA, Wang ZB (2008) Long-term process-based morphological modeling of the Marsdiep Tidal Basin. Mar Geol 256(1-4): 90-100

Dean RG, Dalrymple RA (1991) Water Wave Mechanics for Engineers and Scientists. Advanced Series on Ocean Engineering - Volume 2, World Scientific Publishing Co. Pte. Ltd.

Dissanayake DMPK, Roelvink JA, van der Wegen, M (2009) Modelled channel patterns in a schematized tidal inlet. Coastal Eng 56(11-12): 1069-1083

Eldeberky Y (1996) Nonlinear transformation of wave spectra in the nearshore zone. Ph.D. thesis, published as Communications on Hydraulic and Geotechnical Engineering, Delft University of Technology, Faculty of Civil Engineering, Report No. 96-4, 203 pp.

Fenton JD, McKee WD (1990) On calculating the lengths of water waves. Coastal Eng 14(6): 499-513

Flemming BW, Delafontaine MT (1994) Biodeposition in a juvenile mussel bed of the East Frisian Wadden Sea (Southern North Sea). Neth J Aquat Ecol 28(3-4): 289–297

Flemming BW, Bartholomä, A (1997) Response of the Wadden Sea to a Rising Sea Level: a Predictive Empirical Model. Dtsch Hydrogr Z 49(2-3): 343-353

Fletcher CAJ (1991) Computational Techniques for Fluid Dynamics 1. Springer Series in Computational Physics, Springer-Verlag Berlin Heidelberg

Galperin B, Kantha LH, Hassid S, Rosati A (1988) A Quasi-equilibrium Turbulent Energy Model for Geophysical Flows. J Atmos Sci 45(1): 55-62

Garrison T (2007) Oceanography: An Invitation to Marine Science. Brooks/Cole

Geuzaine C, Remacle JF (2009) Gmsh: a three-dimensional finite element mesh generator with built-in pre- and post-processing facilities. Int J Numer Meth Engng 79(11): 1309-1331

Gourlay MR (1965) Wave-generated currents: some observations made in fixed bed hydraulic models. Department of Civil Engineering, The University of Queensland, Bulletin No. 7, 21 pp.

Gourlay MR (1996) Wave set-up on coral reefs. 1. Set-up and wave-generated flow on an idealised two dimensional horizontal reef. Coast Eng 27(3-4): 161-193

Gourlay MR (1996) Wave set-up on coral reefs. 2. Set-up on reefs with various profiles. Coast Eng 28(1-4): 17-55

Gourlay MR, Colleter G (2005) Wave-generated flow on coral reefs - an analysis for two-dimensional horizontal reef-tops with steep faces. Coast Eng 52(4): 353-387

Grashorn S (2009) Manipulation von Objekten im Mikrometerbereich mittels akustischer Levitation. Diploma Thesis, University of Oldenburg (in German language)

Günther H, Hasselmann S, Janssen PAEM (1992) The WAM model cycle 4 (Revised Version). Technical Report No. 4, German Climate Centre, Hamburg

Haidvogel DB, Beckmann A (1999) Numerical Ocean Circulation Modeling. Imperial College Press, London

Hasselmann K (1974) On the spectral dissipation of ocean waves due to white capping. Boundary-Layer Meteorol 6(1-2): 107-127

Hasselmann K, Barnett TP, Bouws E, Carlson H, Cartwright DE, Enke K, Ewing JA, Gienapp H, Hasselmann DE, Krusemann P, Meerburg A, Müller P, Olbers DJ, Richter K, Sell W, Walden H (1973) Measurements of Wind-Wave Growth and Swell Decay during the Joint North Sea Wave Project (JONSWAP). Deutsch Hydrogr Z, Suppl. A8(12): 95pp.

Hasselmann S, Hasselmann K, Allender JH, Barnett TP (1985) Computations and Parameterizations of the Nonlinear Energy Transfer in a Gravity-Wave Spectrum. Part II: Parameterizations of the Nonlinear Energy Transfer for Application in Wave Models. J Phys Oceanogr 15(11): 1378-1391

Hearn CJ (1999) Wave-breaking hydrodynamics within coral reef systems and the effect of changing relative sea level. J Geophys Res 104(C12): 30007-30019

Hearn CJ (2011) Hydrodynamics of Coral Reef Systems. In: Hopley D (eds.) (2011) Encyclopedia of Modern Coral Reefs, Encyclopedia of Earth Sciences Series 2011, Springer Netherlands, pp 563-573

Heinzl R (2007) Concepts for Scientific Computing. PhD thesis, Technische Universität Wien, Fakultät für Elektrotechnik und Informationstechnik

Hench JL, Leichter, JJ, Monismith SG (2008) Episodic circulation and exchange in a wave-driven coral reef and lagoon system. Limnol Oceanogr 53(6): 2681-2694

Holthuijsen LH (2007) Waves in Oceanic and Coastal Waters. Cambridge University Press

Huang H, Chen C, Cowles GW, Winant CD, Beardsley RC, Hedstrom KS, Haidvogel DB (2008) FVCOM validation experiments: Comparisons with ROMS for three idealized barotropic test problems. J Geophys Res 113(C07042), doi:10.1029/2007JC004557

ICCP report (2007) Climate Change 2007: Synthesis Report. Contribution of Working Groups I, II and III to the Fourth Assessment Report of the Intergovernmental Panel on Climate Change [Core Writing Team, Pachauri, R.K and Reisinger, A. (eds.)]. IPCC, Geneva, Switzerland, 104 pp.

Janssen PAEM (1991) Quasi-linear Theory of Wind-Wave Generation Applied to Wave Forecasting. J Phys Oceanogr 21(11): 1631-1642

Justic D, Wang L (2009) Application of Unstructured-Grid Finite Volume Coastal Ocean Model (FVCOM) to the Gulf of Mexico Hypoxic Zone. In: OCEANS 2009, MTS/IEEE Biloxi - Marine Technology for Our Future: Global and Local Challenges

Kalnay E, Kanamitsu M, Kistler R, Collins W, Deaven D, Gandin L, Iredell M, Saha S, White G, Woollen J, Zhu Y, Leetmaa A, Reynolds R, Chelliah M, Ebisuzaki W, Higgins W, Janowiak J, Mo KC, Ropelewski C, Wang J, Jenne R, Joseph D (1996) The NCEP/NCAR 40-Year Reanalysis Project. Bull Amer Meteor Soc 77(3): 437-471

Kantha LH, Clayson CA (1994) An improved mixed layer model for geophysical applications. J Geophys Res 99(C12): 25235-25266

Kench PS (1998) Physical processes in an Indian Ocean atoll. Coral Reefs 17(2): 155-168

Kliem N, Nielsen JW, Huess V (2006) Evaluation of a shallow water unstructured mesh model for the North Sea-Baltic Sea. Ocean Model 15(1-2): 124-136

Komen GJ, Hasselmann S, Hasselmann K (1984) On the Existence of a Fully Developed Wind-Sea Spectrum. J Phys Oceanogr 14(8): 1271-1285

Komen GJ, Cavaleri L, Donelan M, Hasselmann K, Hasselmann S, Janssen PAEM (1994) Dynamics and Modelling of Ocean Waves. Cambridge University Press

Krögel F, Flemming BW (1998) Evidence for temperature-adjusted sediment contributions in the back-barrier tidal flats of the East Frisian Wadden Sea (southern North Sea). In: Alexander, CR et al. (eds.) (1998) Tidalites: processes & products. SEPM Special Publication no. 61. SEPM, Tulsa, pp. 31-41

Lane EM, Restrepo JM, McWilliams JC (2007) Wave-Current Interaction: A Comparison of Radiation-Stress and Vortex-Force Representations. J Phys Ocenogr 37(5): 1122-1141

Large WG, Pond S (1981) Open Ocean Momentum Flux Measurements in Moderate to Strong Winds. J Phys Oceanogr 11(3): 324-336

Lettmann KA, Wolff J-O, Badewien TH (2009) Modeling the impact of wind and waves on suspended particulate matter fluxes in the East Frisian Wadden Sea (southern North Sea). Ocean Dyn 59(2): 239-262

LeVeque RJ (2002) Finite-Volume Methods for Hyperbolic Problems. Cambridge Texts in Applied Mathematics, Cambridge University Press

Longuet-Higgins MS (1970) Longshore Currents Generated by Obliquely Incident Sea Waves, 1. J Geophys Res 75(33): 6778-6789

Longuet-Higgins MS, Stewart RW (1964) Radiation stresses in water waves; a physical discussion, with applications. Deep-Sea Res 11(4): 529-562

Lyard F, Lefevre F, Letellier T, Francis O (2006) Modelling the global ocean tides: modern insights from FES2004. Ocean Dyn 56(5-6): 394-415

Madsen OS, Poon YK, Graber HC (1988) Spectral Wave Attenuation by Bottom Friction: Theory. In: Proceedings of the 21st International Conference on Coastal Engineering (Malaga), New York, ASCE, pp. 492-504

Massel SR, Gourlay MR (2000) On the modelling of wave breaking and set-up on coral reefs. Coast Eng 39(1): 1-27

McGranahan G, Balk D, Anderson B (2007) The rising tide: assessing the risks of climate change and human settlements in low elevation coastal zones. Environ Urban 19(1): 17-37

McWilliams JC, Restrepo JM, Lane EM (2004) An asymptotic theory for the interaction of waves and currents in coastal waters. J Fluid Mech 511: 135-178

Mei CC (1983) The Applied Dynamics of Ocean Surface Waves. Wiley, New York

Mellor G (2003) The Three-Dimensional Current and Surface Wave Equations. J Phys Oceanogr 33(9): 1978-1989

Mellor G (2005) Some Consequences of the Three-Dimensional Current and Surface Equations. J Phys Oceanogr 35(11): 2291-2298

Mellor GL (2008) The Depth-Dependent Current and Wave Interaction Equations: A Revision. J Phys Oceanogr 38(11): 2587-2596

Mellor G (2011) Wave radiation stress. Ocean Dyn 61(5): 563-568

Mellor G, Blumberg A (2004) Wave Breaking and Ocean Surface Layer Thermal Response. J Phys Oceanogr 34(3): 693-698

Mellor GL, Yamada T (1982) Development of a Turbulence Closure Model for Geophysical Fluid Problems. Rev Geophys 20(4): 851-875

Miles JW (1957) On the generation of surface waves by shear flows. J Fluid Mech 3(02): 185-204

Moghimi S, Klingbeil K, Gräwe, Burchard H (2012) A direct comparison of a depth-dependent Radiation stress formulation and a Vortex force formulation within a three-dimensional coastal ocean model. Ocean Model: http://dx.doi.org/10.1016/j.ocemod.2012.10.002, in press

Monismith SG (2007) Hydrodynamics of Coral Reefs. Annu Rev Fluid Mech 39: 37-55

Monismith SG, Genin A, Reidenbach MA, Yahel G, Koseff JR (2006) Thermally Driven Exchanges between a Coral Reef and the Adjoining Ocean. J Phys Ocenogr 36(7): 1332-1347

Monismith SG, Herdmann LMM, Ahmerkamp S, Hench JL (2013) Wave Transformation and Wave-Driven Flow across a Steep Coral Reef. J Phys Ocenogr: doi: http://dx.doi.org/10.1175/JPO-D-12-0164.1

Munk WH, Sargent MC (1954) Adjustment of Bikini Atoll to Ocean Waves; Bikini and nearby atolls, Marshall Islands. U.S. Geological Survey Professional Paper, 260-C, 275-280.

Osuna P, Monbaliu J (2004) Wave-current interaction in the Southern North Sea. J Mar Syst 52(1-4): 65-87

Phillips OM (1957) On the generation of waves by turbulent wind. J Fluid Mech 2(05): 417-445

Phillips OM (1977) The dynamics of the upper ocean. Cambridge University Press

Pierson WJ, Moskowitz L (1964) A proposed spectral form for fully developed wind seas based on the similarity theory of S. A. Kitaigorodskii. J Geophys Res 69(24): 5181-5190

Pleskachevsky A, Eppel DP, Kapitza H (2009) Interaction of waves, currents and tides, and wave-energy impact on the beach area of Sylt Island. Ocean Dyn 59(3): 451-461

Putnam JA, Johnson JW (1949) The dissipation of wave energy by bottom friction. Trans Am Geophys Union 30(1): 67-74

Qi J, Chen C, Beardsley RC, Perry W, Cowles GW, Lai Z (2009) An unstructured-grid finite-volume surface wave model (FVCOM-SWAVE): Implementation, validations and applications. Ocean Model 28(1-3): 153-166

Reuter R, Badewien TH, Bartholomä A, Braun, A, Lübben A, Rullkötter J (2009) A hydrographic time series station in the Wadden Sea (southern North Sea). Ocean Dyn 59(2): 195-211

Santamarina Cuneo P, Flemming BW (2000) Quantifying concentration and flux of suspended particulate matter through a tidal inlet of the East Frisian Wadden Sea by acoustic Doppler current profiling. In: Flemming, BW et al. (eds.) (2000) Muddy Coast Dynamics and Resource Management. Proceedings in Marine Science vol. 2. Elsevier, Amsterdam, pp. 39-52

Simpson JH, Sharples J (2012) Introduction to the Physical and Biological Oceanography of Shelf Seas. Cambridge University Press

Smagorinsky J (1963) General Circulation experiments with the primitive equations I. The basic experiment. Mon Wea Rev 91(3): 99-164

Snelgrove PVR (1999) Getting to the Bottom of Marine Biodiversity: Sedimentary Habitats. Bioscience 49(2): 129-138

Snyder RL, Dobson FW, Elliott JA, Long RB (1981) Array Measurement of atmospheric pressure fluctuations above surface gravity waves. J Fluid Mech 102: 1-59

Stanev EV, Wolff J-O, Burchard H, Bolding K, Flöser G (2003a) On the circulation in the East Frisian Wadden Sea: numerical modeling and data analysis. Ocean Dyn 53(1): 27-51

Stanev EV, Flöser G, Wolff J-O (2003b) First- and higher-order dynamical controls on water exchanges between tidal basins and the open ocean. A case study for the East Frisian Wadden Sea. Ocean Dyn 53(3): 146-165

Stanev EV, Wolff J-O, Brink-Spalink G (2006) On the sensitivity of the sedimentary system in the East Frisian Wadden Sea to sea-level rise and wave-induced bed shear stress. Ocean Dyn 56(3-4): 266-283

Stanev EV, Flemming BW, Bartholomä, A, Staneva, JV, Wolff J-O (2007a) Vertical circulation in shallow tidal inlets and back-barrier basins. Cont Shelf Res 27(6): 798-831

Stanev EV, Brink-Spalink G, Wolff, J-O (2007b) Sediment dynamics in tidally dominated environments controlled by transport and turbulence: A case study for the East Frisian Wadden Sea. J Geophys Res 112(C4)

Stanev EV, Grayek, S, Staneva, J (2008) Temporal and spatial circulation patterns in the East Frisian Wadden Sea. Ocean Dyn 59(2): 167-181

Staneva J, Stanev EV, Wolff J-O, Badewien TH, Reuter R, Flemming B, Bartholomä A, Bolding K (2009) Hydrodynamics and sediment dynamics in the German Bight. A focus on observations and numerical modelling in the East Frisian Wadden Sea. Cont Shelf Res 29(1): 302-319

Tait RJ (1972) Wave set-up on coral reefs. J Geophys Res 77(12): 2207-2211

Terray EA, Drennan WM, Donelan MA (2000) The Vertical Structure of Shear and Dissipation in the Ocean Surface Layer. Proc. Symp. on Air-Sea Interaction, Sydney, Australia, University of New South Wales, 239-245.

Thornton EB, Guza RT (1986) Surf Zone Longshore Currents and Random Waves: Field Data and Models. J Phys Oceanogr 16(7): 1165-1178

Timmermann R, Danilov S, Schröter J, Böning C, Sidorenko D, Rollenhagen K (2009) Ocean circulation and sea ice distribution in a finite element global sea ice-ocean model. Ocean Model 27(3-4): 114-129

Tolman HL (1992) Effects of Numerics on the Physics in a Third-Generation Wind Wave Model. J Phys Oceanogr 22(10): 1095-1111

van der Wegen, M, Dastgheib, A, Roelvink, JA (2010) Morphodynamic modeling of tidal channel evolution in comparison to empirical PA relationship. Coastal Eng 57(9): 827-837

Versteeg HK, Malalasekera W (2007) An Introduction to Computational Fluid Dynamics. The Finite Volume Method. Second Edition, Pearson Education Limited

von Arx, WS (1948) The circulation systems of Bikini and Rongelap lagoons. Trans Am Geophys Union 29(6): 861-870

WAMDI group (1988) The WAM model - A Third Generation Ocean Wave Prediction Model. J Phys Oceanogr 18(12): 1775-1810

Wang ZB, Hoekstra P, Burchard H, Ridderinkhof H, De Swart HE, Stive MJF (2012) Morphodynamics of the Wadden Sea and its barrier island system. Ocean Coast Manage 68: 39-57

Warner JC, Sherwood CR, Signell RP, Harris CK, Arango HG (2008) Development of a three-dimensional, regional, coupled wave, current, and sediment-transport model. Comput Geosci 34(10): 1284-1306

Whitham GB (1974) Linear and Nonlinear Waves. Wiley, New York

Wu J (1982) Wind stress coefficients over sea surface from breeze to hurricane. J Geophys Res 87(C12): 9704-9706

Wu LY (2009) FVCOM-based Wave-Current-Sediment Model Coupling and Its Application. Doctoral Dissertation, Ocean University of China (in Chinese language)

Wu L, Chen C, Guo P, Shi M, Qi J, Ge J (2011) A FVCOM-Based Unstructured Grid Wave, Current, Sediment Transport Model, I. Model Description and Validation. J Ocean Univ China 10(1): 1-8

Xing J, Davies AM, Jones JE (2012) Influence of sea surface wind wave turbulence upon wind-induced circulation, tide-surge interaction and bed stress. Ocean Dyn 62(7): 1017-1042

Yu Q, Wang Y, Flemming B, Gao S (2012) Modelling the equilibrium hypsometry of back-barrier tidal flats in the German Wadden Sea (southern North Sea). Cont Shelf Res 49: 90-99

8 Danksagung

Mein besonderer Dank gilt meinem Betreuer Jörg-Olaf Wolff. Während meiner Zusammenarbeit mit ihm konnte ich aus seinem großen Fundus an Wissen im Bereich der Ozeanographie schöpfen und seine Ratschläge lenkten meine Arbeit immer wieder aus Sackgassen zurück auf den rechten Weg zur erfolgreichen Promotion. Durch sein Gespür für die Feinheiten im Gebiet der Ozeanwissenschaften konnte ich immer wieder Fehler in meiner Arbeit aufdecken und meine Forschungsergebnisse stetig verbessern. Außerdem ermöglichte er mir durch die Teilnahme an verschiedenen internationalen Summer Schools und Konferenzen meinen Horizont stetig zu erweitern und wichtige Kontakte über mein Forschungsgebiet hinaus zu knüpfen.

Auch möchte ich mich herzlich bei meinem zweiten Betreuer Karsten Lettmann bedanken, der mich mit viel Geduld in die Welt der Ozeanmodellierung eingeführt hat und mir bei Problemen in der täglichen Arbeit immer wieder hilfsbereit zur Seite stand. Seine Vorarbeiten und die von ihm erstellten Programmstrukturen bildeten das Grundgerüst meiner Arbeit und Forschungsergebnisse.

Mein Dank gilt auch Chai Heng Lim, dem zweiten Doktoranden unserer Arbeitsgruppe „Physikalische Ozeanographie (Theorie)“, mit dem ich über wissenschaftliche sowie private Dinge diskutieren, streiten und lachen konnte.

Thomas Badewien ist für die Bereitstellung der von mir benutzten Messdaten verantwortlich, wofür ich mich auch sehr herzlich bedanken möchte. Soeren Ahmerkamp danke ich für das Erstellen des Gitters für das Moorea-Modell und für seine Ratschläge und Tipps zu diesem Forschungsteil meiner Arbeit.

Ich danke auch allen Bachelor-, Masterstudenten, Doktoranden und Mitarbeitern am ICBM, die mich bei meiner Forschungsarbeit unterstützt haben, wobei ich Oliver Bleich und Steffen Rettig große Hilfe beim Erstellen der Küstenlinien verdanke.

Mein Dank gilt auch Dr. Reinhard Leidl und den Mitarbeitern vom HERO- und HLRN-Cluster.

Am HZG möchte ich mich sehr herzlich bei Emil V. Stanev bedanken, der mir nun die Chance gibt, mich in der Welt der Forschung und Wissenschaft abseits der Universität zu beweisen. Ihm ist es genauso wie Jörg-Olaf Wolff zu verdanken, dass meine Abschlussarbeit konkrete Formen annahm und zur Vollendung kam.

Bei den Mitgliedern der Arbeitsgruppe „Auswertung und Datenassimilation“ am HZG möchte ich mich dafür bedanken, dass ich von Ihnen so herzlich aufgenommen wurde und bereits zahlreiche Ratschläge bezüglich meiner Forschungsarbeiten erhalten habe.

Changsheng Chen und seinen Mitarbeitern danke ich für die Bereitstellung und die Updates des FVCOM Source Codes.

Meine Arbeiten wurden durch das Ministerium für Wissenschaft und Kultur des Landes Niedersachsen im Rahmen des KLIFF-Projektes und durch die von der Helmholtz-Gemeinschaft geleitete Initiative Earth Science Knowledge Platform (ESKP) finanziert, wofür ich mich auch herzlich be-

danke.
Ein sehr großer Dank geht zu guter Letzt an meine Freundin und unsere Familien, die mir immer wieder den Rücken gestärkt haben und während meiner gesamten Doktorandenzeit bedingungslos zur Seite standen. Ohne ihre Unterstützung wäre ein Entstehen dieser Arbeit nicht möglich gewesen.

Publikationsliste

Im Laufe der Doktorarbeit wurden folgende Arbeiten eingereicht oder sind in Vorbereitung, die im Zusammenhang mit der vom Doktoranden geleisteten Forschungsarbeit stehen. Teile aus der ersten Veröffentlichung dieser Aufzählung (Grashorn et al. 2013) wurden beim Erstellen der Dissertation verwendet:

1. Grashorn S, Lettmann KA, Wolff J-O, Badewien TH, Stanev EV (2013) Radiation stresses and wave energy in a numerical model of the East-Frisian Wadden Sea (southern North Sea). Ocean Dyn (submitted)
2. Lettmann KA, Rödig E, Grashorn S, Wolff J-O, Flöser G, Badewien TH (2013) Estimates of Local Residence and Flushing Times for Jade Bay, Germany. Environmental Fluid Mechanics (in prep.)
3. Schwichtenberg F, Pätsch J, Amann T, Schartau M, Thomas H, Winde V, Dellwig O, van Beusekom J, Böttcher M, Grashorn S, Salt L (2013) Impact of internal and external Alkalinity fluxes on the carbonate system in the German Bight / SE North Sea - A model study for the years 2001-2009. (in prep.)

Sebastian Grashorn
Josef-von-Scheffel-Weg 1
21502 Geesthacht
Phone (Office): +49 – (0)4152 – 87 – 1505
Email: sebastian.grashorn@uni-oldenburg.de

Curriculum Vitae

Personal data

Name:	Grashorn
First name:	Sebastian
Date of birth:	10.04.1981
Place of birth:	Bremen
Nationality:	German
Family status:	unmarried

Work Experience

since 2013-today	Scientist in the work group “Data Analysis and Data Assimilation” at the Helmholtz-Zentrum Geesthacht Field of study: Developing tools as e.g. numerical models to investigate ocean dynamics and extreme events with a focus on the German part of the southern North Sea
since 2013-today	Member of the initiative “Earth System Knowledge Platform (ESKP)” operated by the Helmholtz Association
since 2010-2012	Research Fellow in the work group “Physical Oceanography (Theory)“ at the “Institute for Chemistry and Biology of the Marine Environment (ICBM)“ at the University of Oldenburg Field of study: High resolution unstructured-grid numerical modelling of wave-current interactions in coastal areas
since 2010-today	Member of the scientific project “KLIFF - Climate impact and adaptation research in Lower Saxony”
2000-2001	Civilian Service

Education

since 2010-today	Member of the Graduate School “Science and Technology” at the University of Oldenburg
since 2010-today	PhD Student in the work group “Physical Oceanography (Theory)“ at the “Institute for Chemistry and Biology of the Marine Environment (ICBM)“ at the University of Oldenburg Field of study: High resolution unstructured-grid numerical modelling of wave-current interactions in coastal areas

Sebastian Grashorn
Josef-von-Scheffel-Weg 1
21502 Geesthacht
Phone (Office): +49 – (0)4152 – 87 – 1505
Email: sebastian.grashorn@uni-oldenburg.de

2002-2010	Study of physics at the University of Oldenburg (final degree: Dipl. Phys., very good) Title of diploma thesis: "Manipulation of objects at the microscale using acoustic levitation" (in German language)
2002	Study of social sciences at the University of Oldenburg
2001-2002	Study of physics at the University of Heidelberg
1987-2000	School education (final degree: general qualification for university entrance (Abitur: 1,9) at the Gymnasium Wildeshausen)

Conferences

- Participant of the Joint Numerical Sea Modelling Group (JONSMOD) conference 2010
- Participant of the Storm Surges Congress 2010
- Talk at the European Geosciences Union General Assembly (EGU) 2011
- Talk at the International Workshop on Multiscale (Un-)structured Mesh Numerical Modelling for coastal, shelf and global ocean dynamics (IMUM) 2011
- Poster at the YOUMARES 2011 (3rd place in poster competition)
- Talk at the Joint Numerical Sea Modelling Group (JONSMOD) conference 2012
- Session Chair at the YOUMARES 2012 (Session: Physical Oceanography – Between Measuring and Modelling)

Additional Skills / Qualifications / Training

- Various soft skill courses at the Graduate School "Science and Technology" at the University of Oldenburg (2010-today)
- Successful participation in the course **Introduction to Matlab and C** in 2006/2007
- Successful participation in the course **Programming with C/C++** in 2006
- Internship at Biolitec Inc., East Longmeadow, MA, USA in 2004 (development and production of medical laser systems and optical fibers)
- Member of the German Physical Society (DPG) and the German Society for Marine Research (DGM)
- Knowledge in Linux, Mac, Windows office and operating software
- Drivers License (German Class B)

Foreign languages

- Fluent in both spoken and written English
- Elementary French
- Elementary Latin

Selbständigkeitserklärung

Hiermit erkläre ich, dass eine Promotion zum Dr. rer. nat. angestrebt wird, dass ich die vorliegende Dissertation selbstständig verfasst und nur die angegebenen Hilfsmittel verwendet habe. Teile der Dissertation sind zur Veröffentlichung eingereicht, aber noch nicht veröffentlicht worden. Die Dissertation hat weder in Teilen noch in ihrer Gesamtheit einer anderen wissenschaftlichen Hochschule zur Begutachtung in einem Promotionsverfahren vorgelegen. Sie liegt auch zum jetzigen Zeitpunkt weder in Teilen noch in ihrer Gesamtheit einer anderen wissenschaftlichen Hochschule zur Begutachtung in einem Promotionsverfahren vor. Die Leitlinien guter wissenschaftlicher Praxis an der Carl von Ossietzky Universität Oldenburg wurden von mir befolgt. Im Zusammenhang mit dem Promotionsvorhaben sind keine kommerziellen Vermittlungs- oder Beratungsdienste (Promotionsberatung) in Anspruch genommen worden.

Geesthacht, 12.06.2013 (Sebastian Grashorn)